Spin Relaxation in Alkali Vapors

by

Stephen John Kadlecek

A dissertation submitted in partial fulfillment
of the requirements for the degree of

Doctor of Philosophy
(Physics)

at the

UNIVERSITY OF WISCONSIN – MADISON

1999

Acknowledgements

I want to thank the many people who offered guidance and support throughout my graduate studies. Much of the credit for this work is traceable to others (although I still get the blame for typos).

The original atom trainers, Dominik Hoffmann, Rob Williamson and Paul Feng, helped me learn my way around the lab. Dominik showed me the German way to clean optics and design apparatus and I hope some of it rubbed off. As a limitless font of technical knowledge, Rob was always a handy guy to have around (to this day, the phrase 'Rob would know that...' is heard in our lab quite frequently). Paul showed me a million little lab details such as how to solder and (more importantly) how to unsolder. And I will remain forever grateful for his introducing me to bibimbap.

The current (and recently graduated) atom trainers have been tremendously helpful and patient with my periodic strange questions. As the senior graduate student, Renée Nesnidal gave me countless tips in the lab. In addition, she didn't get too mad when I snuck in and 'borrowed' a waveplate or two. Ian Nelson has been a very good person to bounce ideas off of– physics related, or not. His healthy distrust of unnecessary quantum mechanics has made me think things through more clearly on several occasions. Although we have not worked together long, Bien Chann seems to have the same characteristics and I look forward to working with him and Ian in the future. I also thank David Steele and Nathan Harrison for starting the experiment that I will be working on next, and getting it going surprinsingly quickly. Finally, I appreciate Edward Vliegen's hard work on my old experiment (thereby allowing me to write my

thesis and graduate).

I owe a great deal to my advisor, Prof. Thad Walker. His excitement about experimental physics is contageous. And, unlike many advisors, he is almost always available for discussions on work in progress or crazy ideas. I also appreciate the support of Prof. Wilmer Anderson as both a teacher and a researcher.

I am grateful to Christopher Erickson and Prof. William Happer of Princeton University for many helpful discussions. Our independent verification of experimental and theoretical results has been extremely comforting to both parties. I hope that our collaboration will continue.

I wish to acknowledge continued support from my family, starting with my newly adopted and always welcoming family, Rochelle and Selig Kainer. I thank my sister Ann for providing object lessons by doing everything first, including coming to Madison for graduate school. The debt to my parents, Mary and John, is beyond repaying, except perhaps to the next generation. My success in and appreciation for physics is a direct result of their foresight and teaching. Finally, I acknowledge the love, support and editing of my wife, Eden. I thank her for sticking with me even as I moved a thousand miles away and stopped making money, and for putting up with me as I complained about graduate school. I look forward to facing whatever comes next together.

Contents

Chapter 1

Introduction and Motivaton

1.1 Overview and Motivation

This thesis describes work I have undertaken to better understand spin-relaxation processes in a polarized alkali vapor. I have studied vapors of the three heaviest naturally occurring alkali atoms, K, Rb and Cs. The choice of atom is motivated by the many applications of a spin-polarized alkali vapor (see, for example [Walker97, Happer72]), a desire to study processes that limit the lifetime of recently created alkali Bose-Einstein Condensates, and the relative ease with which alkali atoms can be handled both experimentally and theoretically.

This investigation is geared toward three specific goals. First, I wish to be able to predict relaxation rates under a wide variety of conditions. Since spin relaxation is generally undesirable, this will allow other workers to choose conditions that minimize depolarization. Toward that end, I present a large volume of new data that allows prediction under a much more complete set of circumstances than was possible before.

Second, I wish to identify the microscopic origin of relaxation processes. This allows prediction of relaxation rates under conditions that have not been reached experimentally. In addition, since the important relaxation mechanisms are collisional in origin, such an identification adds to our basic physical understanding of spin-dependent collisions. Considerable effort has been expended to this end over the last two decades (refs. [Knize89, Wagshul94, Nagengast98, Bhaskar80, Wu85] and many others) and the data I present here is consistent with much of the previous work. However, I

have shown that one relaxation mechanism, alkali-alkali relaxation, has an unexpected magnetic field dependence. This discovery requires a new theoretical interpretation of alkali-alkali relaxation, and I present here the significant steps taken toward the correct interpretation.

Third, my relaxation measurements can be used to probe the dynamics of molecular formation and dissociation in the vapor. I show how this is achieved using measurements of relaxation in alkali singlet dimers similar to the pioneering work of Bouchiat ([Bouchiat71]) on alkali-noble gas Van Der Waals molecules. In addition, I present an accurate model of relaxation in singlet dimers and show how it can be used to determine the nuclear electric quadrupole interaction strength.

1.2 Definition and Usefulness of a Polarized Vapor

To see why a polarized alkali vapor is useful and to understand the significance of polarization-destroying collisions, we must consider the atom's electronic and nuclear structure. To a very good approximation, the alkali atom can be treated theoretically as a nucleus and a single valence electron. Each principal electronic level $|nJ\rangle$ therefore has (2J+1)(2I+1) nearly degenerate sublevels that correspond to different orientations of electronic and nuclear angular momentum. Within an order of magnitude of room temperature, alkali atoms are particularly easy to handle thermodynamically because the energy of the first electronic excited state is much greater than kT. Therefore, a typical vapor cell in thermodynamic equilibrium will most likely have no electronically excited atoms at all. On the other hand, the splitting between the nearly degenerate electronic ground states is much smaller than kT, so population is divided equally among them.

We know from experience that such a low dimensional quantum system becomes interesting if we can somehow take it out of thermodynamic equilibrium. For instance, if we create a population inversion between electronic levels, a system can be made to lase. We can observe similarly interesting and useful behavior (i.e. masing, nuclear magnetic resonance) by changing the population distribution among the electronic ground states, or polarizing the atom.

An analogy with population inversion in a laser is in many ways a good one, but unlike a population inversion, polarized ground state atoms do not return to thermal

equilibrium through spontaneous emission. Therefore, return to equilibrium is entirely through collisional processes that couple to one or more of the atomic spins. Some applications of polarized atoms depend on phase coherence between atoms, which is limited by such collisional processes as well. Thus, collisional relaxation processes limit the usefulness of a polarized vapor, and this investigation is motivated by a desire to understand and minimize their detrimental effects. Note that the relaxation processes of interest here are transitions between electronic ground states.

1.3 Optical Pumping

The easiest way to polarize an alkali vapor is to use a technique known as Optical Pumping. This technique was first demonstrated in the 1950's and led to the Nobel Prize for Alfred Kastler in 1966. The basic idea behind Optical Pumping is to use the absorption of circularly polarized light to transfer angular momentum to the atoms. Figure 1.1 shows the simplest possible scenario– σ_+ circularly polarized light is tuned close to the J=1/2$\leftrightarrow$J'=1/2 alkali resonance (the D_1 resonance) and sent through the vapor cell. Each photon absorption transfers one unit of angular momentum to the atom. The subsequent transition back to the electronic ground state may or may not conserve angular momentum, but on average, the atomic polarization increases until the rate of angular momentum transfer is balanced by the relaxation rate. This is, of course, a highly simplified picture of Optical Pumping. More detail is given in chapter 2 and in several excellent reviews of the subject (for instance, refs. [Happer72, Happer87]).

1.4 Technological Applications / Spin Exchange Optical Pumping

Once a non-thermal spin distribution is created through optical pumping, it can be put to a variety of interesting scientific and technological uses. However, it is often difficult to use alkali polarization directly. Instead, a noble gas is typically introduced into the cell while the alkali polarization is maintained through optical pumping. After a period of minutes to hours of spin-exchange collisions with polarized alkali atoms, the noble gas nuclei will reach an equilibrium, nonzero polarization. This process is known as Spin-Exchange Optical Pumping (SEOP), and the noble gas produced is called

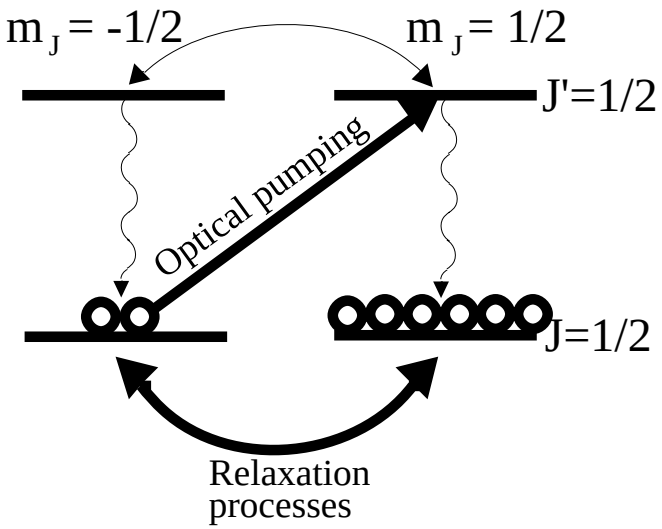

Figure 1.1: Simplified picture of Optical Pumping on D_1 line. The arrow between excited states and wavy arrows represent collisional mixing and de-excitation that is usually present due to buffer gas collisions. Collisional processes tend to return the optically excited atom to either ground state with roughly equal probability, but probability still builds up in the m_J=1/2 ground state due to optical depletion of the m_J=-1/2 ground state.

'Hyperpolarized' to indicate its larger-than-thermal polarization. A detailed description of SEOP can be found in ref. [Walker97].

A hyperpolarized noble gas has three practical advantages over a polarized alkali vapor. First, a noble gas can be introduced into almost any environment, including a living system, without affecting it chemically. Also, noble gases remain gaseous except at very low temperatures, so the nucleus is well isolated from its environment. Therefore, in a suitable container, the noble gas will maintain its polarization for many hours or days. Finally, the heavier noble gases are soluble in a variety of liquids, including blood, and many species are soluble in liquid Xe. This opens up the possibility of polarizing other systems through a similar spin-exchange process ([Fitzgerald98]). For these reasons, it is Spin-Exchage Optically Pumped noble gases that have found direct technical applications in the following areas:

1 Medical Magnetic Resonance Imaging (MRI)

MRI techniques have made enormous progress in the last decade, but the current state of the art still relies on a large magnetic field to polarize protons in the subject. This limits polarization to $O(10^{-6})$. Recently, researchers have shown that having the subject breathe polarized Xe or He can dramatically increase polarization (and therefore signal), particularly for images of lungs (see [Chupp94, Newbury91]). Since Xe is soluable in blood, there is also hope that this technique will lead to more accurate images of other areas such as the brain, and possibly real-time images of circulation and brain function.

2 Surface and Diffusion Studies

The dramatically increased signal from hyperpolarized gases makes surface studies possible with less than a monolayer of adsorbed noble gas. This makes it feasible to investigate crystal surfaces, surface defects and surface reactions with a conventional NMR spectrometer ([Wu90, Raferty91, Jansch98]). In addition, researchers have used this increased signal to study novel diffusion effects, including self-diffusion and the effect of temperature gradients, as well as to measure diffusion coefficients with high accuracy. ([Wolber98, Schmidt97]).

3 Spin-Polarized Targets

The relatively simple nuclear structure of ^{3}He makes it a good target for certain high energy experiments. By hyperpolarizing the target nuclei, one can perform experiments that otherwise require the collision of polarized particle beams. One can thereby simplify the experiment design and increase the interaction rate by many orders of magnitude. This technique was used to make the first measurement of the neutron spin-structure function ([Anthony93]).

4 Quantum Computing

The idea of using quantum states as basic computational elements is at least thirty years old, but it is with Peter Shor's 1985 discovery of a quantum factoring algorithm that the advantages of quantum computing have become clearly apparent. Several realizations of a quantum computer have been proposed, but one of the leading candidates is implemented using NMR techniques on an ensemble of identical molecules in a bulk liquid. Simple computations have already been demonstrated on a thermally polarized liquid ([Linden98]), but it is clear that more complicated work will require the spins to be polarized, most likely through SEOP ([Gershenfeld98]).

Because one needs to maintain a high alkali polarization in order to efficiently polarize other substances, the study of alkali relaxation processes can directly benefit those interested in any of the above areas.

1.5 Brief Description of Experiment

My experimental setup is similar to that of a typical SEOP apparatus. The alkali is contained within a cell of volume $\sim$100 cm^3 with optical access. This cell is then heated (to control alkali vapor density) and a buffer gas or mixture of buffer gases is added from an external manifold. The cell is placed within a uniform magnetic field, as is true for SEOP, but my largest available field is $\sim$1 Tesla, which is much larger than is typically used for that purpose.

I then polarize the alkali vapor using a strong ($\sim$100 mW/cm^3) circularly polarized, pump beam. It typically takes $\sim$100 ms for the alkali atoms to arrive at their equilibrium polarization of $\sim$1%. At this point, I chop off the pumping light and measure the exponential decay of the polarization with a weak ($\sim 10\mu$W/cm^3) probe beam. The exponential decay rate constant is the spin relaxation rate. Much more detail about cell construction and experimental technique is provided in chapter 2.

In order to identify the spin-relaxation mechanism, I vary conditions inside the cell. Specifically, I have mapped out relaxation rates for K, Rb and Cs at vapor pressures from 10^{13} to 5×10^{15} cm^{-3}, using combinations of N_2, H_2 and He as a buffer gas at pressures from 1 to 20000 Torr, magnetic fields from $\sim$1G to 1 Tesla and cells made from aluminosilicate glass and stainless steel/pyrex.

1.6 Brief Summary of Findings

The data over these parameter ranges are well described by a model consisting of four relaxation mechanisms. Other mechanisms are certainly present, but one or more of these four is dominant over all conditions I have investigated, and also at conditions appropriate for SEOP. What follows is a brief description of each of these relaxation mechanisms and its dependence on cell conditions:

1 Relaxation on the Cell Walls.

If an alkali atom collides with the cell wall, it will often stick for a long time (compared to atomic collision times) before returning to the vapor. During this period, it may relax by interacting with other atomic spins in the wall. The relaxation rate due to wall collisions is proportional to the rate at which atoms in the vapor diffuse to the walls; that is, inversely proportional to buffer gas pressure. Our measurements show that, as has been noted before ([Barrat54]), atoms encountering the cell walls are essentially completely relaxed, independent of cell temperature and magnetic field. We may therefore write the wall relaxation rate Γ_{wall} in terms of buffer gas pressure P and vapor temperature T as

$$\Gamma_{wall} = \Gamma_{0,wall}(P_0/P)(T/T_0)^{3/2} \tag{1.1}$$

Γ_0 is a function of the cell size and geometry and possibly also the pump beam geometry.

2 Relaxation due to Alkali-Buffer gas collisions.

Although the interaction time is much shorter, there is a small probability for alkali polarization to be lost during a collision with a buffer gas atom or molecule. As might be expected, this relaxation rate is proportional to alkali-buffer gas collision rate and therefore to buffer gas pressure (unless Van Der Waals molecules are formed as in ref. [Bouchiat71], which does not seem likely in this experiment). It does not depend on alkali density or magnetic field, although there may be a temperature dependence. We may therefore express the relaxation rate due to buffer gas collisions as

$$\Gamma_{buf} = [B]\langle \sigma_{A,B} v_{A,B} \rangle \tag{1.2}$$

for alkali species A and buffer gas B.

3 Relaxation in $^1\Sigma_g^+$ dimers.

In an alkali vapor at densities appropriate for SEOP, approximately 1% of the atoms are in singlet dimers. Because they are paired into a singlet state, there is no net electron polarization to be relaxed, but the nucleus can be relaxed via the electric quadrupole interaction and that depolarization is then transferred to the electron via the hyperfine interaction. This relaxation mechanism has a complicated dependence on the cell conditions, but it is readily calculated and can be used to identify its effects experimentally. Qualitatively, relaxation in singlet molecules increases rapidly with alkali density, decreases with buffer gas pressure and, under certain circumstances, is decoupled by a magnetic field.

I present a model that accurately describes the relaxation rate in singlet molecules in chapter 3. According to this model, the relaxation rate can be calculated from the density of singlet molecules, the cross-section for alkali atom-dimer chemical exchange (σ_{ex}), the cross-section for reorientation of the dimer's angular momentum by collisions with the buffer gas (σ_J), and

the strength of the electric quadrupole interaction in the dimer (Ω_Q). I have determined the latter three quantities experimentally for Rb in N_2. This work is the first direct measurement of alkali relaxation in singlet molecules.

4 Alkali-Alkali relaxation.

The final relaxation mechanism I have measured is thought to arise from alkali-alkali interactions because it scales very nearly linearly with alkali density. Until recently, the microscopic explanation was thought to be alkali-alkali binary collisions [Bhaskar80, Knize89, Chupp94], which can successfully reproduce the alkali density dependence. However, in studying this relaxation process, I have shown that it can be largely decoupled by applying a ∼kG magnetic field. For reasons I discuss in the next section, this observation rules out the previously accepted explanation, but I have been unable thus far to show definitively what the microscopic cause of alkali-alkali relxation is. As of this writing, it appears that relaxation in alkali trimers is the leading candidate. Since three body problems are notoriously difficult to handle theoretically, and hot trimers are nearly impossible to detect experimentally, verifying this supposition is a formidable task. I have characterized this relaxation mechanism experimentally, however, and find that it is well represented by

$$\Gamma_{alk} = (\kappa_A + \frac{\kappa_B}{1+(B/B_0)^2})[A]$$
$$\text{where} B_D = B_{D,0}\sqrt{1+(P/P_D)^2} \tag{1.3}$$

Note that each of these mechanisms has a different dependence on conditions inside the cell, which makes it possible to separate them out experimentally and study each individually. Over the large range of parameters investigated by myself and others, the four processes listed above appear to be independent of each other. Therefore, the total relaxation rate is simply the sum of the rates due to these four processes and we may write the relaxation rate Γ as

$$\Gamma = \Gamma_{buf} + \Gamma_{wall} + \Gamma_{sing} + \Gamma_{alk}. \tag{1.4}$$

	K	Rb
He		1.3×10^{-23} (520K) (*)
		5.3×10^{-24} (380K) ([Baranga98])
		1.0×10^{-23} (450K) ([Baranga98])
N_2	7.9×10^{-23} (440 K) (*)	2.0×10^{-22} (480K) (*)
		2.5×10^{-22} (520K) (*)
H_2		1.7×10^{-23} (500K) (*)
		2.4×10^{-23} ([Brewer62])

Table 1.1: measured values for $\sigma_{A,B}$ (in s^{-1}). (*) indicates this work. See ref. [Happer72] for measured cross-sections involving Cs. See ref. [Walker97] for measurements and theoretical estimates of alkali-noble gas cross-sections.

	κ_A	κ_B	$B_{0,D}$	P_D
K (nat.)	7.5×10^{-15} (*)	8.2×10^{-15} (*)	230 (*)	1700 (in N_2) (*)
	$\kappa_A+\kappa_B=3.0\times10^{-14}$ ([Knize89])			5800 (in He) (*)
Rb (nat.)	1.50×10^{-14} (*)	2.6×10^{-14} (*)	1150 (*)	>15000 (*)
	$\kappa_A+\kappa_B=7.3\times10^{-14}$ ([Knize89])			
^{85}Rb			1010 (†)	
^{87}Rb			1450 (†)	
Cs (nat.)	1.9×10^{-13} (*)	1.8×10^{-13} (*)	2900 (*)	
	$\kappa_A+\kappa_B=4.1\times10^{-13}$ ([Bhaskar80])			

Table 1.2: measured values for κ_A, κ_B (in cm^3/s), B_0 (in G) and P_D (in Torr). (*) indicates this work. (†) indicates recent, unpublished measurements by Christopher Erickson and William Happer at Princeton University.

Thus, the relaxation depends on the parameters $\Gamma_{0,wall}$, $\sigma_{A,B}$, κ_A, κ_B, $B_{0,D}$, P_D, σ_{ex}, σ_J and Ω_Q, to be determined experimentally. $\Gamma_{0,wall}$ is function of cell geometry and is therefore not of fundamental interest (except as a measurement of diffusion coefficients), but I have listed the measured values for all the other coefficients in tables 1.1-1.3. To put these numbers into perspective, I have included figure 1.2, which shows the cell conditions under which each of the above four relaxation mechanisms becomes important.

	σ_{ex}	σ_J	Ω_Q
Rb	$173(35)\mathring{A}^2$	$12(2)\mathring{A}^2$	80(8) KHz (^{85}Rb) 130(13) KHz(^{87}Rb)

Table 1.3: measured values for σ_{ex}, σ_J and Ω_Q.

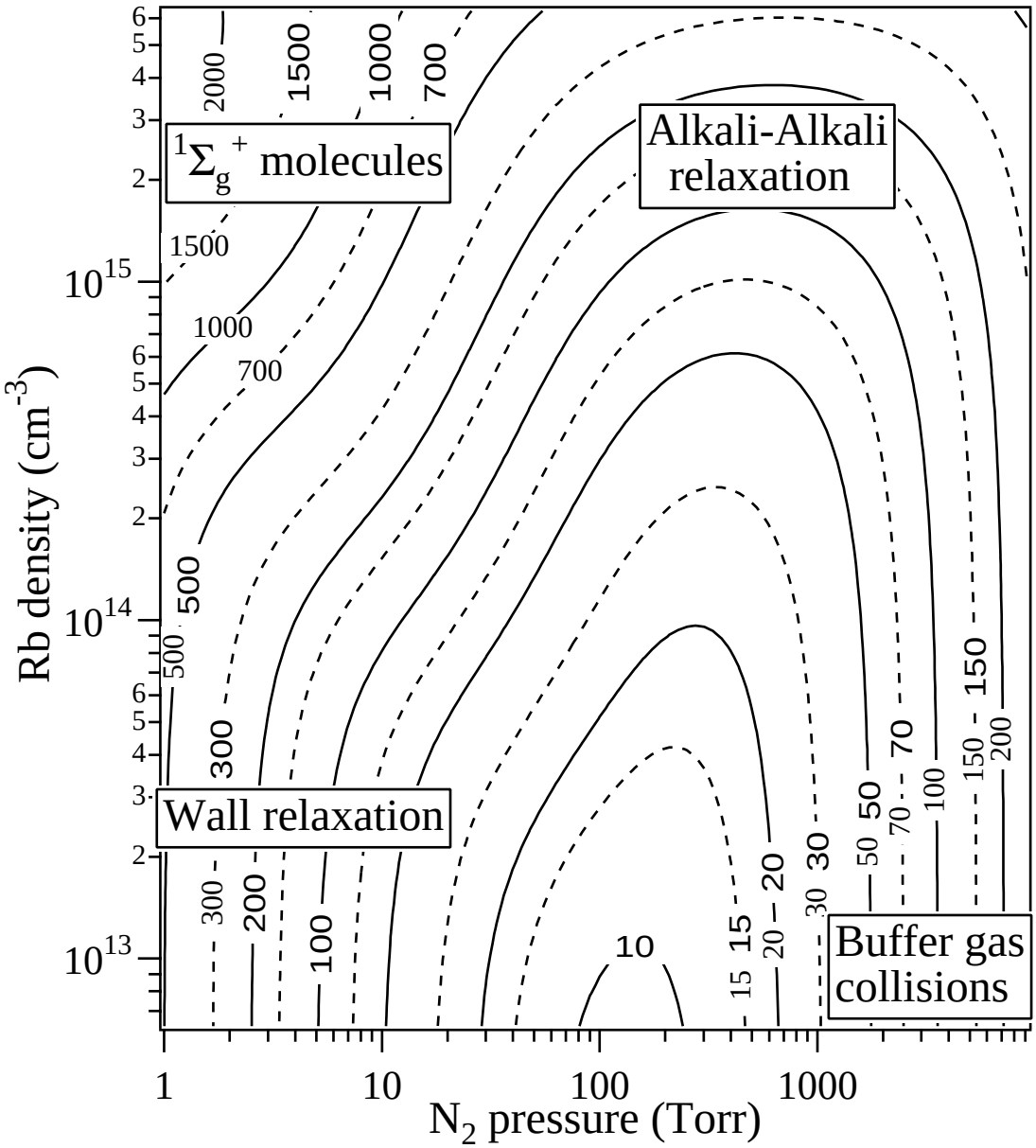

Figure 1.2: Relaxation rate for Rb in N_2 as a function of N_2 pressure and Rb density. The contours shown are relaxation rate at low magnetic field in s^{-1}. The text inserts show the region of phase space in which each of the four relaxation mechanisms are dominant.

1.7 Overview of Alkali-Alkali Relaxation

Because of its detrimental effects on SEOP and the opportunity to probe new dynamical processes in the alkali vapor, the bulk of my experimental work has been directed toward measurements of alkali-alkali relaxation in the different alkalis and developing a consistent microscopic theory of this mechanism. The way we have chosen to attack this problem is to consider each possible relxation mechanism in increasing order of complexity. Since, to the best of our knowledge, the cell consists only of walls, alkali, buffer gas and a magnetic field, the relaxation must be coming from an interaction between an alkali atom and one or a combination of these four. I have enumerated possible relaxation processes below. I give a brief assessment of each, along with references in this dissertation for additional information:

1 Interactions Between Alkalis and the Wall.

Interactions with the cell wall are clearly not the cause of alkali-alkali relaxation because the relaxation rate is often much larger than the diffusion rate. Thus, an alkali atom is relaxed before it has a chance to encounter the wall.

2 Interactions Between Alkalis and the Magnetic Field.

Because the polarization axis and the magnetic field direction are colinear, a constant magnetic field can not cause relaxation, although a time varying magnetic field or diffusion through magnetic field gradients may. We have eliminated this as a possible source of relaxation because it would not have the observed pressure independence or alkali density dependence, and it would require much larger inhomogeneity than is present in our magnet.

3 Interactions Between Alkalis and the Buffer Gas.

These interactions are already well studied and characterized, and they do not have the observed pressure independence and alkali density dependence.

4 Interactions Between Two Alkalis (binary collisions).

When two alkali atoms interact without the presence of a third body, the interaction time is typically no more than a few ps (under certain conditions,

a resonant collision may lead to longer interaction times, but such collisions are quite rare). Since the precession of any atomic spin around a kG magnetic field takes much longer than that, we should not expect the application of a field to change the observed relaxation rate. Thus, the observation of a field dependence to this relaxation mechanism eliminates alkali-alkali interactions as a possibility. For a more detailed argument, along with an estimate of resonance effects, see chapter 5 and section 6.6.

5 Interactions Between Two Alkalis and the Buffer Gas (stable dimers).

If two alkali atoms collide in the presence of a third body, a stable dimer may be formed. Singlet dimers, bound by about 0.5 eV are by far the more numerous, but triplet dimers (bound by about 0.03 eV) are present as well. Relaxation is possible in either species. I have measured relaxation in singlet molecules and find that, in agreement with a theoretical treatment, relaxation becomes negligible at pressures above a few hundred Torr. Because of its nonzero electron angular momentum, relaxation could proceed quickly in triplet dimers through the anisotropic spin-spin interaction ([Mies96]), in which electron angular momentum is coupled to the rotation of the two alkali atoms around each other. However, the expected relaxation rate should depend on trimer formation, destruction and angular momentum reorientation, each of which is sensitive to buffer gas pressure. I have done extensive modeling of this interaction and find no way to reproduce the observed pressure independence of alkali-alkali relaxation. We therefore reject alkali-alkali-buffer gas interactions as the source of this relaxation. See chapter 3 for further discussion of relaxation in singlet dimers, and chapter 6 for triplet dimers.

6 Interactions Between Three Alkalis (metastable trimers).

The reactive collision between an alkali atom and an alkali singlet dimer is a fascinating and well studied problem. As one would expect from energy considerations, the products are almost always an atom and a dimer, but the three atoms can stay together in a metastable complex for a surprisingly long time– hundreds of ps or even ns dwell times are not uncommon. This is

long enough to explain our magnetic field measurements, and the reaction is common enough to explain the measured relaxation rates. In addition, the expected alkali density dependence is consistent with our measurements. I therefore consider metastable trimers to be the structure in which alkali-alkali relaxation is most likely taking place. See chapter 7 for more detail.

7 Interactions Between Four Alkalis or Three Alkalis and the Buffer Gas (stable trimers).

A stable alkali trimer may be formed by any of the following reactions (A refers to an alkali atom, B to a buffer gas atom or molecule):

$$
\begin{aligned}
I. \quad & A + A + A + B \rightarrow A_3 + B \\
II. \quad & A + A_2 + B \rightarrow A_3 + B \\
III. \quad & A + A_3 \rightarrow A + A_3 \quad \text{(chemical exchange)} \\
IV. \quad & A_2 + A_2 \rightarrow A + A_3
\end{aligned}
$$

I have estimated alkali density and buffer gas pressure dependences for the above processes (see chapter 7) and I do not find them to be in agreement with measured alkali-alkali relaxation rates.

The above list shows how we have attempted to understand alkali-alkali relaxation– by eliminating all the simpler possibilities, we are left to consider the exotic mechanisms involving metastable alkali trimers. Processes involving more than three alkali atoms can be neglected because they are very rare in all but extremely high density vapors.

1.8 Direct Applications Of This Work

Under conditions suitable for Spin-Exchange Optical Pumping, I find that alkali-buffer gas collisions and alkali-alkali relaxation dominate the relaxation rate. Unfortunately, little can be done to reduce alkali-buffer gas collisions, because another gas needs to be present as a spin-exchange partner (and to avoid rapid alkali diffusion). However, the discovery of magnetic decoupling of alkali-alkali relaxation may have important consequences, because this mechanism accounts for much of the relaxation present in a

SEOP apparatus. I estimate that by applying a magnetic field of a few kG, a typical large-scale SEOP apparatus can increase its production rate by at least factor of 2.

Chapter 2

Experimental Design

This chapter describes my experimental apparatus and how it is used. In section 2.1, I describe the light sources used to optically pump and probe the alkali vapor (2.1.1), explain how the cell is constructed (2.1.2) and show how the polarization is detected and averaged (2.1.3). Section 2.2 shows how these elements are put together to make a relaxation rate measurements. Finally, I describe two methods for measuring the alkali vapor density– using absorption spectroscopy (2.3.1) and Faraday rotation (2.3.2).

2.1 Experiment Overview/Diagrams

2.1.1 Light Sources

In order to measure relaxation rates, I first polarized the alkali vapor with a strong (100 mW – 1W), circularly polarized laser beam (the pump beam). This brings the vapor into a new equilibrium, with a polarization of $\sim$1%. I then turned off the pump beam suddenly and measured the subsequent decay of polarization with a weak ($\sim 1\mu$W) laser beam (the probe beam). I kept the probe intensity sufficiently low that it did not significantly affect the polarization of the vapor. A diagram of this setup is shown in fig. 2.1.

Typically, I used an Ar^+ (Spectra Physics model 171) pumped Titanium:Sapphire laser (Spectra Physics model 3900) as both pump and probe beam. This laser was typically detuned about 1 nm from either the D1 or D2 atomic resonance, although I used detunings from 0.2 to 40 nm, depending on cell conditions (detunings mea-

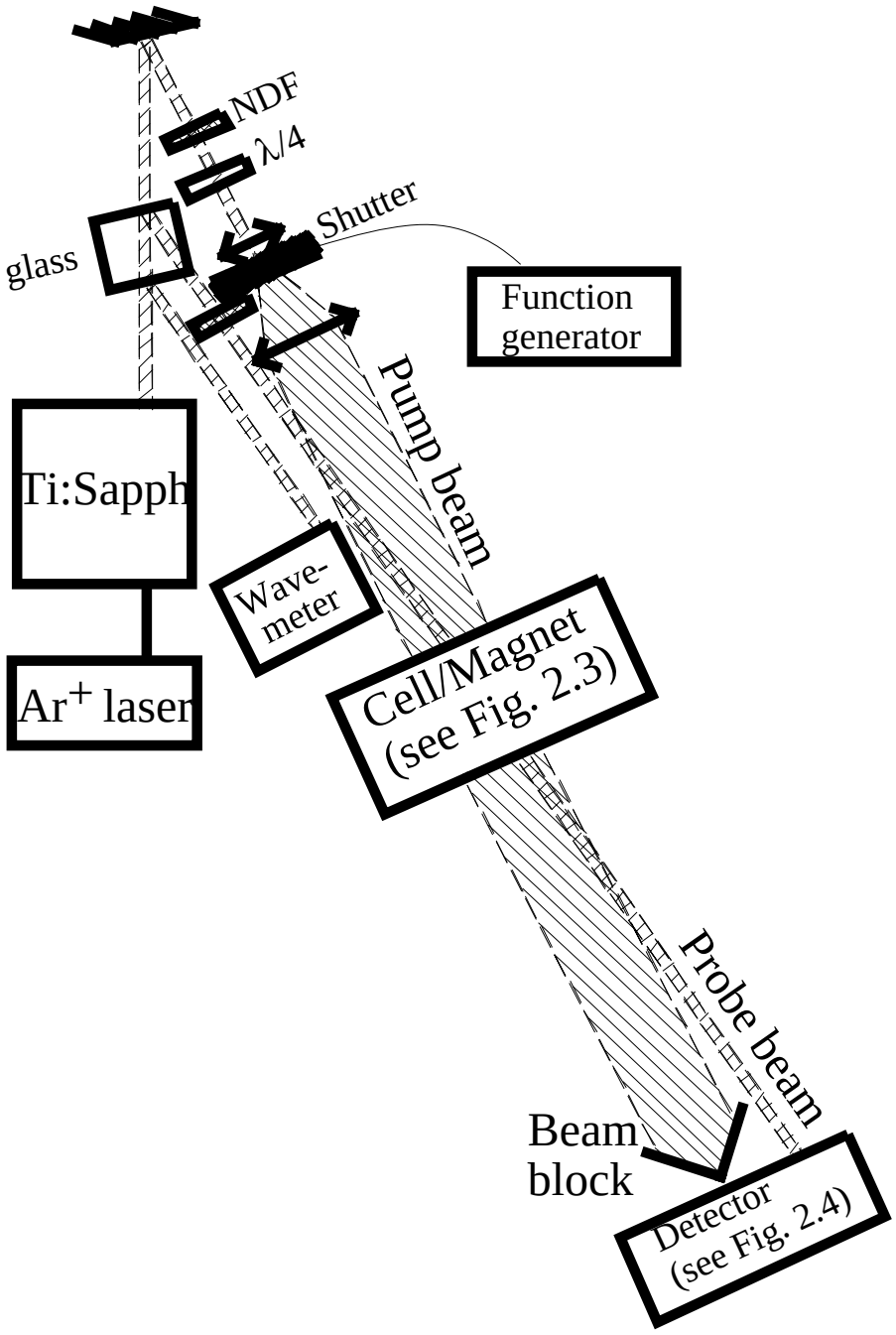

Figure 2.1: Functional diagram of the experiment for relaxation rate measurements, showing the light sources and optics.

sured using a Burleigh WA-1500 or New Focus model 7711 Fizeau wavemeter). The Ti:Sapph linewidth was approximately 30 GHz. I also made measurements using an Optopower OP-A015-795 (∼2 nm. linewidth, up to 15W power) or a Microlase MBR-110 Ti:Sapph (100 KHz linewidth, ∼300 mW power) as the pump laser, and used a grating-stabilized diode laser (100 kHz linewidth, 20 mW Power, constructed in the manner of ref. [Wieman91]) as the probe beam. The measurements presented here do not depend on the light sources or detunings used (although for the reasons described in appendix A, the results are hard to interpret at very small pump or probe detuning). I used neutral density filters (NDFs) to attenuate both pump and probe to the desired intensity and chopped the pump beam with a Uniblitz model 136ZM2 mechanical shutter (full-on to full-off in 0.5 ms).

2.1.2 The Cell

The alkali vapor was typically contained inside a stainless steel cell, although I took measurements in all-glass cells as well, to verify that the stainless steel had no effect on the measured relaxation rate. The exact size and shape of the cell depended on the pressure, alkali density and magnetic field conditions desired, but the nearly all the measurements presented here were done using one of the four cells shown in fig. 2.2. As a rule, the smaller cells were used for high pressure (where diffusion presents minimal difficulty) and high magnetic field (to fit between the pole faces of the magnet). All of the work with Cs was done in the cell shown in fig. 2.2c.

Much of this work required the buffer gas pressure or species to be changed. I accomplished this by attaching the cell to a gas manifold as shown in fig. 2.3, which contained gases of 99.999% purity. I measured the pressure using a mechanical gauge and a series of capacitance manometers (Baratron model 0BHS-2A3-B-1 for pressures up to 1 Torr, Varian model BGG22300 for pressures up to 1000 Torr and Baratron model 122AA-10000BB for pressures up to 10000 Torr).

The windows of the stainless steel cells were affixed in the manner of ref. [Noble94]. I used plain pyrex circles (2" diameter x 3/8" thick) for the windows and 30-40 sheets of aluminum foil as a pad between the window and the stainless retaining ring. For high pressure work, I found that the cell survived much longer if I tightened the bolts to ∼60 in-lb, as compared to the ∼36 in-lb used by ref. [Noble94]. The window attach-

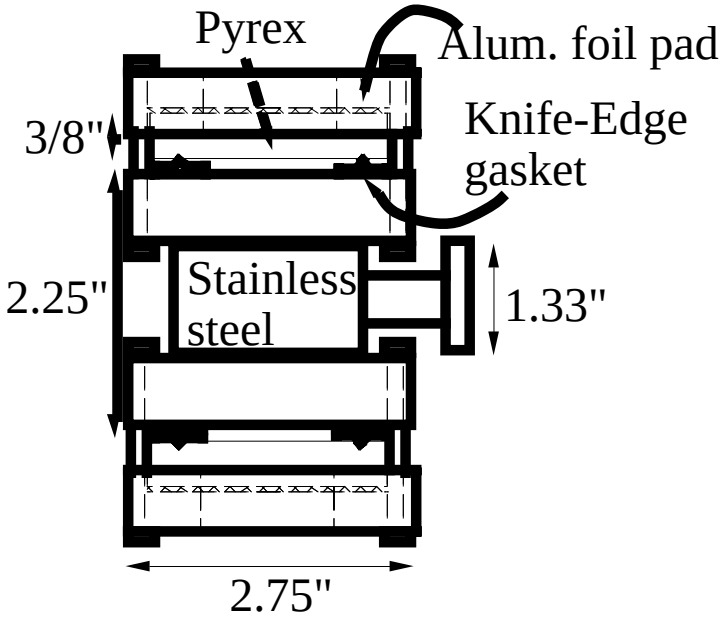

Figure 2.2a

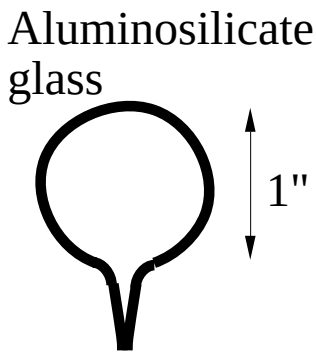

Figure 2.2b

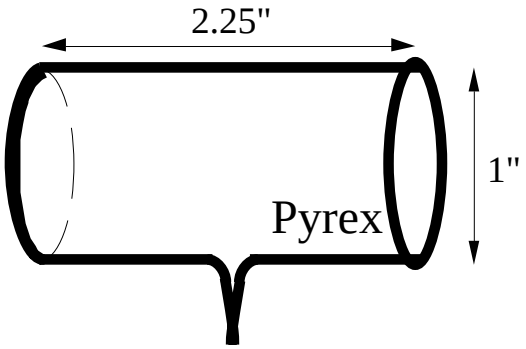

Figure 2.2c

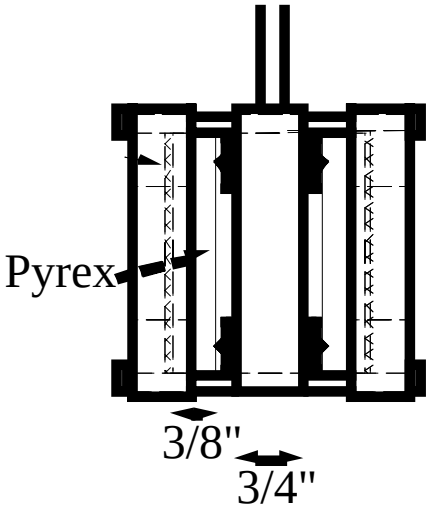

Figure 2.2d

Figure 2.2: Cells used to contain the alkali vapor for relaxation rate measurements.

ment procedure is otherwise identical to that described in the reference, including the machining of the copper knife-edge gaskets. These windows successfully held pressure from 10^{-9} Torr to 20 atmospheres. The seal also withstands alkali attack quite well, although the windows themselves deteriorate over a period of about a month until they are too opaque to be useful.

I placed the cell inside an high-temperature ceramic fiberboard oven with optical access and attached it to a gas manifold as shown in fig. 2.3. To prevent the alkali from escaping, the cell was valved off inside the oven, and I kept this valve closed whenever the oven was on, except for brief periods to change the buffer gas pressure or composition. The oven was heated with space heaters and heater tape, which produced stray fields on the order of a few mG at the alkali sample. I checked that the neither position of the heaters nor whether AC or DC current is used has any effect on the measured relaxation rate.

Finally, I placed the oven between the pole faces of a water-cooled NMR magnet (Ventron model 1365) which can produce a field of approximately 1.2 Tesla over a 3" high by 5" diameter cylinder. Alternatively, one can remove the pole faces, which reduces the maximum field to 6 kG, but increases the volume to 6.5" high by 5" diameter. In either case, the field is constant to at least a few percent over the available volume, despite holes that have been drilled in the pole faces to allow optical access. This is an upper limit based on my inability to detect field gradients with a Bell model 610 Gaussmeter.

2.1.3 Polarization Detector

An atomic vapor affects near-resonant light in several ways, which can be used to monitor the polarization. For most measurements, I used the setup shown schematically in fig. 2.4a, which takes advantage of the rotation of a linearly polarized probe beam. I sent this beam nearly colinear to the pump beam such that the two beams overlapped in the cell. The probe then passed through a $\lambda/2$ plate and a polarizing beamsplitter. I rotated the $\lambda/2$ plate until equal amounts of light were sent through each arm of the beamsplitter and therefore onto two balanced photodetectors, giving a null signal when the vapor was unpolarized. Subsequent changes in vapor polarization cause the probe beam's polarization axis to rotate by an angle proportional to the vapor polar-

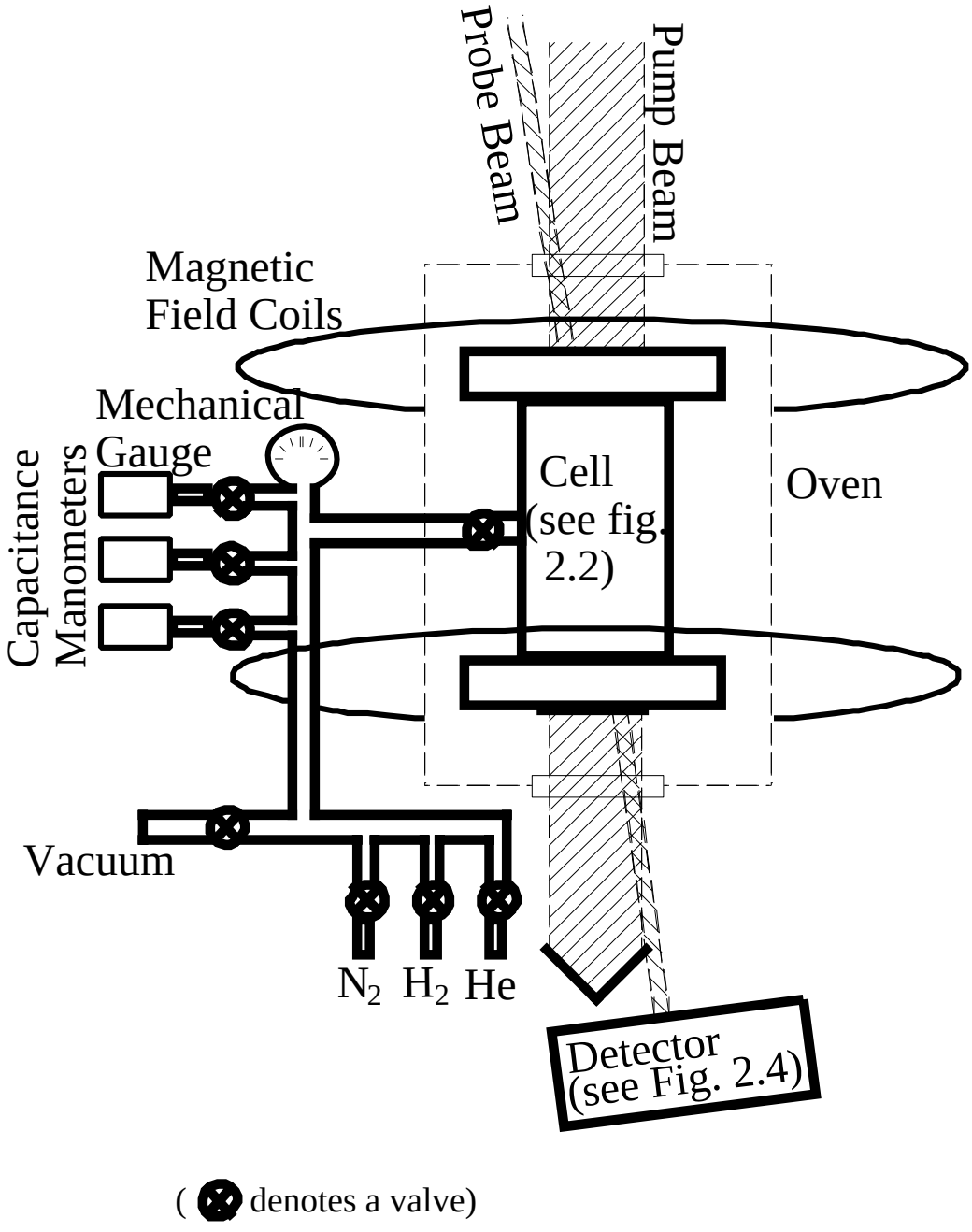

Figure 2.3: Functional diagram of the experiment for relaxation rate measurements, showing the gas manifold, cell positioning and magnet.

ization P (see Appendix A for the theory behind this effect) and the current from the photodetectors is proportional to $\sin(P)$. By adjusting the probe detuning, I kept the maximum rotation angle to a few degrees, so that $\sin(P) \approx P$. The photodetector current was then amplifed and sent to an oscilloscope, yielding a signal proportional to vapor polarization. This setup has extremely good sensitivity. In addition, it provides excellent common-mode laser amplitude noise rejection.

Under certain cell conditions, however, it may be impossible to remain in the small angle regime if one wishes to use the same laser for both the pump and probe beams. Some measurements therefore required the detector shown in fig. 2.4b, which takes advantage of the change in absorption of a circularly polarized probe as the atomic vapor polarization is changed (again, see Appendix A).

The absorption of circularly polarized light has a standard Beer's law form $I(z) = I_0 e^{-z/z_0}$. To simplify the analysis, I kept the probe detuning large enough that z_0 was much larger than the cell length whever possible to maintain the linearity of the detector (this is the equivalent of the small angle approximation above). In order to verify that my polarization detection was accurate and linear, I took care to compare the two detection methods periodically. The measured relaxation rate did not depend on which method was used.

For both setups, I found it advantageous to put the photodiodes in a light-tight box. I focused the probe light through a pinhole in the box (to minimize stray pump light), and put red filter glass in front of the hole (to minimize other stray light).

2.2 Relaxation Rate Measurements

Combining the pump/probe techniques described above gives a relaxation rate transient similar to the one shown in fig. 2.5. I recorded the transients with a Lecroy model 9304 digital oscilloscope. A single relaxation transient was almost always too noisy to be useful, so I would usually average between 100 and 5000 pump/relax cycles recorded with identical cell conditions (fig. 2.5 is actually the result of such averaging). The measured relaxation rate is then the time constant of an exponential fit to the averaged transients. As long as I met the conditions of small absorption/rotation angle and small polarization fraction (to avoid complicating nuclear effects– see appendix B), the exponential fit was always excellent, subject to the limits of experimental noise.

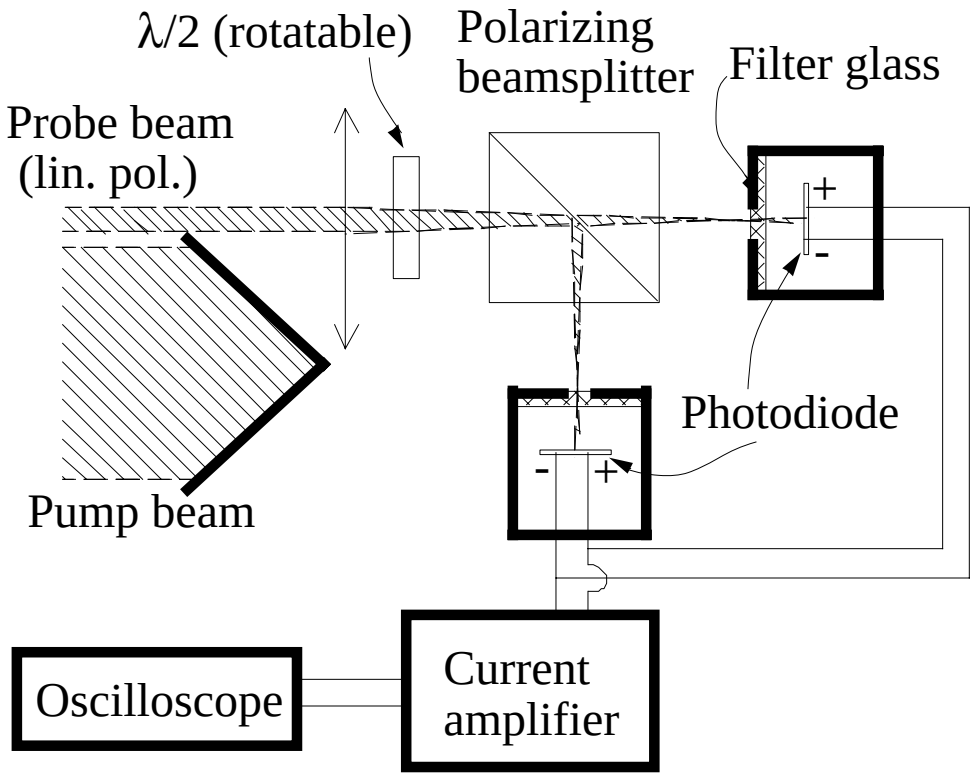

Figure 2.4a: Detector setups for monitoring probe Faraday rotation

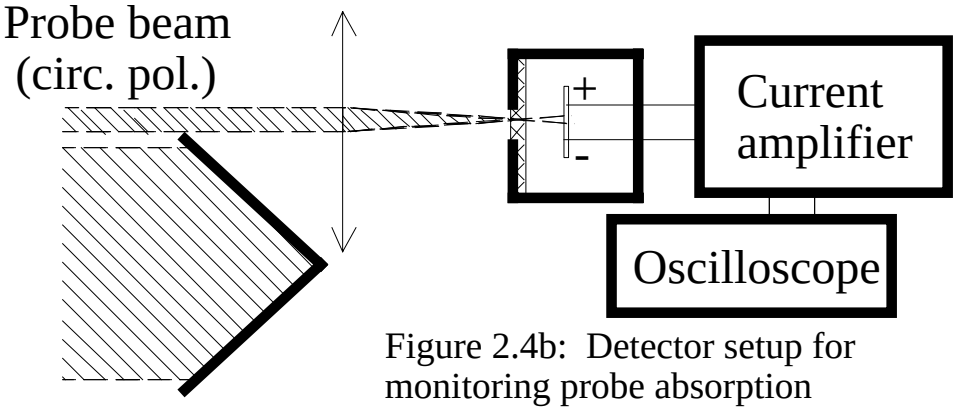

Figure 2.4b: Detector setup for monitoring probe absorption

Figure 2.4: Polarization-sensitive detectors.

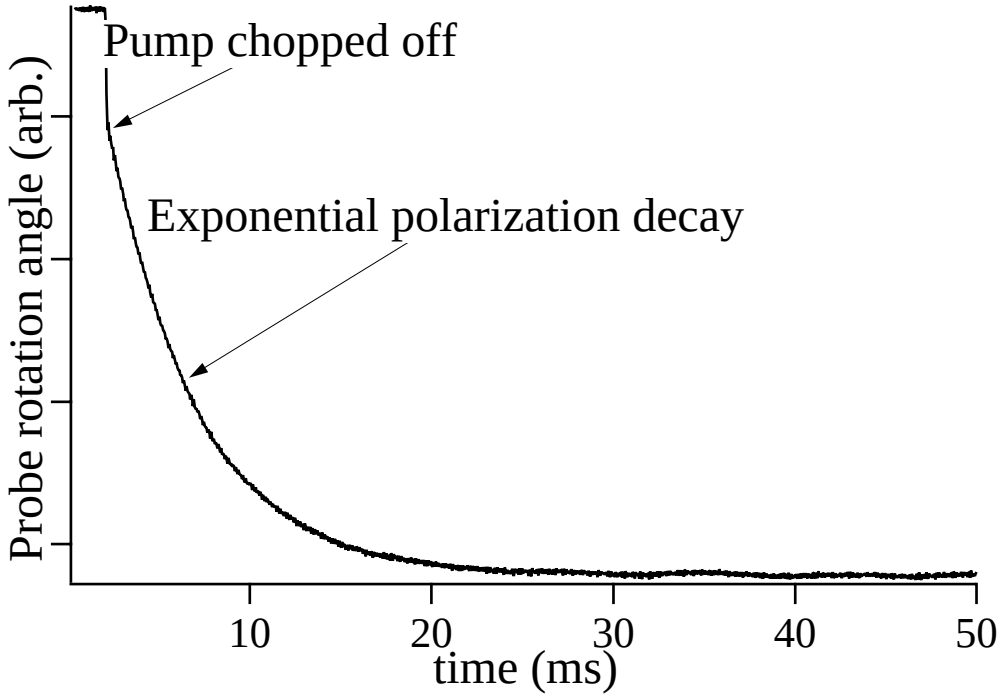

Figure 2.5: Sample spin-relaxation transitient.

My experiment consisted mainly of measurements like this. It is impossible to determine the cause of spin-relaxation by looking at a single relaxation transient, so my strategy was to vary the cell conditions (buffer gas pressure and composition, alkali species and density, and magnetic field) and compare the relaxation rate's dependence on these conditions to theoretical predictions. I also varied other experimental parameters, such as pump and probe intensity, helicity, linewidth and beam shape, electronics and detector proximity to the magnetic field and cell composition, to verify that the measured rates were not due to experimental artifacts.

2.3 Vapor Pressure Measurement

In order to identify the source of alkali relaxation, it is necessary to have an accurate measurement of alkali vapor density. Ideally, this would be accomplished with a sensor placed inside the cell, but I know of no sensor that would survive the extremely corrosive conditions. The simplest alternative is to measure the temperature on the outside of

the cell, using multiple sensors, and estimate the vapor density using the published vapor pressure curves (see Appendix A). I found this to be unreliable, although I am not sure what the source of the error is. One possible explanation is the difficulty I had in avoiding large temperature gradients and radiative heating of the temperature sensors in such a small oven. Additionally, the alkali may fail to reach its quoted vapor pressure due to the presence of buffer gas and the composition of the cell walls. I therefore settled on two direct optical methods of determining alkali vapor pressure– absorption spectroscopy and Faraday rotation.

2.3.1 Absorption Spectroscopy

This technique is based on the following relation for the integrated absorption cross-section across one of the atomic spectral lines

$$\int_{-\infty}^{\infty} \sigma(\nu) d\nu = \pi r_e f c. \tag{2.1}$$

The absorption cross-section $\sigma(\nu)$ can be written in terms of the alkali density [A] and the $1/e$ absorption length $l(\nu)$ as $\sigma(\nu) = ([A]l(\nu))^{-1}$. In the special case of a Lorentzian lineshape, we can parameterize σ as

$$\sigma(\nu) = \left[[A]l_0 \left(1 + (\frac{\Delta}{\Delta_0})^2\right)\right]^{-1}, \tag{2.2}$$

where l_0 is the $1/e$ absorption length at line center. Equation 2.1 can be easily integrated, giving

$$[A] = \frac{\Delta_0}{l_0 r_e f c} \tag{2.3}$$

(Δ_0 is the detuning in frequency, not angular frequency). We can therefore arrive at the alkali density by measuring l_0 and Δ_0. The oscillator strengths f are given for all alkali species and transitions of interest in ref. [Migdalek98].

I first attempted to measure l_0 and Δ_0 for the most experimentally convenient transition, the D_1 line. Since our spin relaxation measurements must take place at high alkali densities (usually $10^{14} - 10^{16}$ cm^{-3}), l_0 for this transition is of order 0.1 - 1 mm. Therefore, no detectable light penetrates the cell within several linewidths of the resonance and I am dependent on absorption measurements in the far wings.

Unfortunately, the wings are broadened in a quasistatic interaction with the buffer gas which depends on buffer species and pressure, and is insufficiently well characterized for this purpose. This leads to unacceptable error in determining l_0 and Δ_0.

I avoided this uncertainty by choosing a weaker transition, the $J = \frac{1}{2} \rightarrow J' = \frac{3}{2}$ transition in the second doublet of the alkali principal series. The oscillator strengths for this transition are typically two orders of magnitude smaller than those of the first resonance, so l_0 is well matched to our cell size for alkali densities of interest. This leads to the following relationships between alkali density, Δ_0 and l_0:

$$\begin{aligned} [K] &= 21360 \text{ cm}^{-3} \left(\frac{\Delta_0}{Hz}\right) \left(\frac{\text{cm}}{l_0}\right) \\ [Rb] &= 12400 \text{ cm}^{-3} \left(\frac{\Delta_0}{Hz}\right) \left(\frac{\text{cm}}{l_0}\right) \\ [Cs] &= 10480 \text{ cm}^{-3} \left(\frac{\Delta_0}{Hz}\right) \left(\frac{\text{cm}}{l_0}\right) \end{aligned} \tag{2.4}$$

Working at the second resonance requires tunable light in the visable blue to near UV range, which I produced by frequency doubling the Ti:Sapph laser. The experimental setup is shown in fig. 2.6. The following description is for work at the second resonance of potassium, but is applicable to Rb and Cs as well by changing the frequencies and phase matching conditions. See, for example, ref. [Arecchi], p. 941 for a description of phase matching and indices of refraction for common doubling crystals.

Using a 1 cm cube $LiIO_3$ crystal, I doubled approximately 500 mW of 808 - 810 nm to fully resolve the $4s_{1/2}$-$5p_{1/2}$ and $4s_{1/2}$-$5p_{3/2}$ resonances. The incident red light had a bandwidth of approximately 8 GHz and since the doubled spectral intensity is proportional to the square of the incident spectral intensity, I expect that the doubled light was significantly narrower. My crystal was cut with a 38 deg. angle between the optical axis and one set of faces, so phase matching requires that the incident light make a 14.1 deg. angle with the normal to those faces. The incident light was polarized in the ordinary/extrordinary plane and was focused inside the crystal with a f=15 cm lens. This produces approximately 1-5 μW of blue light polarized in the ordinary/ordinary plane. I corrected the significant astigmatism of the blue light with a f=8 cm cylindrical lens and sent it down a 5 m multimode fiber over which it became unpolarized. The transmission measurement is scaled by the intensity at a reference photodiode, right before the cell. This is necessary to eliminate intensity fluctuations as the Ti:Sapph is

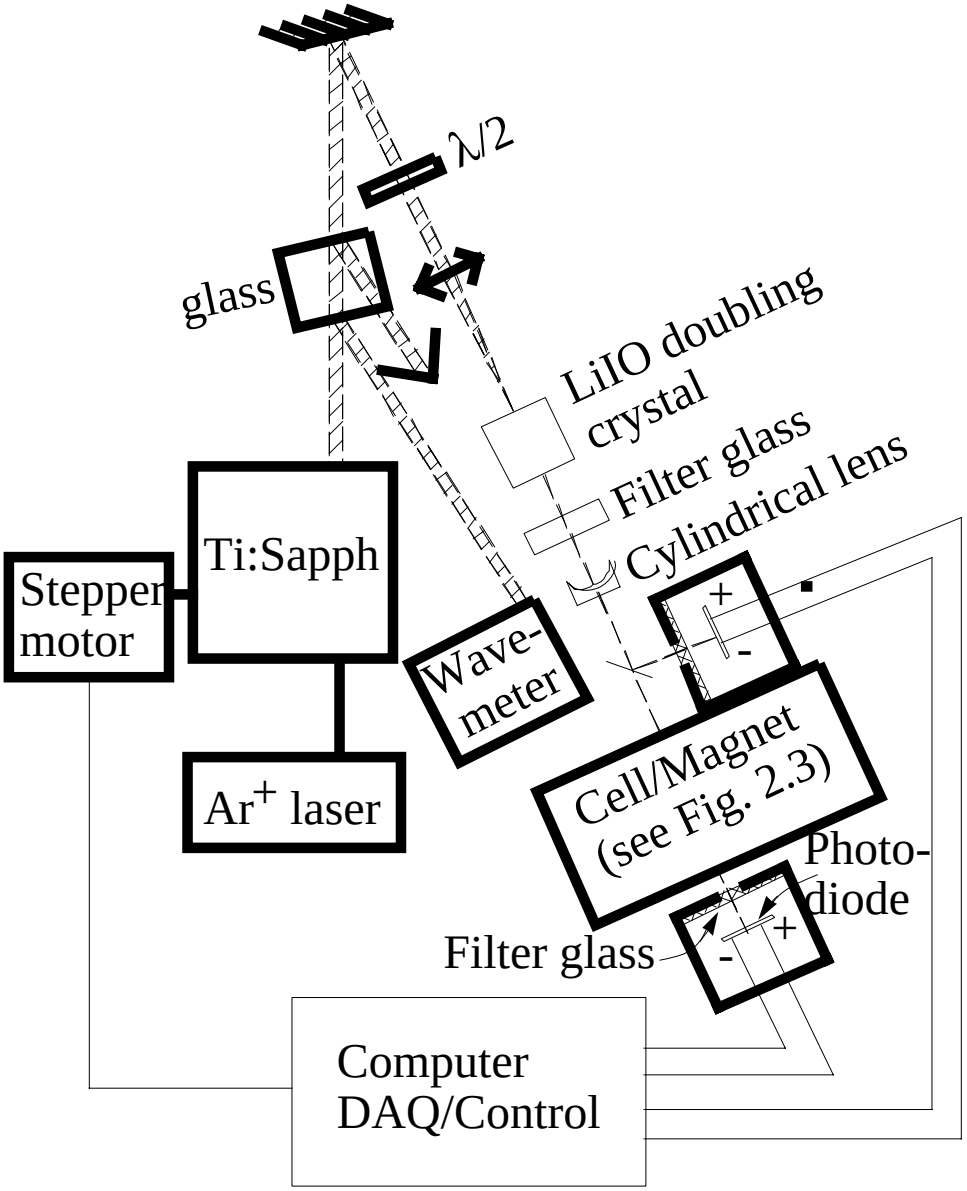

Figure 2.6: Functional diagram of experiment for vapor pressure measurement by absorption spectroscopy.

scanned.

Typical absorption spectra along with the extracted [K] are shown in fig. 2.7. I sweep the blue light across both resonances of the doublet in order to accurately fit to two Lorentzian lines as well as to verify that the presence of the buffer gas does not redistribute oscillator strength between the two. It is interesting to note that although the oscillator strengths have the same ratio as in vacuum (2.16 for K, 2.34 for Rb and 4.23 for Cs), the $s_{1/2}$-$p_{3/2}$ shows much more pressure broadening than the $s_{1/2}$-$p_{1/2}$ transition.

2.3.2 Faraday Rotation

The above technique is very accurate and easy to interpret theoretically, although it is time consuming to align. In addition, its accuracy is diminished for alkali densities below about 10^{14}cm^{-3} (where the absorption is too small to detect reliably) and above about $3\times10^{15}\text{cm}^{-3}$ (where the optical thickness starts to present the same problems as discussed above for the D1 line). I therefore used the Faraday rotation of linearly polarized light, which is proportional to vapor density, for most of my vapor pressure determinations. I discuss the quantitative theory of Faraday rotation in Appendix A, but a very useful approximation for this work can be found in [Wu86]– the amount by which linearly polarized light rotates θ (in radians) as one changes the magnetic field by B is determines the alkali vapor density $[A]$ as

$$[A] = \frac{18\ c\ \theta}{[4/(\Delta\lambda_{1/2})^2 + 7/(\Delta\lambda_{3/2})^2] r_e \lambda^4 l \mu_B B/h} \tag{2.5}$$

in which $\Delta\lambda_J$ is the wavelength detuning to the component J of the first fine structure doublet and l is the length of the light path through the cell. This expression is remarkably independent of buffer gas pressure.

A typical rotation spectrum is shown in fig. 2.8, along with a fit to the above form plus a rotation offset (caused by optical activity in the cell windows). The fit is quite good except for a small deviation between the two resonances. I do not know the source of this deviation, although it does not appear to be due to the buffer gas. It also appears to scale with the rotation angle as the vapor pressure is changed, which suggests it is not due to alkali-alkali broadening or alkali dimers. In order to minimize the effect of

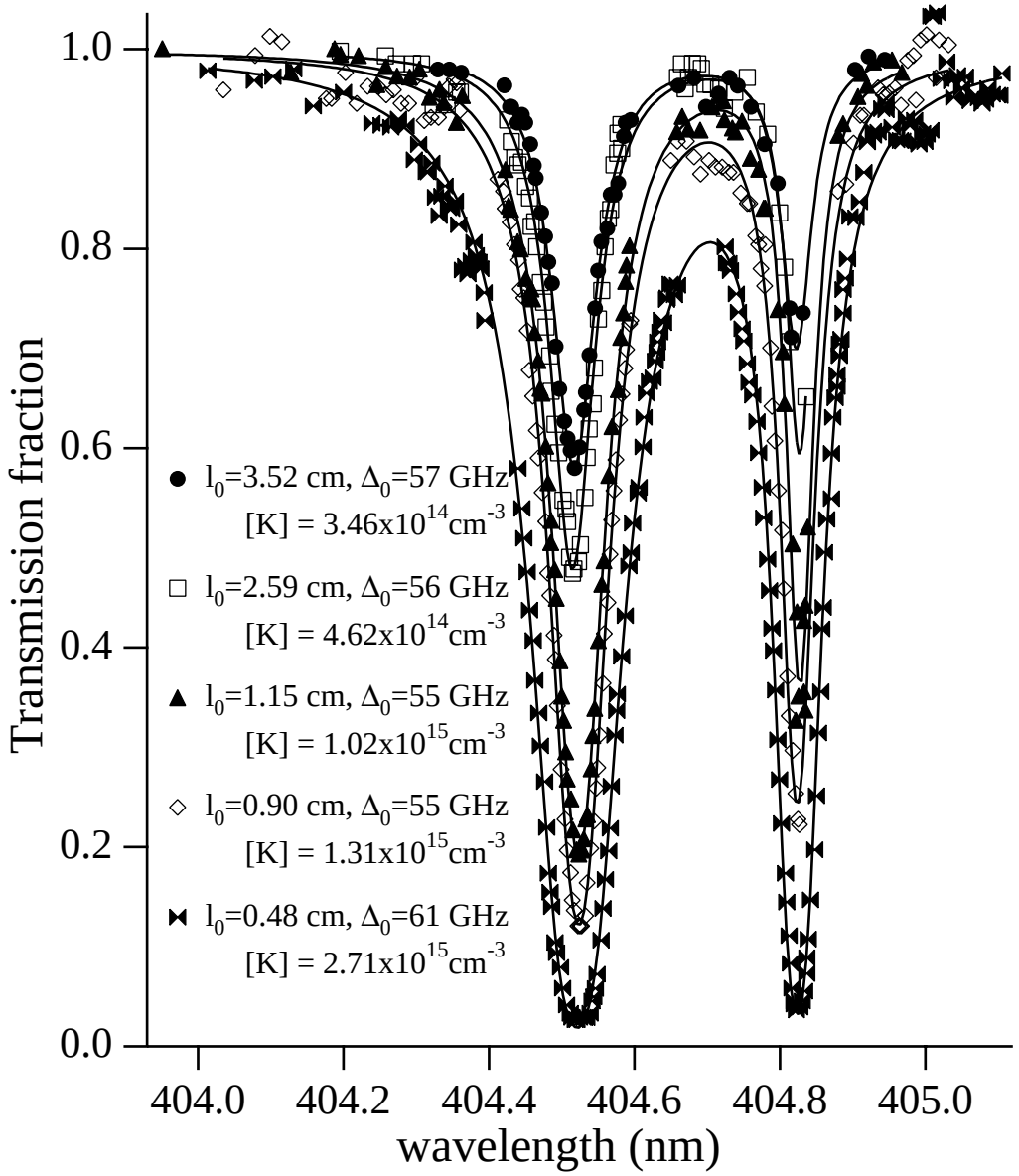

Figure 2.7: Absorption of blue light at the K second resonance. The fits are to the form exp(-g(ω)) where g(ω) is a sum of two Lorentzian lineshapes, one centered on the $4s_{1/2}$-$5p_{1/2}$ resonance and one centered on the $4s_{1/2}$-$5p_{3/2}$ resonance

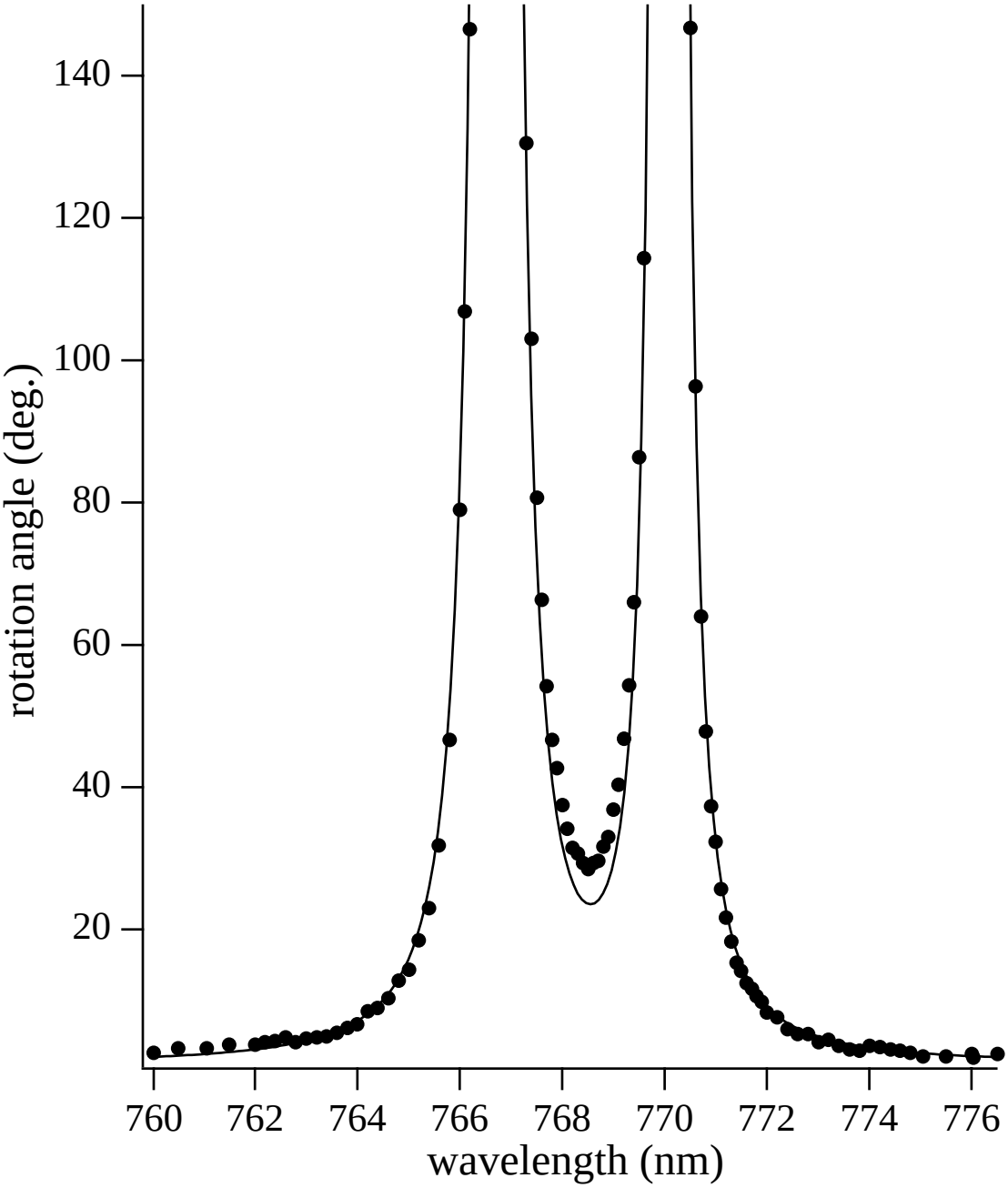

Figure 2.8: Faraday rotation of light near the K first resonance.

this discrepancy, I have made my rotation measurements in the line wings, detuned by at least 1 nm, where I have found this method to reliably match number density measurements using absorption spectroscopy.

Chapter 3

Measurements and Model of Relaxation in Singlet Dimers

In this chapter, I present the details of spin-relaxation due to the electric quad-rupole interaction in alkali $^1\Sigma_g^+$ dimers. I begin by discussing a calculation of the equilibrium dimer density and the molecular potential on which it is based. In section 3.2, I show how the well known form of the quadrupole interaction can be simplified for this application. Next, I discuss dimer formation, breakup and reorientation processes (section 3.3). This leads to an analytic model of spin relaxation, applicable at all cell conditions. The calculation is fairly long, so I have broken it down into a preliminary qualitative analysis (3.4.1), discussion of coherent relaxation (3.4.2), the effect of decohering collisions (3.4.3), and finally the full calculation of relaxation rate in singlet molecules (3.4.4). I then revisit the qualitative behavior and limiting cases in section 3.5.

I present my relaxation rate measurements in section 3.6, and show how these measurements allow determination of chemical exchange and molecular reorientation rates in the vapor, as well as the strength of the quadrupole interaction. Finally, I compare these measured quantities to previous related measurements and classical-trajectory simulations in section 3.7.

3.1 The $^1\Sigma_g^+$ Alkali Dimer Potential

At alkali densities suitable for most applications of a polarized vapor, roughly 0.1–1% of the atoms are in $^1\Sigma_g^+$ dimers. This makes them by far the dominant molecular species. Although the singlet dimer has no net electron spin, the nucleus is subject to depolarization via the electric quadrupole interaction (and, to a lesser extent, via the spin-rotation interaction). Then, after the dimer has been broken up, the electronic and nuclear polarization quickly come into equilibrium through a combination of the atomic hyperfine interaction and spin-exchange collisions (see appendix B). Thus rapid polarization transfer, plus the large density of singlet molecules, make nuclear depolarization an efficient means of spin relaxation, despite the relatively small coupling typical of nuclear interactions.

In order to make quantitative relaxation rate calculations, we need to know how many singlet molecules are present in the vapor. Unfortunately, the dimer density is much more difficult to measure than the atomic density because the dimer ro-vibrational states broaden its resonances into bands. This complicates an absorption measurement, such as that described in section 2.3.1, considerably.

I have therefore chosen to calculate the dimer density from statistical considerations (see, for example, [Reif]). Because this procedure depends sensitively on the molecular potential, I have attempted to construct the most accurate potential possible by starting with the *ab initio* calculations of ref. [Krauss90], scaling them to match recent spectroscopic determinations of the dimer binding energies ([Elbs99, Amiot91, Tsai97]) and matching them to the well studied long range $1/R^6$ potentials of refs. [Marinescu94, Boesten96]. Table 3.1 gives a convenient parameterization of the resulting potentials for K, Rb and Cs, as well as the most recent measurements of binding energy and C_6 coefficients. Figure 3.1 is a plot of the parameterized potentials for comparison to the (scaled) calculations of ref. [Krauss90].

Next, I numerically determined the energy eigenstates of these potentials and summed them, weighted by a Boltzmann factor, to determine the chemical equilibrium coefficient as

$$^1k_{chem} = \frac{1}{8}\left[\frac{h^2}{\pi m k T}\right]^{3/2} \sum_i e^{-E_i/kT}(2\mathrm{J}_i + 1) \tag{3.1}$$

in which m is the atomic mass and E_i, J_i are the energy and rotational angular momen-

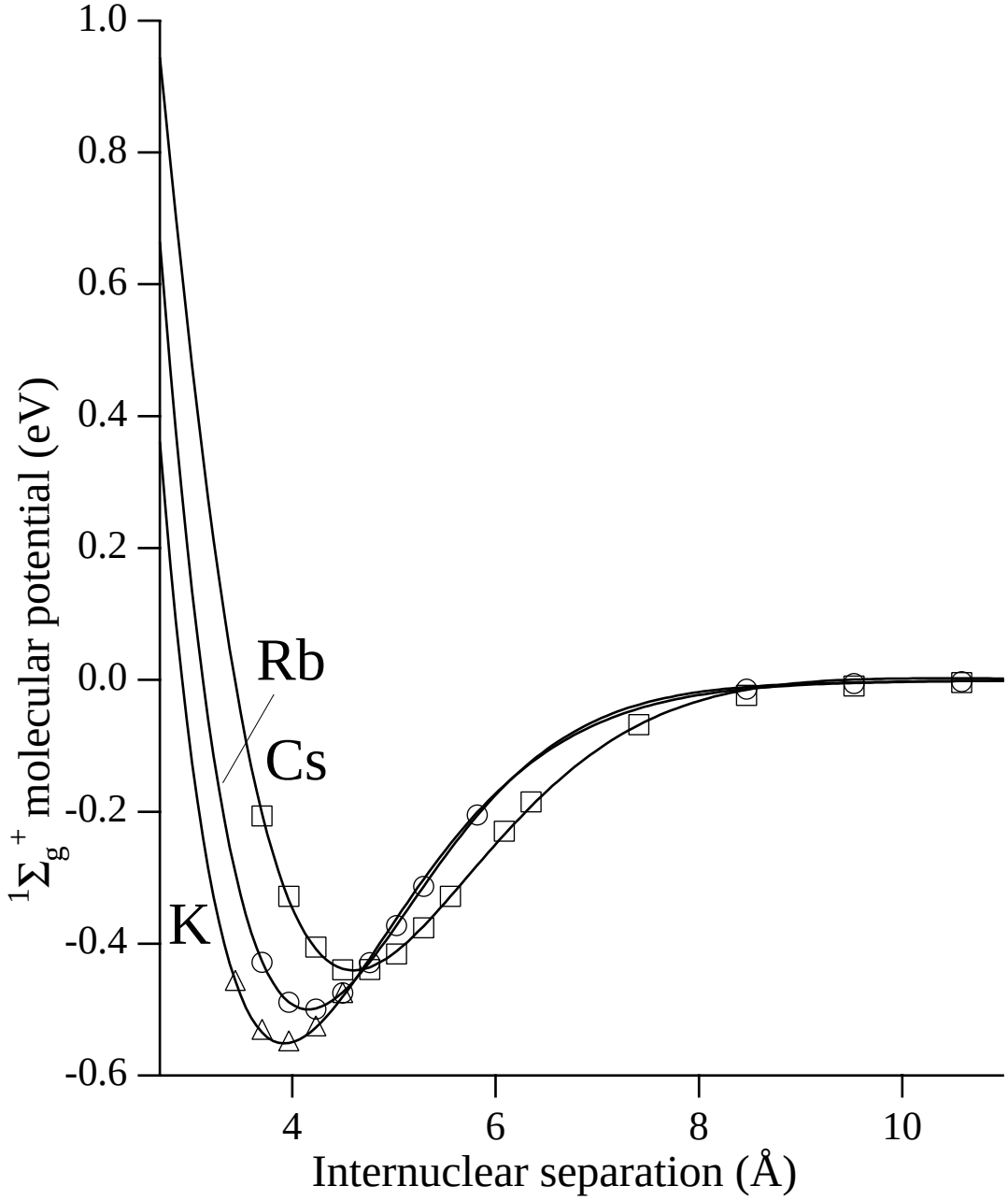

Figure 3.1: Homonuclear diatomic singlet potentials for K, Rb and Cs, scaled to fit the most recent experimental determinations of molecular binding energy. The points plotted are the (scaled) *ab initio* calculations of ref. [Krauss90]. The curves are a convenient analytic fit, parameterized in table 3.1.

	D_E	C_6	c_0	c_1	r_0	r_1	r_2	r_3
K	0.02028	3813	7.7199	-0.14708	1.3579	-0.5126	6.707	2.4974
Rb	0.01820	4550	7.7119	-0.04466	1.3579	4.3540	4.979	2.4974
Cs	0.01630	6330	3.2909	-0.32850	2.2000	-0.8000	7.597	2.9727

Table 3.1: Fit parameters for $^1\Sigma_g^+$ potentials. Column 1 is the most recent experimental determination of the dimer binding energy. The other entries parameterize the potential as $V(r) = c_0 e^{-r/r_0} + c_1 e^{-((r-r_1)/r_2)^2} - C_6(1-e^{-r/r_3})/r^6$. All table entries are in atomic units.

	a_0	a_1	$a_2 \times 10^4$	$a_3 \times 10^7$
K	2.707	-0.1781	2.551	-1.350
Rb	-4.6452	-0.1470	2.003	-1.005
Cs	-7.9145	-0.1426	2.043	-1.081

Table 3.2: Fit parameters for calculated $^1\Sigma_g^+$ dimer chemical equalibrium coefficient to the form $\ln(^1k_{chem}) = \sum a_n \mathrm{T}^n$. a_n are given in the table and T is the vapor temperature in K.

tum of the i'th energy eigenstate. The density of singlet dimers of alkali species A is then

$$[^1A_2] = {}^1k_{chem}[A]^2. \tag{3.2}$$

Table 3.2 gives a parameterized fit to $^1k_{chem}(T)$ for K, Rb and Cs, and Fig. 3.2 shows $^1k_{chem}(T)$ and the calculated fraction of alkali atoms bound in singlet dimers.

3.2 The Quadrupole Interaction in Singlet Molecules

The electric quadrupole interaction in a rotating molecule takes the form (originally due to Casimir and discussed in detail in ref. [Townes], p. 138)

$$V_Q = \frac{1}{2}\frac{eqQ}{I(2I-1)J(2J-1)}[3(\mathbf{I}\cdot\mathbf{J})^2 + \frac{3}{2}(\mathbf{I}\cdot\mathbf{J}) - I^2J^2] \tag{3.3}$$

in which Q is the nuclear electric quadrupole moment and $q = \langle JJ|\partial^2 V/\partial z^2|JJ\rangle$ is the electric field gradient at the nucleus in the stretched rotational state. A somewhat smaller coupling is also present, known as the spin-rotation interaction ([Huber80,

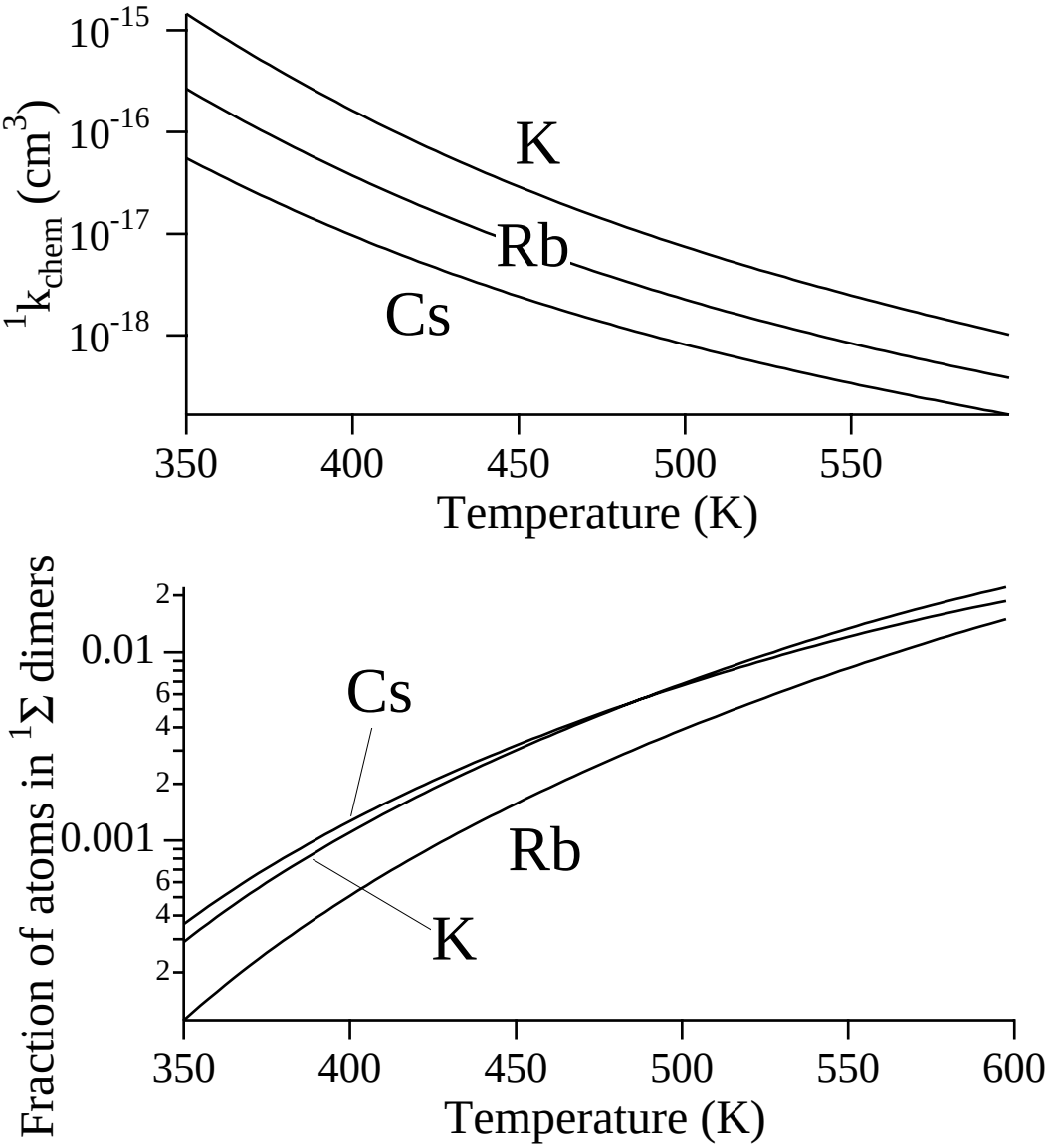

Figure 3.2: Alkali $^1\Sigma_g^+$ dimer chemical equilibrium coefficient (top) and fraction of alkali atoms contained in $^1\Sigma_g^+$ dimers (bottom) as a function of vapor temperature.

VanEsbroeck85])

$$V_{SR} = c'(\mathbf{I} \cdot \mathbf{J}) \tag{3.4}$$

Although measurements of the spin-rotation interaction are not complete, its contribution to relaxation is expected to be much smaller than that of the quadrupole interaction in all alkali dimers (with the possible exception of Cs_2)[Huber80], so I do not include it in the following calculations. In situations in which the spin-rotation interaction is large, it can be treated analytically in a manner completely analagous to the following treatment of the quadrupole interaction.

Under conditions appropriate for SEOP, the average rotational angular momentum J is, on average, greater than 100 $\hbar$. The first term of V_Q is therefore dominant, allowing eq. 3.3 to be simplified to

$$V_Q \approx \hbar\Omega_Q \, \mathbf{I} \cdot \left(\frac{3\hat{\mathbf{J}}\hat{\mathbf{J}} - 1}{2} \right) \cdot \mathbf{I} \tag{3.5}$$

where

$$\Omega_Q = -\frac{eqQ/\hbar}{4I(2I-1)}. \tag{3.6}$$

This interaction couples the nuclear spin to molecular rotation, from which it is lost in subsequent collisions. It is important to point out that the electric field gradient q may depend sensitively on the ro-vibrational state of the molecule. The appropriate value of q to use in eq. 3.6 is the root mean square over the thermal distribution of molecular states. Some consequences of this averaging are discussed in section 3.6.

3.3 Singlet Molecules in a Buffer Gas

Of course, evolution according to eq. 3.5 does not proceed unimpeded. Singlet molecules are formed and dissociated and, on a much shorter time scale, reoriented by collisions with the buffer gas. Since the quadrupole interaction depends on the direction of molecular angular momentum $\mathbf{J}$, such reorienting collisions also halt coherent evolution.

3.3.1 Dimer Formation and Dissociation

Since the singlet dimer binding energy is much larger than $k_B T$, only a rare combination of buffer gas impacts transfers sufficient energy to cause dissociation. Three-body breakup and formation is therefore greatly suppressed, and previous work ([Glas78]) is consistent with the requirement that each $^1\Sigma_g^+$ molecule undergo approximately $\exp(0.5\text{eV/kT}) \approx 10^4$ collisions before dissociating.

Therefore, despite the relative infrequency of $A - {}^1\!A_2$ collisions for alkali species A, they dominate the formation and breakup of singlet dimers through chemical exchange processes of the form

$$A_1 + {}^1(A_2A_3) \;\rightarrow\; {}^1\!(A_1A_2) + A_3 \tag{3.7}$$

under conditions where the alkali density exceeds approximately 10^{-5} of the buffer gas density. There is no Boltzmann suppression of the chemical exchange process because it does not need to overcome the large singlet binding energy. Note that the terms 'formation' and 'breakup' may be somewhat misleading, since the number of dimers is not changed by process (3.7). More precisely (but awkwardly), we might say that chemical exchange is the dominant process by which atoms enter into and exit from singlet molecules.

In order to completely describe molecular dynamics of singlet dimers in a buffer gas, we need to include three-body formation and breakup, chemical exchange, and **J**-reorienting collisions. However, because the cross-section for reorientation is so much larger than for three-body breakup, relaxation during a molecular lifetime is very small whenever the buffer gas pressure is high enough that three-body breakup is significant. In this regime, the atom is cycled through many singlet dimers before relaxing completely, so the relaxation rate depends only on the fraction of time spent in singlet dimers, not the rate or mechanism of formation and breakup (see section 3.4). Therefore, we can simplify our treatment by ignoring three-body processes entirely. The resulting model is valid at all buffer gas pressures and alkali density $>10^{11}\text{cm}^{-3}$.

To characterize the exchange process (3.7), I define the chemical exchange cross-section as follows; the rate at which a given member of a ${}^1\!A_2$ dimer is ejected by chemical exchange is $1/\tau_{ex} = [A]\langle\sigma_{ex} v_{A\cdot A_2}\rangle/2$. The factor of $1/2$ represents the fact that either atom may be ejected.

3.3.2 Molecular Reorientation

Similarly, I define the molecular reorientation cross-section as follows; the rate at which the quadrupole interaction in a singlet molecule is subject to decoherence from collisions with buffer gas species B is $1/\tau_J = [B]\langle\sigma_J v_{B\cdot A_2}\rangle$. Because of the large values of J typical of singlet molecules, this collision-induced decoherence can be thought as the reorietation of the classical dyadic $(3\hat{\mathbf{J}}\hat{\mathbf{J}}-1)/2$ in eq. 3.5. Thus, in terms of the classical vector $\hat{\mathbf{J}}$, I define τ_J as

$$\langle\frac{3\left(\hat{\mathbf{J}}(t)\cdot\hat{\mathbf{J}}(t+\tau_J)\right)^2-1}{2}\rangle = 1/e. \tag{3.8}$$

Of course the magnitude of $\mathbf{J}$ is changed as well, but since the quadrupole interaction is nearly independent of rotational quantum number, this is of no consequence.

3.4 Calculation of Relaxation Rates

3.4.1 Brief Qualitative Discussion

Because of its importance for interpreting NMR experiments, quadrupolar relaxation has been well studied. In particular, many useful results are derived in ref. [Abragam] and we can make a few preliminary predictions based on that work.

At sufficiently high pressure, relaxation is hindered by rapid reorientations of the molecular angular momentum during collisions with the buffer gas. This case is addressed in ref. [Abragam], p. 314, although the derivation assumes that the reorientation is so rapid that even the molecular rotation is hindered, which is not true for singlet molecules in a buffer gas. Thus, the result must be modified to include rotational averaging, but that simply reduces the effective interaction strength by a factor of 2 (see section 6.2). The high pressure relaxation rate is therefore well known: nuclei in a singlet molecule relax at the rate

$$\frac{3}{10}\frac{2I+3}{I^2(2I-1)}\left(\frac{eqQ}{\hbar}\right)^2\tau_J. \tag{3.9}$$

Note that the relaxation rate becomes inversely proportional to buffer gas pressure at

sufficiently high pressure.

We can also predict the low pressure limit because, regardless of the details of the relaxation in a dimer, it must saturate given sufficient interaction time. Thus, we expect the relaxation rate to be proportional to dimer formation rate at low pressure. Since the dominant formation mechanism is pressure independent (section 3.3.1), we expect the relaxation rate to become presure independent as well.

Relaxation in singlet dimers is an unusual example of quadrupolar relaxation because by changing the buffer gas pressure, we can observe the transition from high to low pressure behavior. In the rest of this section, I develop a model that predicts relaxation rates at all pressures.

3.4.2 Density Matrix Evolution

The first task a full calulation of the relaxation rate from singlet dimers is to investigate the evolution of the nuclear density matrix under the influence of eq. 3.5. Specifically, we need to know the average fractional polarization loss (which I will refer to as F_J) during a period of coherent evolution.

Coherent evolution is interrupted by molecular reorientation and chemical exchange, which are both random collisional events, so we expect the duration of coherent evolution τ to be Poisson distributed as

$$P(\tau) = \frac{1}{\tau_c} e^{-\tau/\tau_c} \tag{3.10}$$

in which $1/\tau_c = 1/\tau_J + 1/\tau_{ex}$. The density matrix after a period of coherent evolution should therefore be averaged over period durations and a uniform distribution of molecular orientations $\hat{\mathbf{J}}$ as

$$\rho_F = Eu \int_0^\infty \frac{d\tau}{\tau_c} e^{-\tau/\tau_c} e^{-iV_Q\tau} \rho_0 e^{iV_Q\tau}. \tag{3.11}$$

V_Q is as in eq. 3.5 and Eu denotes an average over Euler angles for $\hat{\mathbf{J}}$. I assume that evolution begins with an axially symmetric density matrix with a spin temperature distribution

$$\rho_{0mn} = T_m \delta_{mn}. \tag{3.12}$$

T_m is the probability to be in nuclear sublevel m. In spin temperature (see ref. [Anderson60] and Appendix B),

$$T_m = \frac{(1-\alpha)\alpha^{I-m}}{1-\alpha^{2I+1}} \qquad \text{where } \alpha = \frac{1-2\langle S_z\rangle}{1+2\langle S_z\rangle} = e^{-\beta} \tag{3.13}$$

$1/\beta$ is the spin-temperature. In the low polarization limit,

$$T_m = (1 + m\langle S_z\rangle)/(2I+1). \tag{3.14}$$

The derivation thus far is independent of the form of the interaction and may be solved in general by diagonalizing the interaction numerically as described in appendix C. However, it is clear that the transformation that diagonalizes the eq. 3.5 is the rotation to the primed system $\hat{\mathbf{z}}' = \hat{\mathbf{J}}$. The density matrix in that system is

$$\rho_{0m'n'} = \sum_n T_n \langle m'|n\rangle\langle n|n'\rangle \tag{3.15}$$

Note that this transformation does not diagonalize the interaction Hamiltonian appropriate for evolution in a magnetic field. In that case, we need to resort to the numerical solution.

We may further simplify eq. 3.5 by rescaling the energy to eliminate the second term $(\hbar\Omega_Q I(I+1)/2)$ and use this form to solve eq. 3.11

$$\begin{aligned} \rho_{Fm'n'} &= Eu\int_0^\infty \frac{d\tau}{\tau_c} e^{-\tau/\tau_c}\rho_{0m'n'} cos(\omega_{m'n'}\tau) \\ &= Eu\frac{\rho_{0m'n'}}{(1+\omega_{m'n'}^2\tau_c^2)} \end{aligned} \tag{3.16}$$

where

$$\omega_{m'n'} = \frac{3}{2}\Omega_Q(m'^2 - n'^2) \tag{3.17}$$

Now, transforming back to the unprimed system,

$$\rho_{Fmm} = Eu\sum_{m'n'n} \frac{T_n}{1+\omega_{m'n'}^2\tau_c^2}\langle m|m'\rangle\langle m'|n\rangle\langle n|n'\rangle\langle n'|m\rangle \tag{3.18}$$

The bra-ket inner products can be written in terms of Wigner D functions, and reduced

by the Clebsch-Gordan series to make the angular integration possible. In the following, the implicit arguments to $D^I_{m_1 m_2}$ are the Euler angles for the rotation $\hat{\mathbf{z}} \rightarrow \hat{\mathbf{J}}$.

$$\begin{aligned}
\rho_{Fmm} &= \sum_{m'n'n} \frac{T_n}{1+\omega^2_{m'n'}\tau_c^2} Eu\left(D^I_{mm'} D^{I*}_{nm'} D^I_{nn'} D^{I*}_{mn'}\right) \\
&= \sum_{m'n'nj} \frac{(-)^{2I-j}}{2j+1} \frac{T_n}{1+\omega^2_{m'n'}\tau_c^2} C^2(IIj;mn) C^2(IIj;m'n') \\
&= \sum_j \frac{(-)^{2I-j}}{2j+1} \sum_n T_n C^2(IIj,mn) \sum_{m'n'} \frac{1}{1+\omega^2_{m'n'}\tau_c^2} C^2(IIj,m'n')
\end{aligned}$$

In the low polarization limit, ρ_{Fmm} - 1/(2I+1) remains proportional to m, thus assuring a spin temperature distribution for the start of the next period of coherent evolution. Thus,

$$\begin{aligned}
F_J(\tau_J,\tau_{ex}) &= 1 - \frac{\sum_m m\rho_{Fmm}}{\sum_m m\rho_{omm}} \\
&= N(\alpha) \sum_{j=0}^{2I} \frac{(-)^{2I-j}}{2j+1} \left(\sum_{m,n=-I}^{I} m\alpha^{-n} C^2(IIj;mn) \right) \times \\
&\qquad \left(\sum_{m,n=-I}^{I} C^2(IIj;mn) \frac{\omega^2_{mn}\tau_c^2}{1+\omega^2_{mn}\tau_c^2} \right)
\end{aligned} \tag{3.19}$$

where the normalization

$$N(\alpha) = \frac{(1-\alpha)^2\alpha^I}{I(1-\alpha)(1+\alpha^{2I+1}) + \alpha(\alpha^{2I}-1)}. \tag{3.20}$$

In the low polarization limit, this becomes

$$\begin{aligned}
F_J(\tau_J,\tau_{ex}) = \frac{1}{6} \sum_{j=0}^{2I} (-)^{2I-j} \left(\frac{3j(j+1)}{I(I+1)(2I+1)} - 1 \right) \times \\
\sum_{m,n=-I}^{I} C^2(IIj;mn) \frac{\omega^2_{mn}\tau_c^2}{1+\omega^2_{mn}\tau_c^2}.
\end{aligned} \tag{3.21}$$

By summing terms with the same $\omega_{m,n}$, we can show that F_J is a Lorentzian function

for nuclear spin $I \leq 3/2$, or a sum of Lorentzians for higher spin.

$$F_J(\tau_J, \tau_{ex}) = \sum_{l=1} c_l \frac{(3l\Omega_Q \tau_c)^2}{1 + (3l\Omega_Q \tau_c)^2} \tag{3.22}$$

where, as before, $1/\tau_c = 1/\tau_J + 1/\tau_{ex}$ and the coefficients c_l are

spin 3/2 (^{39}K,^{87}Rb)	$c_1 = 2/5$
spin 5/2 (^{85}Rb)	$c_1 = 32/105$, $c_2 = 4/21$
spin 7/2 (^{133}Cs)	$c_1 = 5/21$, $c_2 = 4/21$, $c_3 = 1/9$

There is a similarly simple and exact expansion for all I.

Note that for short coherence times, this reduces to

$$F_J(\tau_c) = \frac{3}{10}(2I-1)(2I+3)\Omega_Q^2 \tau_c^2, \tag{3.23}$$

in agreement with ref. [Abragam].

3.4.3 The Effect of Decoherence

Having calculated F_J, the average fractional polarization loss during a period of coherent evolution, we now need to sum the losses from the multiple periods during a molecular lifetime. If an atom undergoes N coherence periods before exiting a molecule, then the fraction of polarization remaining is $[1-(1-F_J)^N]$. Note that because decoherence events are Poisson distributed, setting a fixed value for N does not change the distribution of coherence period lengths that were used for calculating F_J.

Now, if $P(N)$ is the probability of getting N coherence periods before an leaving the dimer, the average fractional polarization loss F_{mol} for a nucleus during a molecular lifetime is

$$\begin{aligned} F_{mol} &= \sum_{N=1}^{\infty} P(N)[1-(1-F_J)^N] \\ &= 1 - \sum_{N=1}^{\infty} P(N)(1-F_J)^N. \end{aligned} \tag{3.24}$$

To evaluate $P(N)$, we simply integrate over all possible molecular lifetimes and

coherence times while maintaining N coherence periods. Thus one can show that

$$\begin{aligned} P(N) &= \int_0^\infty (dt_{ex}/\tau_{ex})\, e^{-t_{ex}/\tau_{ex}} \int_0^{t_{ex}} (dt_2/\tau_J)\, e^{-t_2/\tau_J} \int_0^{t_{ex}-t_2} (dt_3/\tau_J)\, e^{-t_2/\tau_J} \\ &\quad \ldots \int_0^{t_{ex}-t_2-\ldots-t_{N-1}} (dt_N/\tau_J)\, e^{-t_N/\tau_J} e^{-(t_x-t_2-\ldots-t_N)/\tau_J} \\ &= 1/(\tau_{ex}\tau_J^{N-1}) \int_0^\infty e^{-t_{ex}/\tau} \int_0^{t_{ex}} dt_2 \int_0^{t_{ex}-t_2} dt_3 \ldots \int_0^{t_{ex}-t_2-\ldots-t_{N-1}} dt_N \\ &= 1/(\tau_{ex}\tau_J^{N-1}) \int_0^\infty e^{-t_{ex}/\tau} \int_0^{t_{ex}} dt_2 \int_0^{t_2} dt_3 \ldots \int_0^{t_{N-1}} dt_N \\ &= 1/(\tau_{ex}\tau_J^{N-1}) \int_0^\infty dt_{ex}\, e^{-t_{ex}/\tau}\, \frac{t_{ex}^{(N-1)}}{(N-1)!} \\ &= \frac{\tau_{ex}^{N-1}\tau_J}{(\tau_{ex}+\tau_J)^N} \end{aligned} \tag{3.25}$$

and therefore that

$$F_{mol} = 1 - \frac{\tau_J}{\tau_{ex}} \sum_{N=1}^{\infty} \left[\frac{\tau_{ex}(1-F_J)}{\tau_{ex}+\tau_J} \right]^N = \frac{(1+\langle N\rangle)F_J}{1+\langle N\rangle F_J} \tag{3.26}$$

in which $\langle N\rangle = \tau_{ex}/\tau_J$ is the average number of reorientations before an exchange.

3.4.4 Singlet Molecule Relaxation Rate

Finally, we can use the average fractional polarization loss F_{mol} from the previous section to arrive at the total relaxation rate in singlet molecules of species A

$$\Gamma_{sing} = [{}^1A_2]\langle \sigma_{ex} v_{A\cdot A_2} \rangle\ s\ F_{mol} \tag{3.27}$$

where s is the fraction of atomic polarization stored in the nucleus. For Rb, in which two isotopes are present, the appropriate generalization is

$$\Gamma_{sing} = [{}^1A_2]\langle \sigma_{ex} v_{A\cdot A_2} \rangle \sum_i s_i F_{mol,i} \tag{3.28}$$

	s
K	5/6
^{85}Rb (pure)	35/38
^{87}Rb (pure)	5/6
^{85}Rb (nat.)	0.7778
^{87}Rb (nat.)	0.1296
Cs	21/22

Table 3.3: Fraction of vapor polarization contained in the nucleus (s). This quantity is changed by the presence of other isotopes– the 'pure' values should be used with an isotopically pure sample, and the 'nat.' values for a sample with natural abundances.

where the sum is over isotopes. Note that the factor s is analagous to the nuclear slowing down factor discussed in [Happer72] and can be calculated similarly, yielding

$$s_i = f_i \frac{(I_i + 1/2)\mathrm{ctnh}(\beta(I_i + 1/2)) - 1/2\mathrm{ctnh}(\beta/2)}{1/2(\tanh(\beta/2) - \mathrm{ctnh}(\beta/2)) + \Sigma_j f_j (I_j + 1/2)\mathrm{ctnh}(\beta(I_j + 1/2))} \tag{3.29}$$

in terms of the spin temperature parameter β [Anderson60] and the isotopic fraction f_i of species i. In the low polarization limit,

$$s_i = \frac{f_i((I_i + 1/2)^2 - 1/4)}{1/2 + \Sigma f_j (I_j + 1/2)^2}. \tag{3.30}$$

Table 3.3 gives the appropriate values for K, Rb and Cs in the low polarization limit.

3.5 Qualitative Behavior and Limiting Cases

The calculation above is valid at all buffer gas pressures and alkali densities above $10^{11}\mathrm{cm}^{-3}$. Unfortunately, it does not have a particularly simple form and does not address the effect of a magnetic field on the relaxation rate, except as mentioned in section 3.4.2. It is therefore instructive to look at a few limiting cases and approximations to eq. 3.28. This process also makes it clear how experimental measurements can provide values for the unknown parameters σ_J, σ_{ex} and Ω_Q.

We first consider the qualitative effect of a magnetic field on the relaxation rate. As with other examples of magnetic decoupling (such as the hyperfine interaction), the field must be larger than the interaction to be decoupled in order to have significant effect.

In addition, the presence of reorienting collisions adds the more stringent requirement that the nuclear precession due to the magnetic field must be large ($\sim$1 radian) during a coherence period for decoupling to occur. Otherwise, the (small) precessions due to the field and the quadrupole interaction simply add and do not interfere with one another. Thus, a qualitative prediction for field decoupling is

$$\Gamma_{sing}(B) = \Gamma_{sing(B=0)} \frac{(\omega_B \tau_J)^2}{1 + (\omega_B \tau_J)^2} \qquad \text{with } \omega_B = \frac{g_I \mu_N B}{I\hbar} \tag{3.31}$$

This turns out to be quite a good approximation, although the exact field dependence requires a numerical solution as described in appendix C. Note that the only unknown parameter in eq. 3.31 is τ_J, which makes the field dependence an excellent way to measure the molecular reorientation cross-section. The more exact, numerical solution has this feature as well.

It is also instructive to consider relaxation in the limit of high and low buffer gas pressure. In the high pressure limit ($\tau_J \ll \tau_{ex}, \Omega_Q^2 \tau_J \tau_{ex} \ll 1$)

$$\Gamma_{sing} = \frac{3}{10}(2I-1)(2I+3)\frac{[^1A_2]}{[A]}\, s\, \Omega_Q^2 \tau_J. \tag{3.32}$$

This expression is correct for all magnetic field. The relaxation rate is inversely proportional to buffer gas pressure, varies with alkali density as $^1k_{chem}[A]$ and is independent of the chemical exchange cross-section (justifying the assertion in section 3.3.1 that the high pressure relaxation rate is independent of dimer formation mechanism). Note that eq. 3.32 depends on the interaction strength Ω_Q and reorientation rate. Once the reorientation cross-section has been measured by observing the magnetic field dependence, the high pressure relaxation rate provides a good measurement of Ω_Q.

In the low pressure limit, as long as the alkali vapor pressure is not too large ($\tau_J \rightarrow \infty, \Omega_Q \tau_{ex} \gg 1$), $F_{mol} \rightarrow F_J = \sum c_l$. Therefore,

$$\Gamma_{sing} = [^1A_2]\langle \sigma_{ex} v_{A\cdot A_2} \rangle\ s\ \sum_l c_l \tag{3.33}$$

with c_l as defined in eq. 3.22. In this regime, the relaxation rate becomes independent of buffer gas pressure and depends on alkali density as $^1k_{chem}[A]^2$. Note that the only unknown parameter in eq. 3.33 is σ_{ex}, which makes low pressure studies an excellent

way to measure chemical exchange.

The transition between the high and low pressure regimes occurs when the terms in the denominator of eq. 3.26 are equal– that is, at a characteristic pressure where $\tau_J = \tau_{ex} F_J$. Substituting in for F_J, and noting that $\Omega\tau_J \ll 1$, we see that the transition occurs when

$$9\Omega_Q^2 \tau_{ex} \tau_J \sum_l c_l l^2 = 1 \tag{3.34}$$

which shows that the characteristic pressure is inversely proportional to alkali density. This feature depends on all three unknown parameters, and provides a good consistency check for our model.

3.6 Measurements

Figure 3.3 summarizes my measurements of Rb relaxation in N_2 as a function of magnetic field. The main part of the figure shows a typical field decoupling. The insert shows that the field width varies linearly with buffer gas pressure in agreement with eq. 3.31.

These field dependence measurements are especially revealing because the field width depends only on the reorientation cross-section. I have fit eq. 3.28 to this data, allowing σ_J to vary (and numerically diagonalizing the interaction as described in Appendix C) and find that $\sigma_J = 12(2)\mathring{A}^2$. The measurements summarized in fig. 3.3 were taken at alkali densities between $2.5\times10^{14}\text{cm}^{-3}$ and $3.0\times10^{15}\text{cm}^{-3}$. The field widths show no dependence on alkali density.

Figure 3.4 shows my measurements of Rb relaxation in N_2 near the transition between the high and low pressure regimes described in section 3.5. Note that the qualitative behavior is essentially as described in section 3.5, although instead of approaching a constant at low buffer gas pressure P, the relaxation rate continues to increase at approximately 530 $s^{-1}(\text{Torr}/P)$. I believe that this effect is unrelated to relaxation in singlet dimers, and represents the decay of polarization due to diffusion to the cell walls. This hypothesis explains the experimental fact that the extreme low pressure behavior is approximately independent of alkali density. In addition, if we assume that the additional low pressure relaxation represents the decay of the lowest diffusion mode ([Happer72]) of the cell, the implied diffusion coefficient is for Rb in N_2 is 0.22 cm^2/s

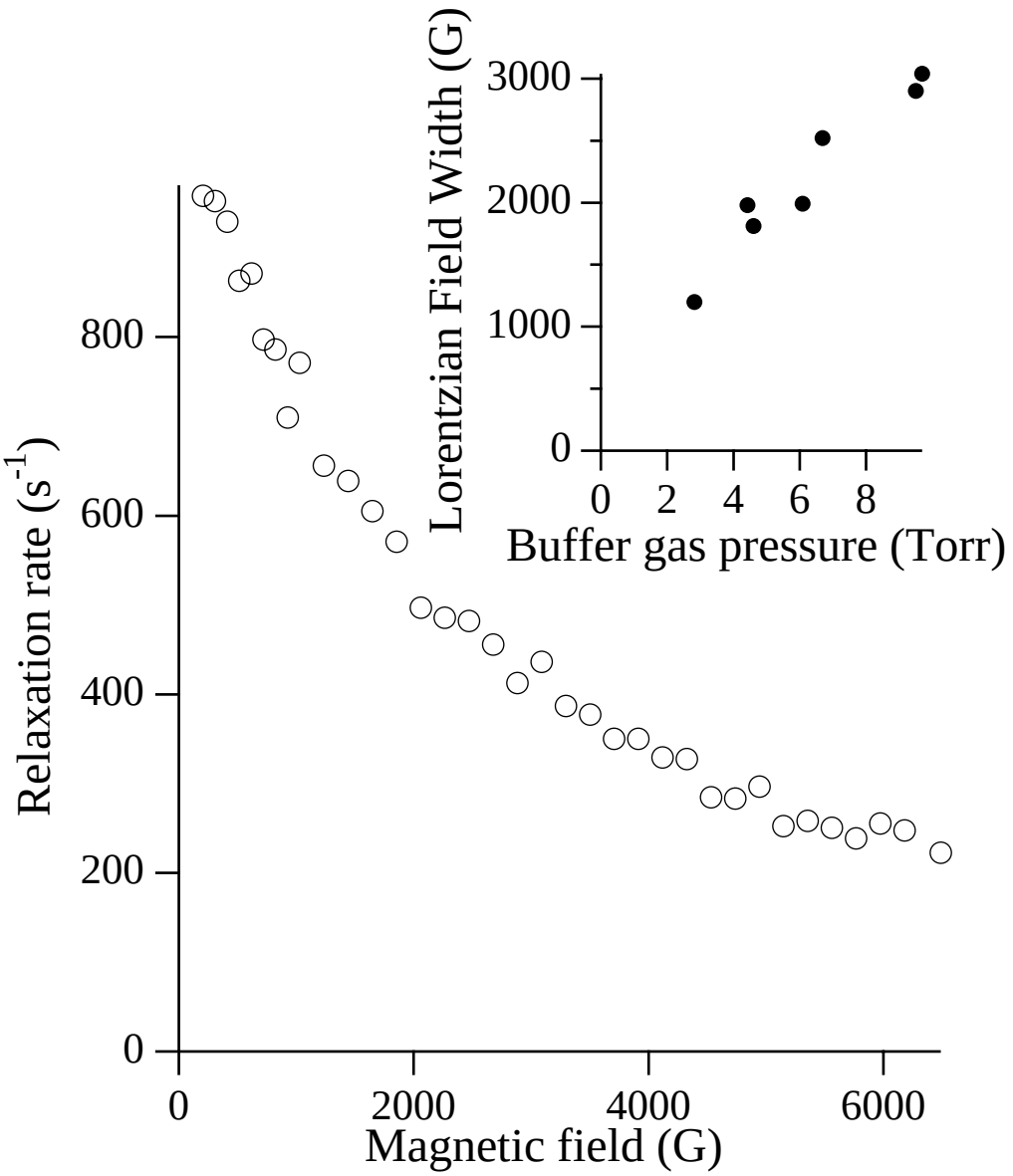

Figure 3.3: Measured Rb relaxation rate as a function of magnetic field at [Rb]=1.45×10^{15}cm^{-3} and N_2 pressure of 6.09 Torr. The insert shows the approximately linear dependence of the field width on buffer gas pressure. This indicates that the duration of coherent relaxation according to eq. 3.5 is cut short by collisions with the buffer gas. Note that because of the two Rb isotopes and the exact form of eq. 3.5, the fit to a Lorentzian function is not exact.

which is in fair agreement with published value of 0.33 cm^2/s (ref. ([McNeal62]).

I therefore fit the measurements in fig. 3.4 to a function of the form $\Gamma = \Gamma_{sing} + a_1 + a_2/P$ with the additional terms representing alkali-alkali relaxation and diffusion. These are the fits shown in fig. 3.4. As described in section 3.5, the combination of low and high pressure behavior constrains both σ_{ex} and Ω_Q and I find the best fit for $\sigma_{ex} = 173(35)\mathring{A}^2$, $\Omega_Q = 80(8)$ kHz for ^{85}Rb and $\Omega_Q = 130(13)$ kHz for ^{87}Rb. Note that since the ratio of the quadrupole moments $Q_{85}/Q_{87} = 2.07$, and the field gradient q is essentially independent of isotope, we know from eq. 3.6 that $\Omega_{85}/\Omega_{87} = 0.62$. The two values are therefore not independent and I maintained this ratio while doing the fit.

Because of the much smaller quadrupole coupling in K and Cs, similar measurements in those alkalis are difficult with my current apparatus and I did not pursue them.

3.7 Previous Measurements

To the best of my knowledge, these are the first direct measurement of relaxation rates due to singlet molecules. However, the electric quadrupole interaction has been studied previously and values for σ_{ex} and σ_J inferred by observing the dependence of NMR linewidths on experimental conditions. The first such experiment, by Gupta, *et al.* ([Gupta74]), quotes approximate values for Cs in Ne that are similar to ours*. Subsequent work on Na ([Huber80, Kompitsas75]), K ([Kamke75], and Cs([Kompitsas75]) gives similar values as well, with the exception of ref. [Huber80], which implies an improbably small σ_J for Rb in Ne. Atom-dimer exchange processes have also been studied using colliding atomic and molecular beams ([Mascord76]), and yield cross-sections similar to our measurements. Finally, I have performed classical-trajectory Monte Carlo modeling of atom-dimer exchange collisions (see appendix D) using the trimer potential of ref. [Martins83] scaled to reflect recent dimer binding energy data (see section 3.1). Because of the large angular momenta typical of these collisions, a semi-classical calculation should be sufficient. The reliability of these results is probably limited by the quality of the trimer Born-Oppenheimer potential. I predict a chemical exchange cross-section of $180\mathring{A}^2$ in K, $193\mathring{A}^2$ in Rb and $210\mathring{A}^2$ in Cs. This work compares favorably to

*Equation (7) in ref. [Gupta74] is too large by a factor of 4 because of its failiure to account for the motional narrowing in a rotating singlet molecule. Thus, the implied value of σ_J in that experiment (eq. 13) should be changed to $\approx 2.5\mathring{A}^2$.

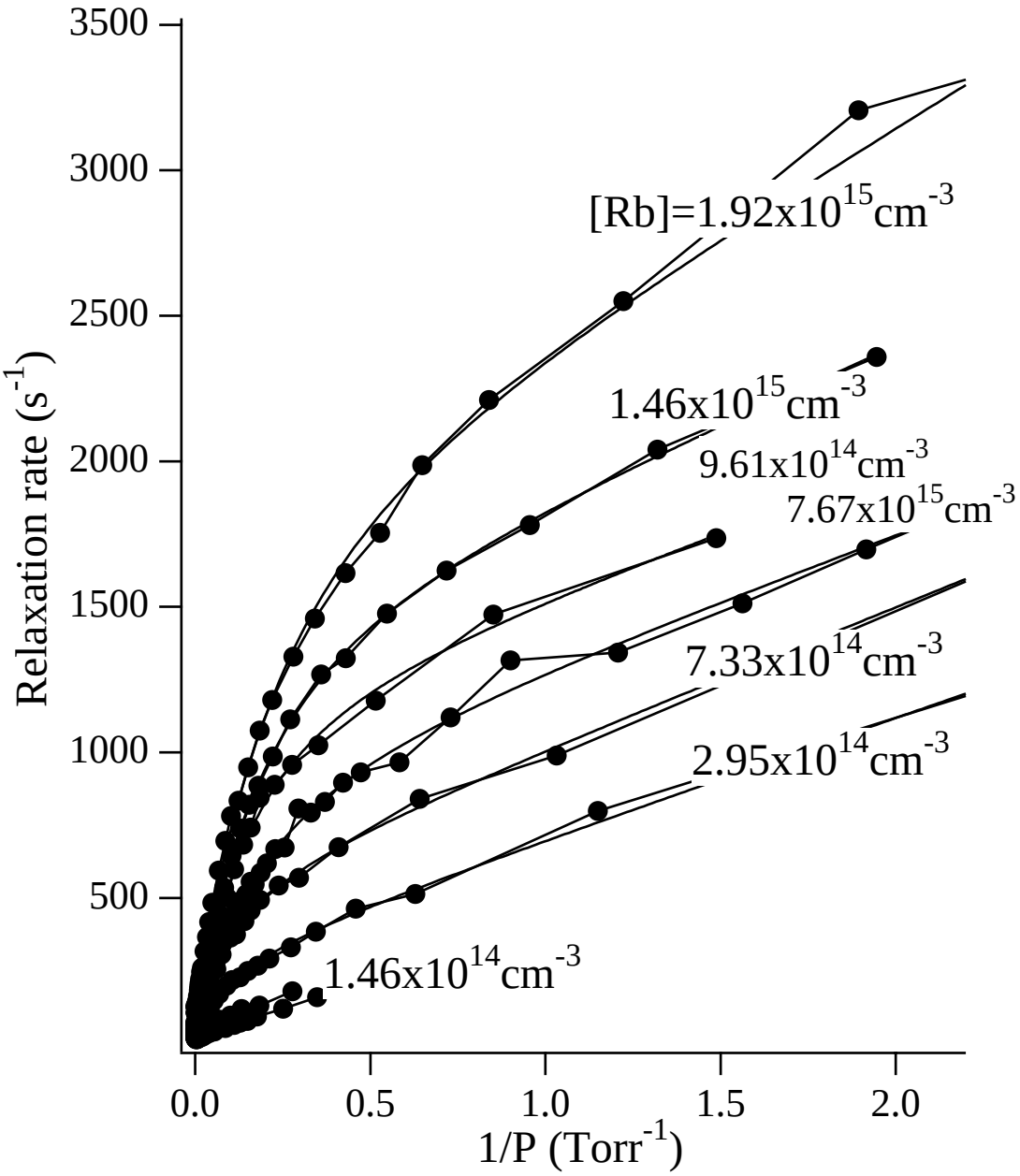

Figure 3.4: Measured relaxation rate as a function of inverse buffer gas pressure $1/P$ and Rb density. This shows how the relaxation rate in singlet dimers transitions from a region of inverse P dependence to P independence at a characteristic pressure of a few Torr. The fits are to eq. 3.5 and constrain σ_{ex} and Ω_Q.

my measurements as well. See ref. [Whitehead75] for a similar calculation.

There has also been one previous measurement of Ω_Q, and here the comparison is not as good. This measurement, made by Logan, et. al. in 1952 ([Logan52]) used molecular beam methods to measure the quadrupole energy splittings directly. Their quoted values (translated using eq. 3.6) are 27.5 kHz for ^{85}Rb and 48.3 kHz for ^{87}Rb.

This discrepancy may be resolved by noting, as has been recognized before (see ref. [Logan52] and references therein), that the interaction strength Ω_Q varies with molecular ro-vibrational state. The Logan result must be interpreted as the statistically most likely value of the interaction strength, whereas the spin-relaxation experiment measures the root mean square value. I also note that due to certain experimental artifacts (discussed in ref. [Logan52]), the Logan results was intended as a lower bound on Ω_Q.

Chapter 4

Measurements of Alkali-Alkali Relaxation

In this chapter, I present my measurements of alkali-alkali and alkali-buffer gas relaxation. This work has led me to reject the previously held belief that alkali-alkali relaxation occurs in binary collisions between alkali atoms. In subsequent chapters, I develop and evaluate alternate theories to explain the experimental phenomena.

I begin by explaining the usefulness of buffer gas pressure series in studying relaxation processes individually. I show how I have used this technique to establish the alkaki density dependence of alkali-alkali relaxation in section 4.2, and the magnetic field dependence in section 4.3. I then discuss the implications of a magnetic field dependence in section 4.4.

4.1 Use of Pressure Series

As I have described in chapters 1 and 3, the four most important relaxation mechanisms in this experiment each depend on buffer gas pressure differently. The clearest way that I have found to separate the mechanisms from each other experimentally is to vary the buffer gas pressure while keeping all other cell conditions constant. This technique yields a series of relaxation rates such as that shown in fig. 4.1.

Note that each of the major relaxation mechanisms contributes a distinct feature to the pressure series. At extreme low pressure, vapor relaxation is dominated by

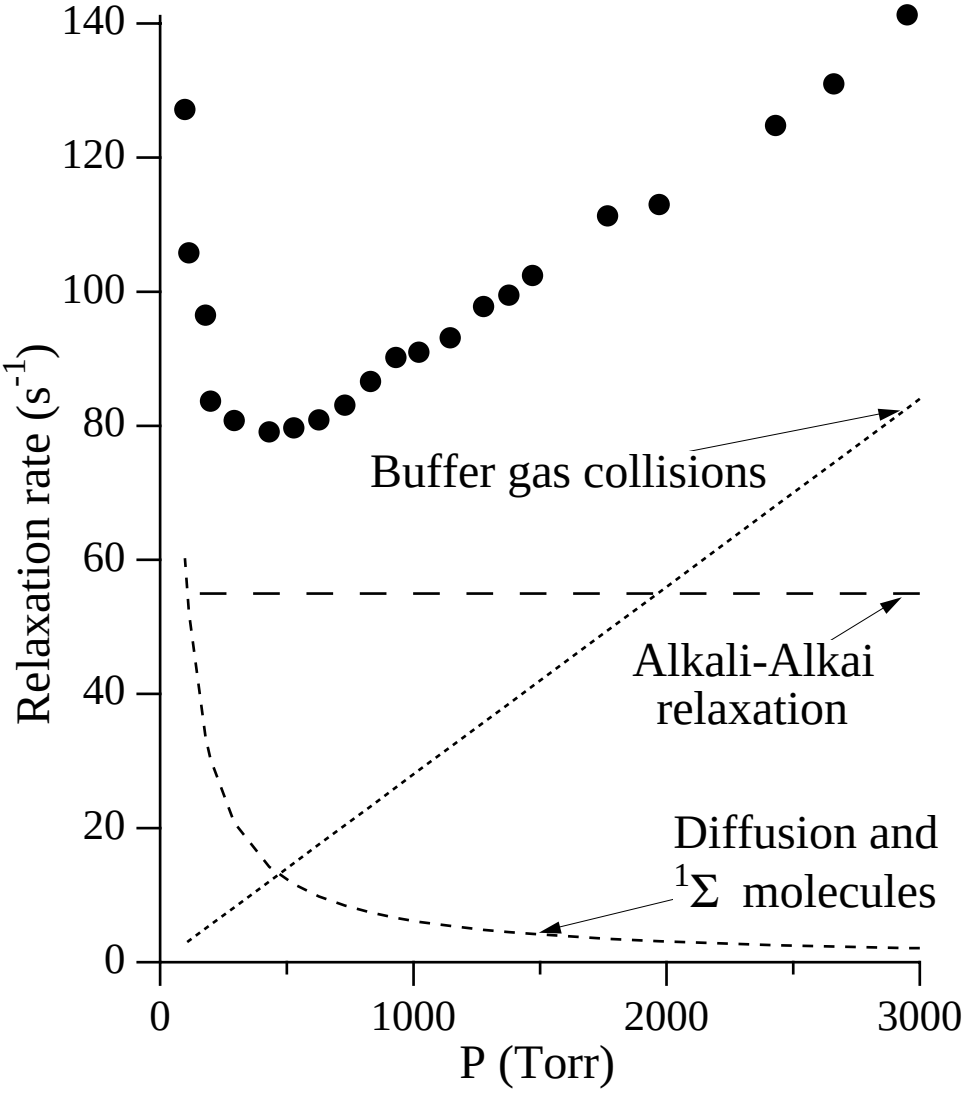

Figure 4.1: A typical pressure series of relaxation rates as a function of buffer gas pressure. This series was taken with [Rb]=1.1×10^{15}cm^{-3} in N_2. Note the characteristic behavior due to singlet dimers at low pressure and buffer gas collisions at high pressure. Alkali-alkali relaxation is an offset that is not accounted for by any other mechanism.

diffusion and, as the pressure increases, one passes through a region dominated by singlet molecules and finally alkali-buffer gas collisions. Alkali-alkali relaxation corresponds to an offset to the curve that is not accounted for by the other three mechanisms. These characteristic pressure dependences are demonstrated in fig. 4.1 as well.

I have therefore found it useful to measure a pressure series before and after changing an experimental parameter. That way, by noting which features have changed, I can find out the individual dependences on that parameter.

4.2 Alkali Density Dependence of Alkali-Alkali Relaxation

I first used this technique to investigate the alkali density dependence of alkali-alkali relaxation. Figure 4.2 shows three pressure series recorded at different alkali densities. Note that both the alkali-alkali and singlet dimer contributions increase quickly with alkali density. The investigation of relaxation in singlet dimers (chapter 3, eq. 3.28) makes it possible to subtract off the low pressure contributions, leaving only alkali-alkali and alkali-buffer gas relaxation. The residuals then fit well to a line whose slope is a measure of the alkali-buffer gas relaxation cross section, and whose intercept is the alkali-alkali relaxation rate. Figure 4.2 demonstrates this process, and figure 4.3 shows how the slopes and intercepts vary with Rb density. Note that alkali-alkali relaxation varies approximately linearly with alkali density. This is consistent with the assumption that it arises from an alkali-alkali interaction. The alkali-buffer gas relaxation cross-section also increases with Rb density, although only very slowly. A similar (but larger) increase has been noted before, for Rb in He ([Baranga98]).

Table 1.1 gives my measured values for alkali-buffer gas relaxation cross-sections. As described in the next section, alkali-alkali relaxtion is more complicated and can not be described by a single cross-section.

4.3 Magnetic Field Dependence of Alkali-Alkali Relaxation

4.3.1 Observation

While I was measuring coherence times in singlet dimer relaxation, I noticed that the magnetic decoupling characteristic of low pressure relaxation (see chapter 3) does not

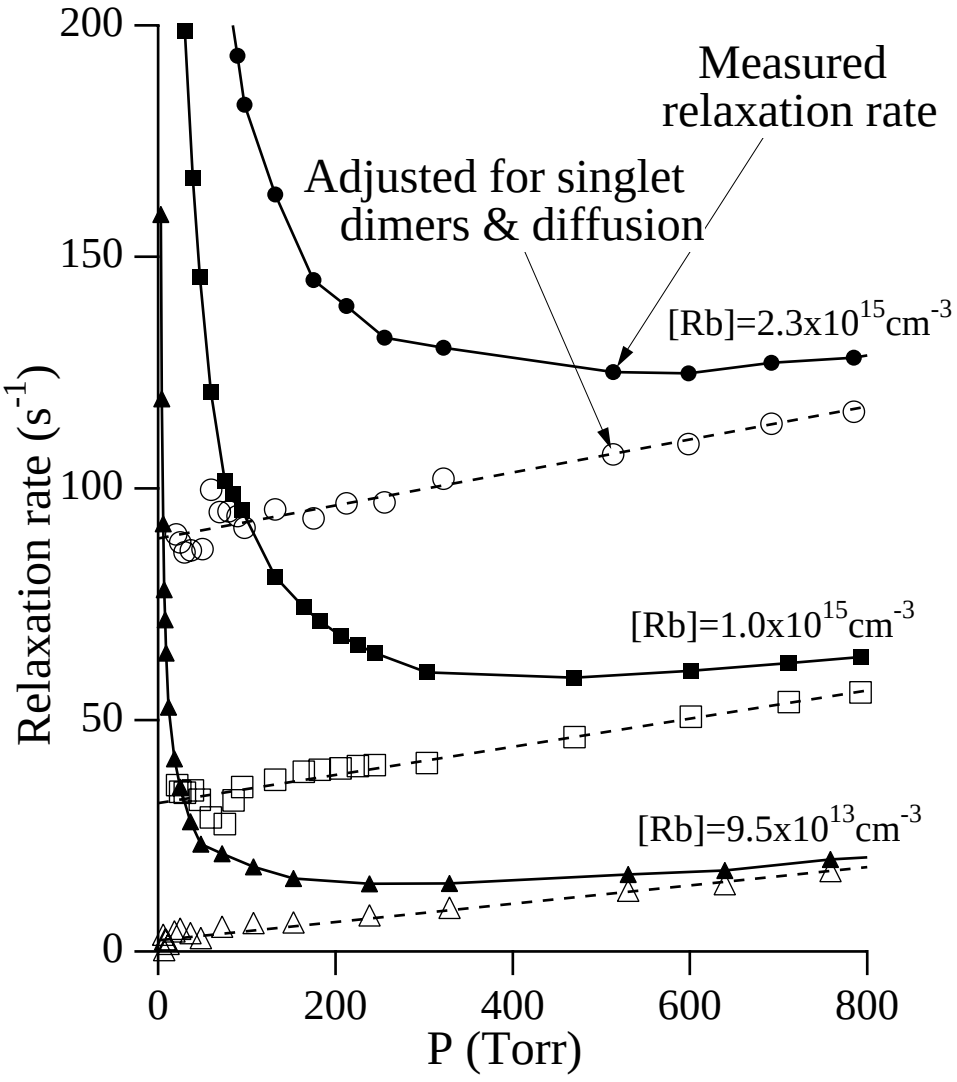

Figure 4.2: An example showing how low pressure relaxation due to singlet dimers and diffusion may be subtracted off using the results of chapter 3. The residuals then have a constant slope, which gives the alkali-buffer gas relaxation cross-section, and an offset, which is alkali-alkali relaxation. Note that the offset increases rapidly with alkali density while the slope does not. These data were taken with N_2 as the buffer gas.

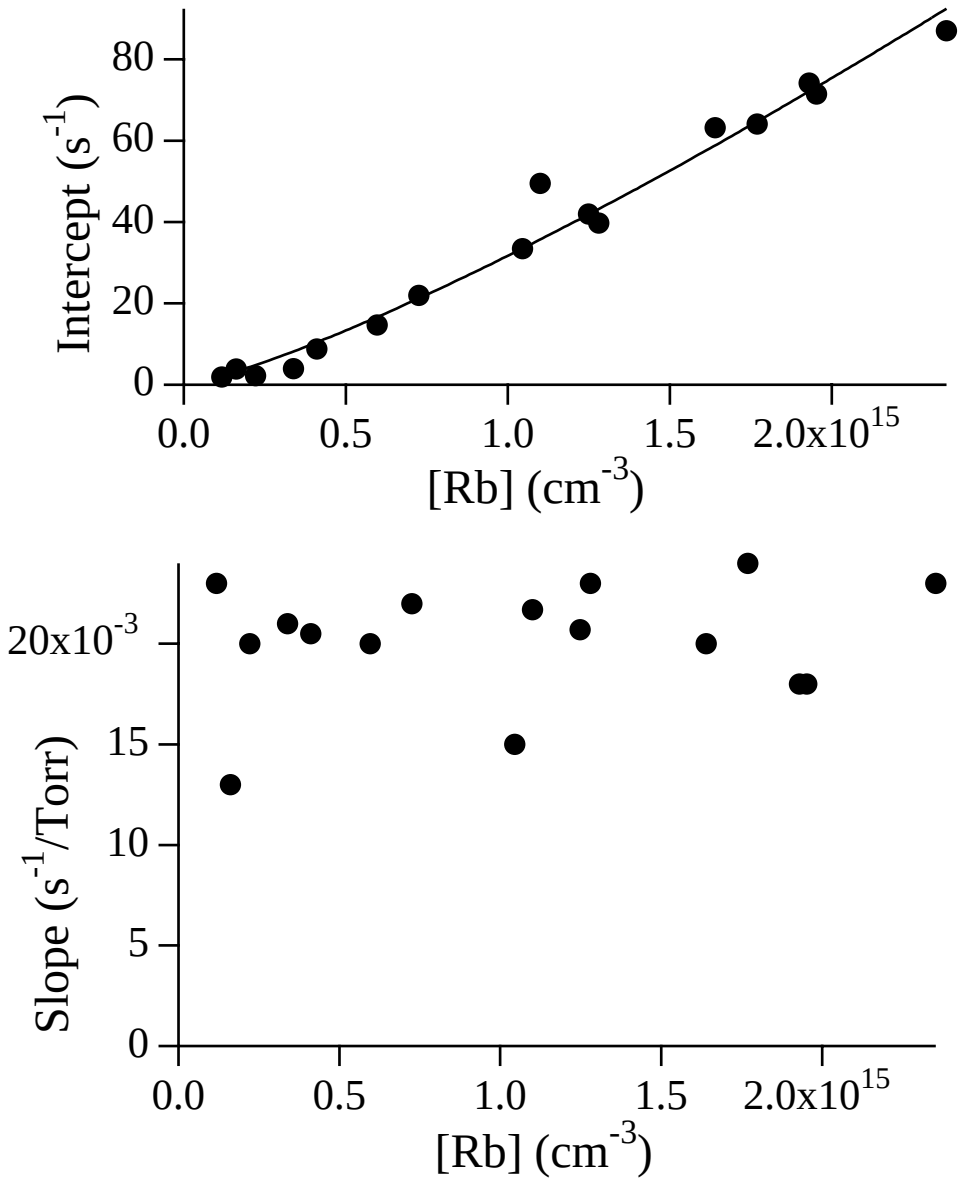

Figure 4.3: Measured residual slopes and intercepts after low pressure relaxation is subtracted off in the manner of fig. 4.3. The slopes give the alkali-buffer gas relaxation cross-section and the intercepts show the alkali density dependence of alkali-alkali relaxation.

entirely disappear at higher pressures. In fact, it persists at pressures of many atmospheres, even though the predicted relaxation rate in singlet molecules becomes negligible. Thus, either alkali-alkali or alkai-buffer gas relaxation must be sensitive to a magnetic field as well.

In order to learn which relaxation mechanism was being decoupled, and to guard against experimental artifacts, I used the pressure series technique described in section 4.1. Two such series are shown in fig. 4.4, which clearly demonstrate that over a large range in buffer gas pressure, only the alkali-alkali relaxation is affected by application of a magnetic field.

Note, however, that some alkali-alkali contribution is still required to fit the 6 kG series in fig. 4.4. This indicates that 6 kG is sufficient to decouple most, but not all, of the alkali-alkali relaxation. I have verified that further increasing the field to 1.2 Tesla does not significantly change the relaxation rate. I therefore conclude that alkali-alkali relaxation has two components, only one of which is decoupled by a relatively small magnetic field. These components may or may not be explained by the same mechanism, but any consistent theory must account for this partial decoupling.

Finally, I observed how the relaxation rate depends on magnetic field while keeping alkali density and buffer gas pressure constant. One such example is shown in fig. 4.5. I find that the decoupling is always well represented by a Lorentzian function.

The experimental observations thus far have led me to parameterize alkali-alkali relaxation of alkali species A as

$$\Gamma_{alk}([A]) = \left(\kappa_A + \frac{\kappa_B}{1 + (B/B_D)^2}\right)[A]. \tag{4.1}$$

Having used pressure series to establish that only alkali-alkali relaxation is affected by changes in alkali density and magnetic field, it is now much more straightforward to study this phenomenon using field dependences like fig. 4.5 as follows; first, measure relaxation rate as a function of magnetic field at many different buffer gas pressures while holding alkali density constant. This allows direct measurement of κ_B and B_D, and highlights any pressure dependence of either parameter. Next, measure relaxation rate as a function of magnetic field at many alkali densities while holding buffer gas pressure constant. This allows measurement κ_A, κ_B and B_D, highlights any alkali density dependence of the parameters.

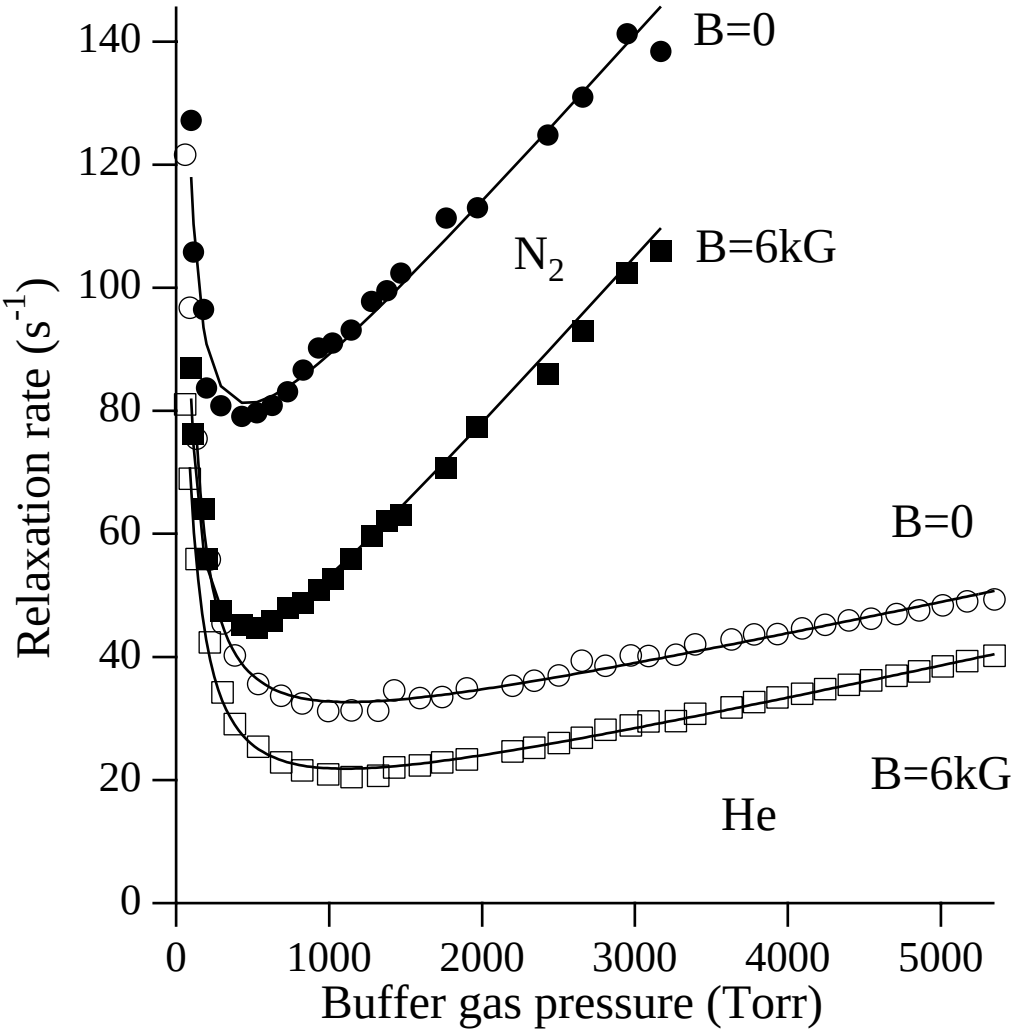

Figure 4.4: Rb relaxation rates as a function of buffer gas pressure in low (circles) and high (squares) magnetic field. Rb densities were 1.1×10^{15}cm^{-3} (filled) and 6.5×10^{14}cm^{-3} (unfilled). Note that in both cases, the application of a magnetic field reduces relaxation rates by a pressure independent amount. This indicates that alkali-alkali relaxation is decoupled by the field. The field decoupling is independent of buffer gas used, as demonstrated in fig. 4.12.

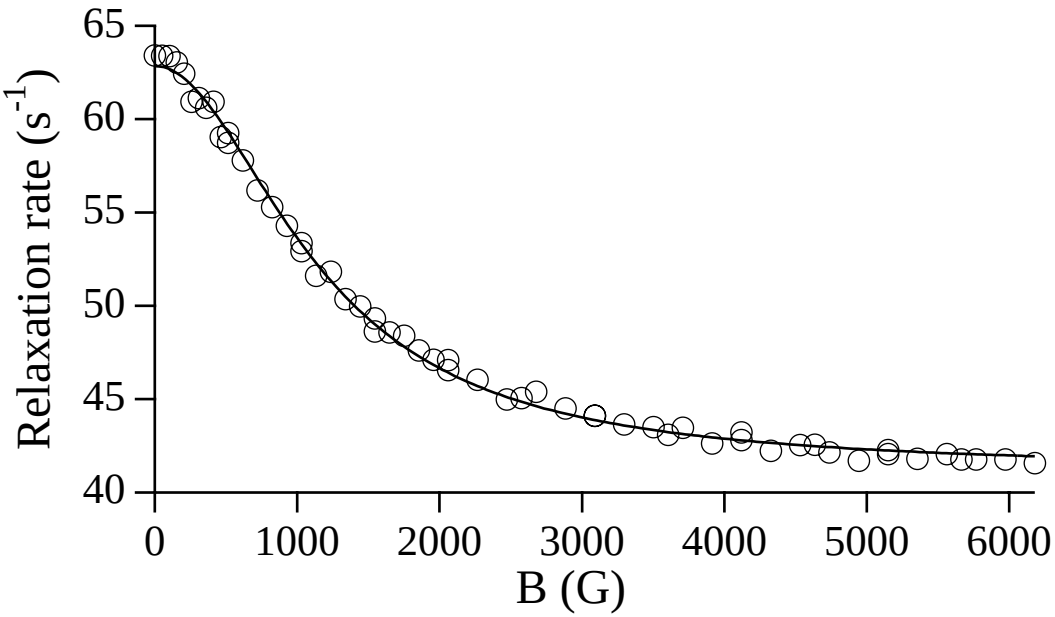

Figure 4.5: A typical series showing decoupling of alkali-alkali relaxation in a magnetic field. This series was taken with [Rb]=6.8×10^{14}cm^{-3} in N_2.

I have shown three examples of this process, with K in N_2 given in fig. 4.6, Rb in He in fig. 4.7, and Cs in He in fig. 4.8. Note that the Cs was contained in a sealed glass cell, so I did not vary the buffer gas pressure.

The data can be summarized by the following qualitative observations: observations:

1 Over a range of pressures from 20 Torr to 20000 Torr and alkali densities from 2×10^{13} to 5×10^{15}cm^{-3}, I saw no cases in which the form of eq. 4.1 did not accurately fit the data.

2 κ_A and κ_B are independent of buffer gas species and are pressure independent over at least two orders of magnitude. Some lessening of κ_B may occur at extremely high pressure, although the interpretation of this data is complicated by departure from spin temperature equilibrium (see fig. 4.6, appendix B).

3 κ_B has a weak, positive alkali density (or temperature) dependence. That is, the field dependent alkali-alkali relaxation rate increases with alkali density slightly faster than linear. I find that the field dependent relaxation rate in K and Rb are well represented by $\kappa_B[A]([A]/10^{15}\text{cm}^{-3})^{1/4}$. κ_B in Cs

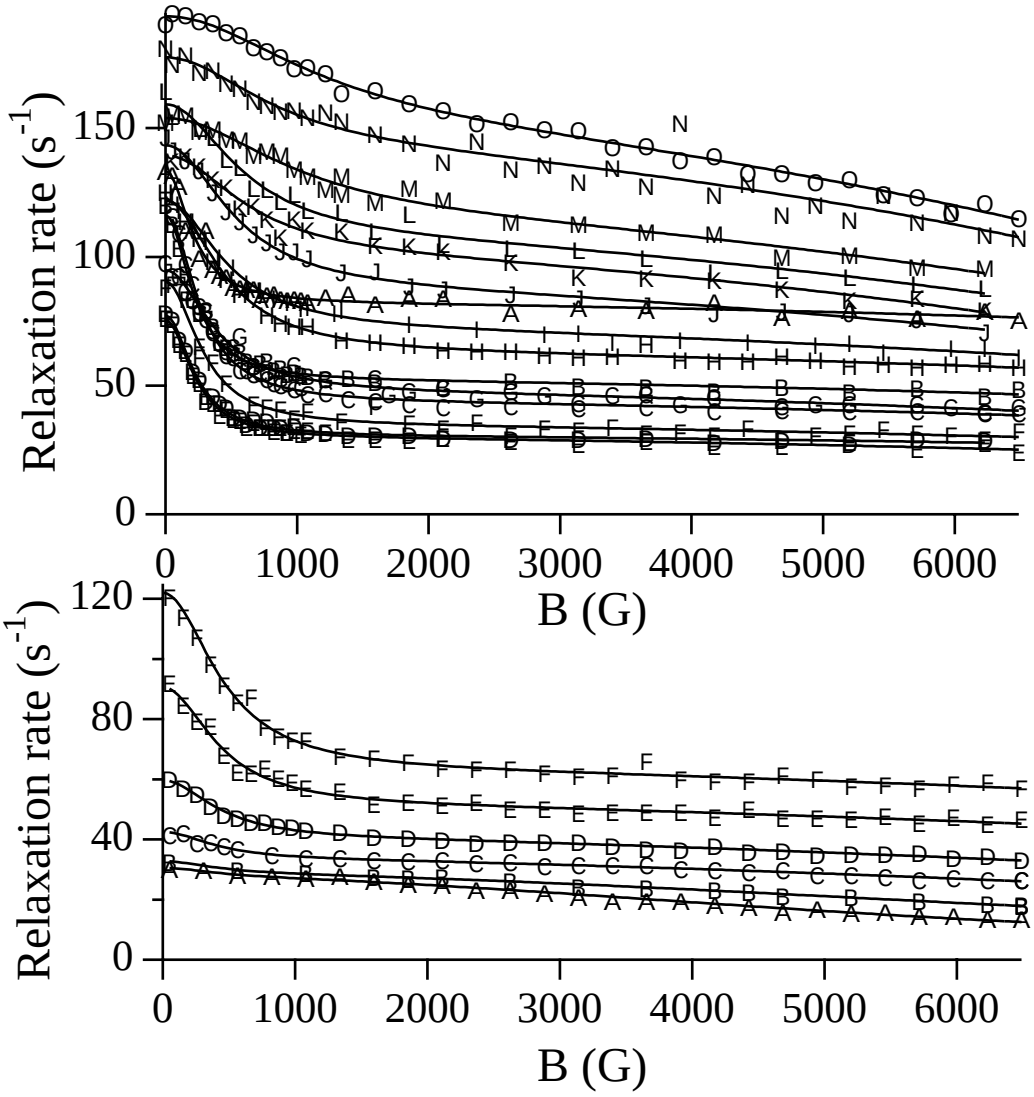

Figure 4.6: Magnetic field dependence of K relaxation as N_2 pressure (top) and [K] (bottom) are changed. In the top figure, [K] is held at 4.5×10^{15}cm^{-3} and pressures (A-O) are 21.5, 47, 72, 148, 330, 611, 1030, 1322, 1853, 2367, 3182, 3439, 4225, 5074, 5737 Torr. In the bottom figure, the pressure is held at 1300 Torr and the [K] (A-F) are 0.30, 0.45, 1.1, 1.9, 3.6 and 4.8×10^{15}cm^{-3}. Note that these measurements are complicated by a departure from spin-temperature equilibrium at high pressure. This causes a quadratic decrease in apparent relaxation rate, even though the relaxation mechanism is not affected by the field. See appendix B for an explanation of this effect.

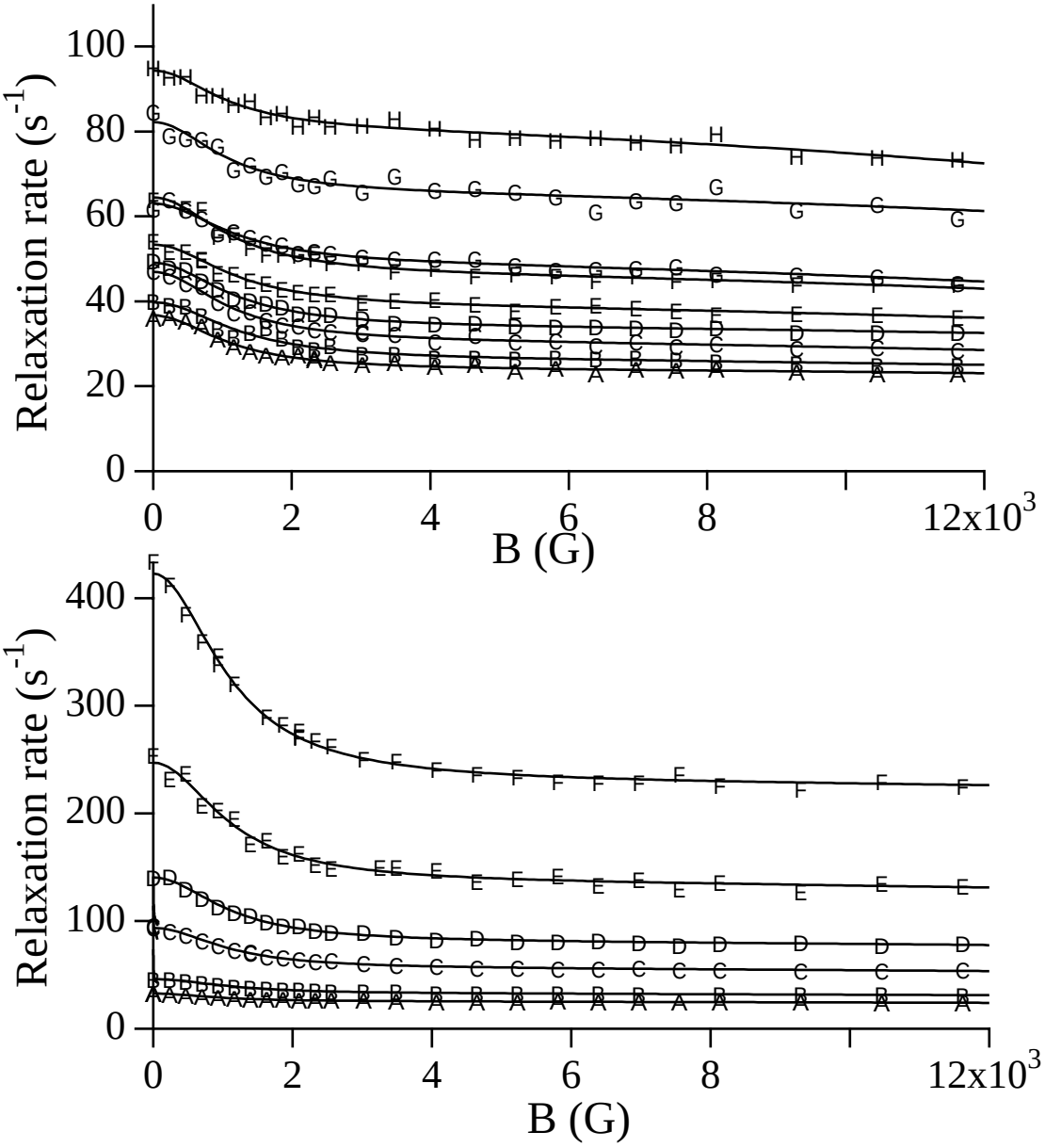

Figure 4.7: Magnetic field dependence of Rb relaxation as He pressure (top) and [Rb] (bottom) are changed. In the top figure, [Rb] is held at 7.4×10^{14}cm^{-3} and pressures (A-H) are 2270, 3747, 5297, 6824, 8349, 9850, 11390, 12900 and 16040 Torr. In the bottom figure, the pressure is held at 4750 Torr and the [Rb] (A-F) are 0.47, 0.71, 1.5, 2.1, 3.4 and 5.0×10^{15}cm^{-3}.

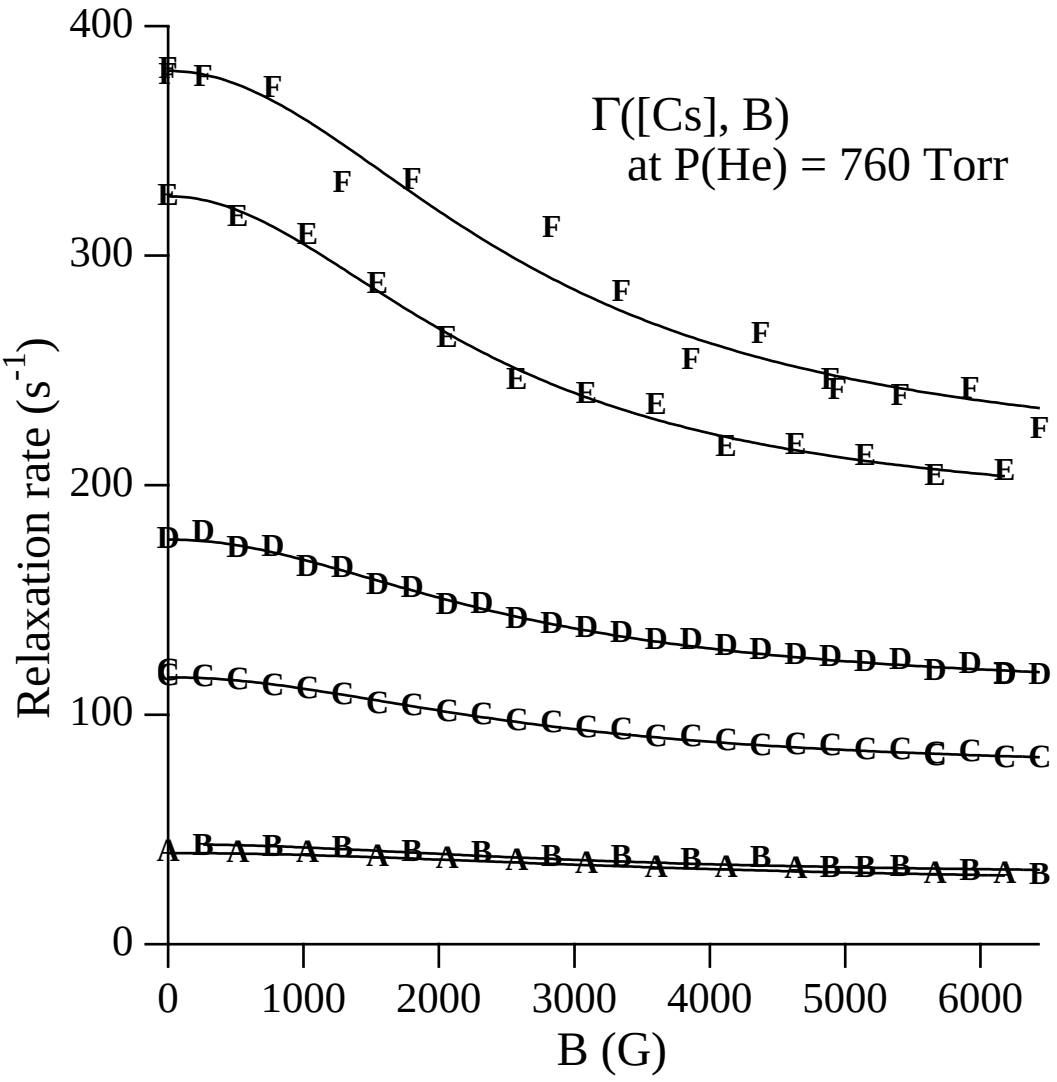

Figure 4.8: Magnetic field dependence of Cs relaxation as [Cs] is changed. [Cs] (A-F) are 0.20, 0.21, 1.7, 2.9, 6.8 and $7.8\times10^{14}\mathrm{cm}^{-3}$.

appears to have a smaller alkali density dependence and is sufficiently well represented by a single value.

4 B_D is buffer gas species and pressure independent over two orders of magnitude in Rb, although slight broadening appears to occur at extremely high buffer gas pressure. Much more significant broadening occurs for K at high pressure, especially for K in N_2. This indicates that the interaction causing relaxation is subject to decoherence through collisions with the buffer gas. I represent this effect with the approximate pressure dependence

$$B_D = B_{D,0}\sqrt{1 + (P/P_D)^2} \tag{4.2}$$

as introduced in eq. 1.3. I saw no dependence of B_D on alkali density.

5 κ_A, κ_B and B_D are all smallest in K, larger in Rb and largest in Cs

6 In all three alkalis, B_D at low buffer gas pressure is fairly close to the field required to decouple the hyperfine interaction ($B_D \approx \Delta E_{hyp}/g_S\mu_B$, where ΔE_{hyp} is the ground state hyperfine splitting.

These observations are shown quantitatively in figs. 4.9, 4.10, 4.11 and 4.12. Figure 4.9 shows the Lorentzian field widths as a function of buffer gas pressure, and demonstrates the broadening noted above. Figure 4.10 shows how the high field relaxation rate increases with alkali density, which is a measure of κ_A. Note, however, that a small part of the increase is likely due to temperature dependence of the alkali-buffer gas relaxation, so the implied value of κ_A is an upper bound. Figure 4.11 shows how the field decoupling increases with alkali density, which is a measure of κ_B. Finally, fig. 4.12 shows that κ_B is remarkably independent of buffer gas pressure, despite clear indications in fig. 4.9 that the interaction is subject to decoherence through collisions with the buffer gas.

My measured values for κ_A, κ_B, $B_{D,0}$ and P_D appear in table 1.2.

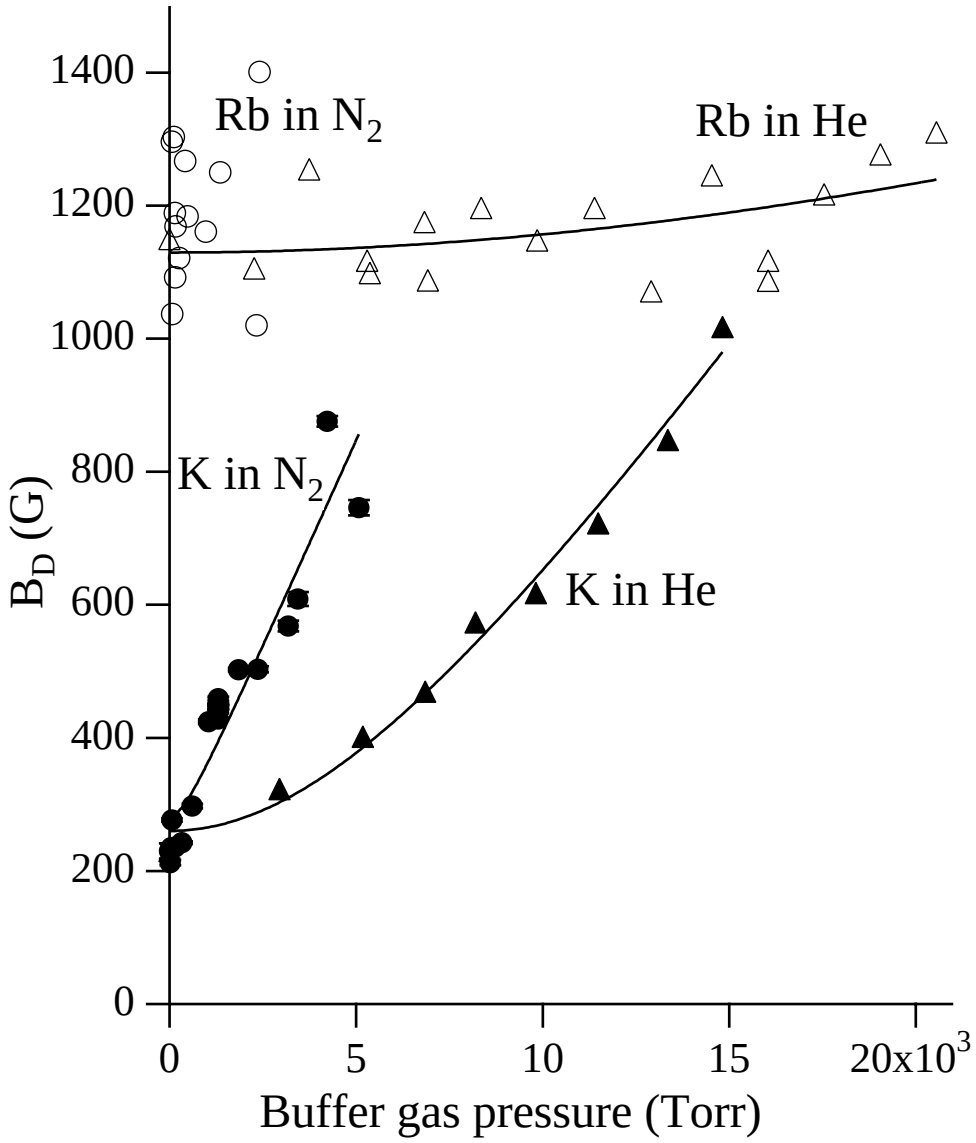

Figure 4.9: Magnetic field decoupling widths (B_D) as a function of buffer gas pressure. Measured widths are shown for K (filled) and Rb (unfilled) in He (triangles) and N_2 (circles).

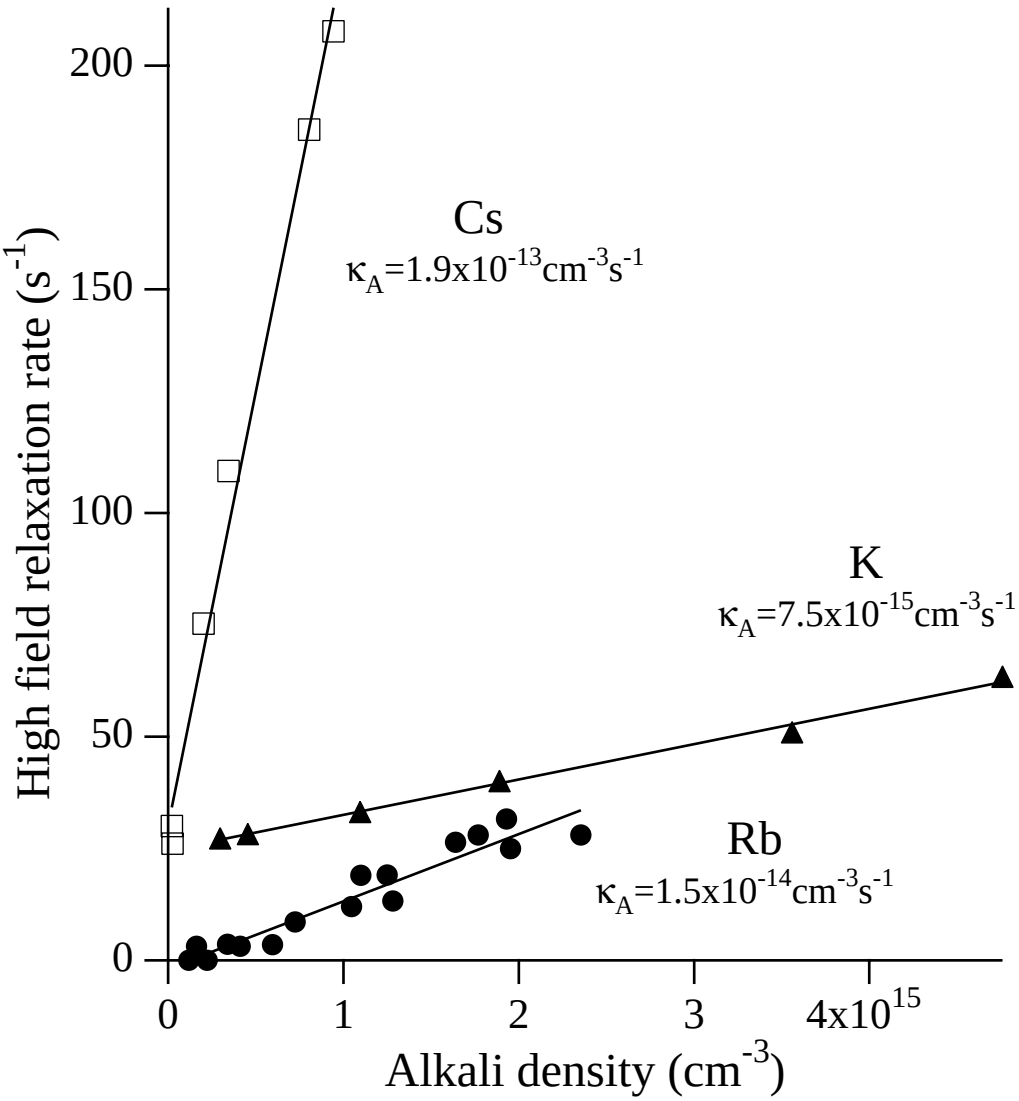

Figure 4.10: High field relaxation rates as a function of alkali density. The K data were taken with N_2 pressure of 1300 Torr. The Cs data were taken with He pressure of 760 Torr. The Rb data are from fits to high field pressure series like that shown in fig. 4.4. Note that the K and Cs numbers should be considered an upper bound because some of the increase with alkali density may be due to a temperature dependence of the alkali-buffer gas relaxation cross-section.

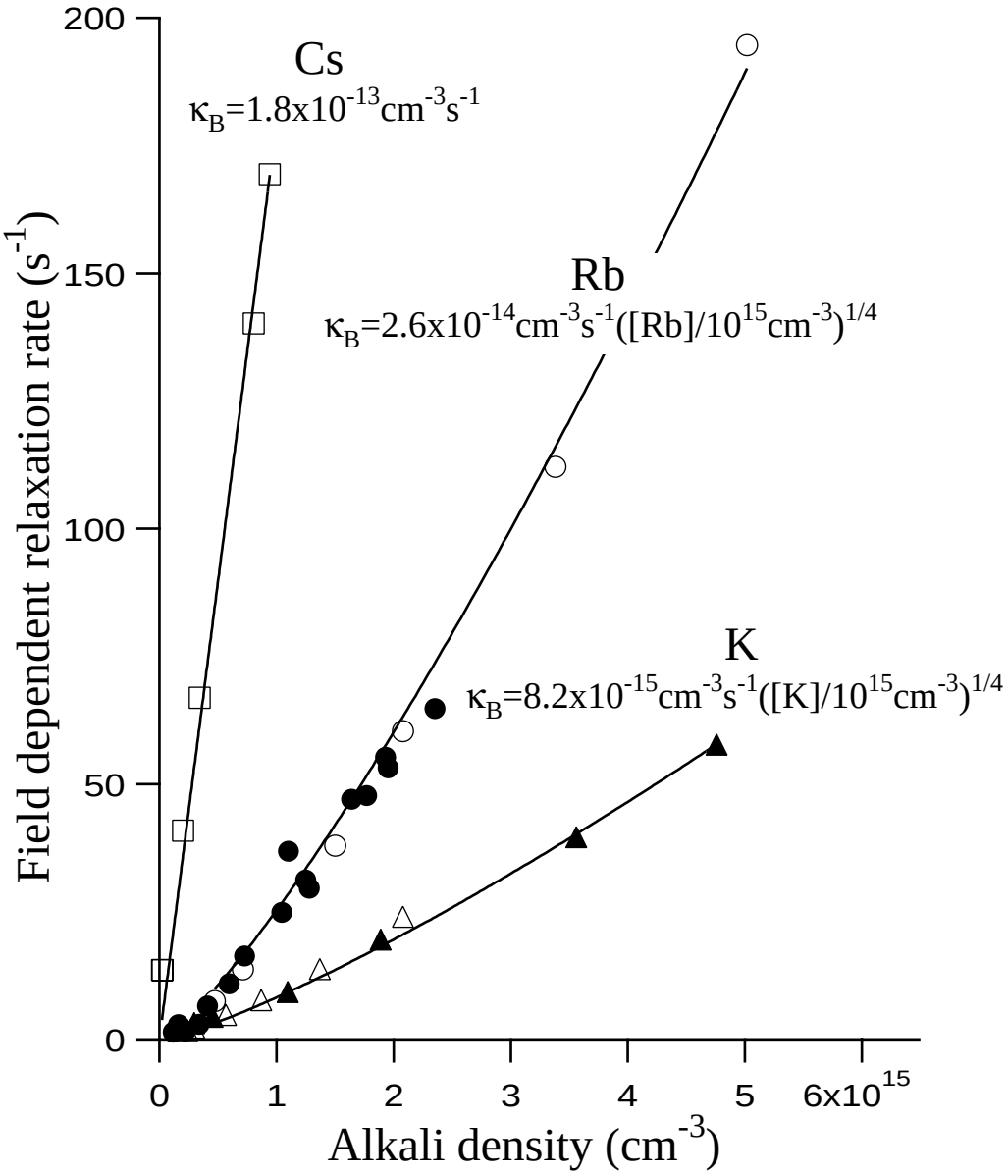

Figure 4.11: Field-dependent part of alkali-alkali relaxation $\kappa_B[A]$ in K (triangles), Rb (circles) and Cs (squares) with He (unfilled) or N_2 (filled) as the buffer gas. Note that κ_B is independent of buffer gas species. I find that in K and Rb, κ_B increases slightly with alkali density (or temperature). I have represented that increase by using the fits shown in the figure.

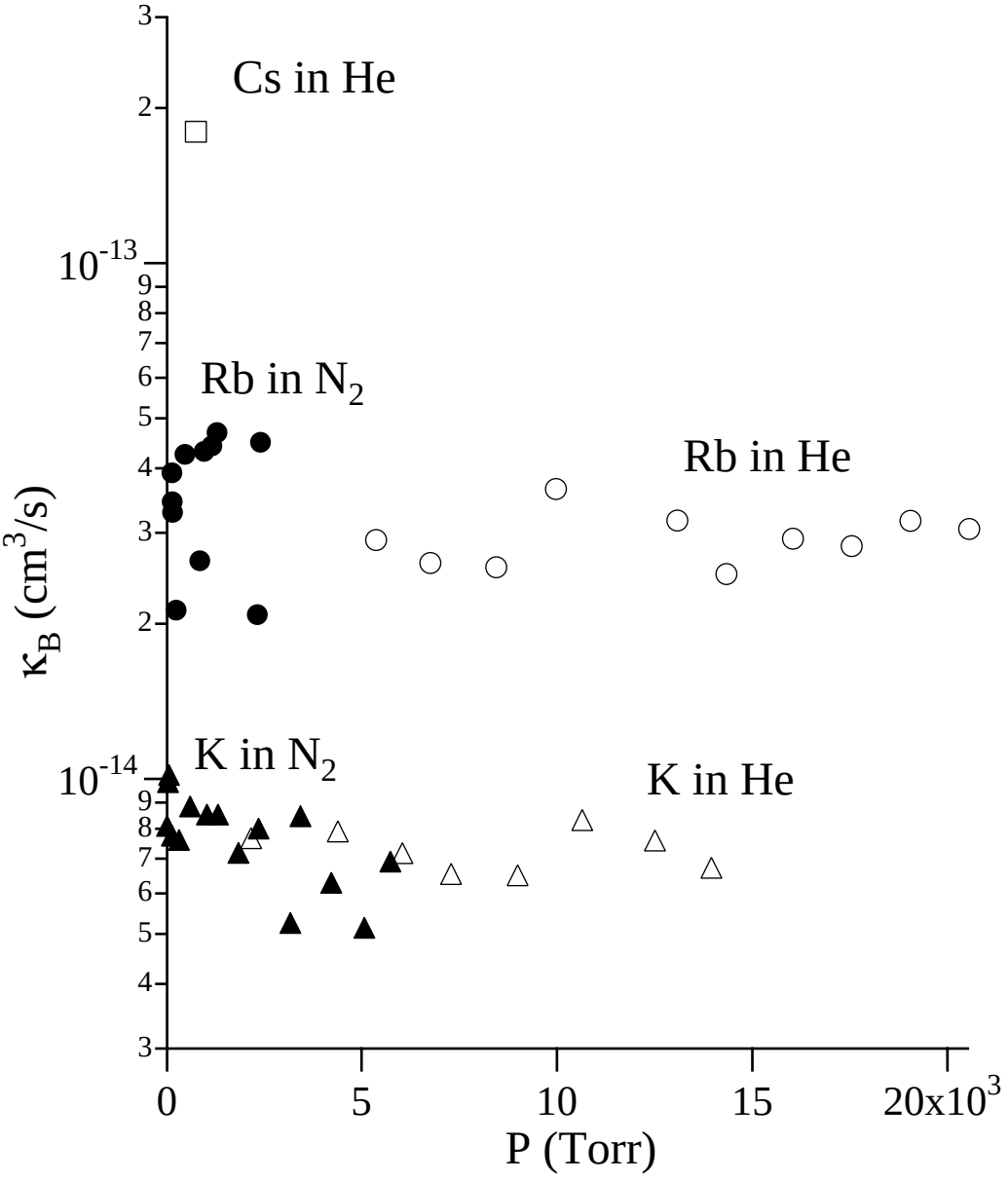

Figure 4.12: Measured dependence of κ_B on buffer gas pressure. The values shown are the field-induced reduction in relaxation rate divided by $[A]([A]/10^{15})^{1/4}$, as per fig. 4.11. Alkali densities used were 4.5×10^{15}cm^{-3} (K in N_2), 1.3×10^{15}cm^{-3} (K in He), 1.5×10^{15}cm^{-3} (Rb in N_2), and 7.3×10^{14}cm^{-3} (Rb in He). Note that κ_B shows no consistent dependence on buffer gas pressure.

4.4 Implications

In the analysis of relaxation in singlet dimers, I explained how measuring magnetic field decoupling of quadrupole tells us how long the relaxing interaction acts coherently (section 3.5). The same argument applies to alkali-alkali relaxation, regardless of the underlying mechanism.

Of course, the relaxation mechanism can (and probably does) act on the alkali electron, so if we measure that a field of B_D is required to decouple alkali-alkali relaxation, a lower bound on the coherence time τ_C for the relaxing interaction is

$$\tau_C > 1/g_S\mu_B B_D. \tag{4.3}$$

If the relaxation occurs through an interaction with the nuclear spin, the required coherence time would be much longer.

Thus, the interaction causing alkali-alkali relaxation must last at least 300 ps in K, 50 ps in Rb and 18 ps in Cs. These times are much longer than a typical atomic collision at the temperature in the cell and therefore leads me to reject the previously held belief ([Knize89, Wagshul94]) that alkali-alkali relaxation arises during a binary alkali collision. This argument is expanded and made more quantitative in chapters 5 and 6.

Chapter 5

Model of Relaxation in Alkali-Alkali Collisions

In this chapter, I discuss the expected relaxation rate due to binary alkali-alkali collisions. I will show that it is too small to match the experimentally observed alkali-alkali relaxation rate and lacks the observed magnetic field dependence. I begin with a parameterization of the of potential between two alkali atoms in the triplet state. This is followed in section 5.2 by a discussion of the spin-dipolar and second order spin-orbit couplings, which are thought to be the largest interactions that can cause spin-relaxation in binary collisions. I then outline a classical trajectory calculation of relaxation rates in section 5.3 and compare its predictions to experiment section 5.4. Note that this calculation does not include quantum effects such as the tunneling and Feshbach resonances. I discuss those corrections and show them to be negligible in chapter 6.

5.1 The $^3\Sigma_u^+$ Alkali Dimer Potential

As two alkali atoms approach each other, the coupling between the valence electron spins through the exchange interaction becomes larger than the individual atomic hyperfine couplings at a distance of about 25 a_0. At distances closer than that, it is convenient to consider the electronic states as coupled in the singlet or triplet manifold. The largest spin-relaxing interaction does not mix the two manifolds, so any collisions that cause relaxation must be take place along the triplet potential.

	D_E	C_6	c_0	c_1	r_0	r_1	r_2	r_3
K	0.0195	2.4293	3813	-0.03173	1.5877	-3.3752	8.656	3.7
Rb	0.0184	2.9074	4550	-0.02321	1.5812	-2.6054	8.478	3.7
Cs	0.0162	1.7451	6330	-0.01271	1.9893	5.3418	6.042	3.7

Table 5.1: Fit parameters for the $^3\Sigma_u^+$ potentials. Column 1 the dimer binding energy. The other entries parameterize the potential as $V(r) = c_0 e^{-r/r_0} + c_1 e^{-((r-r_1)/r_2)^2} - C_6(1 - e^{-r/r_3})/r^6$. All table entries are in atomic units.

As is the case for the singlet dimers, Krauss and Stevens (ref. [Krauss90]) have performed *ab inito* calculations of the $^3\Sigma_u^+$ Born- Oppenheimer potentials. As of this writing, there are no experimental measurements of these potentials comparable to those of the singlet dimers, so I have used their calculations unmodified. Figure 5.1 shows the calculated triplet potentials for K, Rb and Cs along with a convenient fit, which is parameterized in Table 5.1.

5.2 The Spin-Dipolar and Second Order Spin-Orbit Interactions

5.2.1 Spin-Dipolar Coupling

As shown in chapter 4, the alkali-alkali relaxation rate is nearly proportional to alkali density. Therefore, the most obvious candidate mechanism involves the interaction of one alkali atom with another. As always, angular momentum is conserved in such an interaction, and the only place spin polarization can go is into the rotation of the two atoms around each other. All other possible couplings are either completely negligible (such as coupling to the radiation field), or do not constitute spin relaxation because the polarization is eventually recoupled to an alkali electron (such as the hyperfine and exchange interactions).

One possible relaxation mechanism is the classical interaction of the valence electrons as magnetic dipoles when the atoms approach each other. I will refer to this as the spin-dipolar coupling, and it takes the form

$$V_{SD} = \frac{(g_S \mu_B)^2}{r_{12}^3} \mathbf{S_1} \cdot (3\hat{\mathbf{r}}_{\mathbf{12}}\hat{\mathbf{r}}_{\mathbf{12}} - 1) \cdot \mathbf{S_2} \tag{5.1}$$

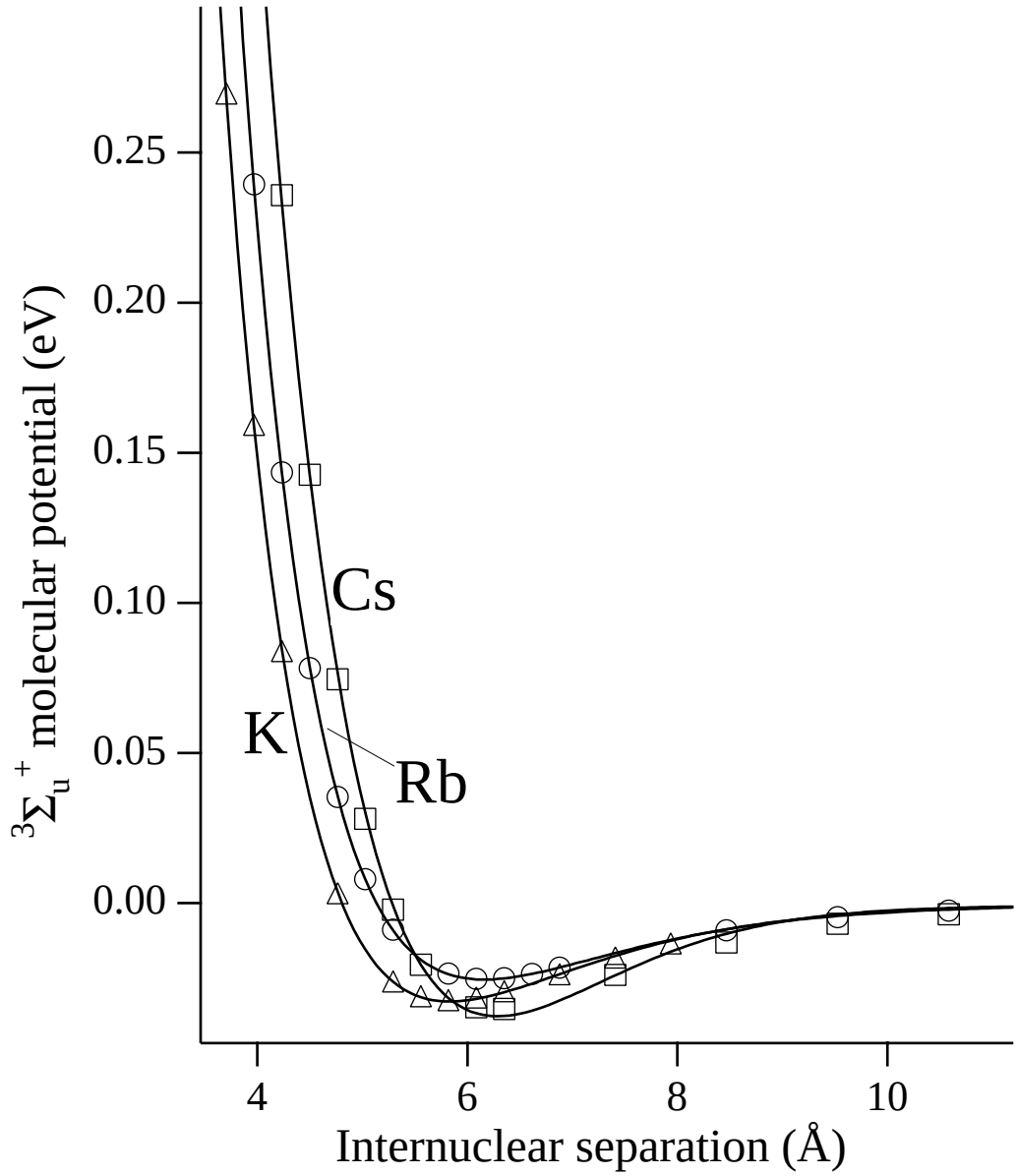

Figure 5.1: Homonuclear diatomic triplet potentials for K, Rb and Cs. The points plotted are the *ab inito* calculations of ref. [Krauss90]. The curves are a convenient analytical fit, parameterized in table 5.1

where $\hat{\mathbf{r}}_{\mathbf{12}}$ is the unit vector between the electrons. When this interaction is averaged over the electron wavefunctions and a collisional trajectory, the total electron polarization in the two atoms can change.

5.2.2 Correction Due to Electron Correlation

In order to simplify relaxation rate calculations, it is convenient to write the interaction in terms of the nuclear separation $\vec{\mathbf{r}}$ rather than the electronic separation $\vec{\mathbf{r}}_{\mathbf{12}}$. At large r, the distinction is not important, but at the small separation where relaxation occurs, they differ due to the spatial distribution of the electron charge and the correlation between the electrons' positions required by the Pauli principle. The following calculation allows us to estimate the importance of these effects.

We can take the wavefunction of the triplet state of an alkali dimer to be

$$\begin{aligned} \Psi(\mathbf{r}_1, \mathbf{r}_2) &= \psi(\mathbf{r}_1, \mathbf{r}_2)\, {}^3\chi \\ &= N[\varphi_A(1)\varphi_B(2) - \varphi_B(1)\varphi_A(2)]\, {}^3\chi \end{aligned} \tag{5.2}$$

where $\varphi_A(1)$ is a spatial orbital for electron 1 centered at nucleus A, N a normalizing factor, and ${}^3\chi$ is the (symmetric) spin part of the wavefunction. The expectation value of the spin-dipolar interaction can then be written as

$$\begin{aligned} &\langle\psi| \frac{\alpha^2 a_0^2 e^2}{r_{12}^3} \left(3\mathbf{S}_1 \cdot \hat{\mathbf{r}}_{12}\hat{\mathbf{r}}_{12} \cdot \mathbf{S}_2 - \mathbf{S}_1 \cdot \mathbf{S}_2\right) |\psi\rangle \\ &\quad = B_{SD} \langle {}^3\chi | 3\mathbf{S}_1 \cdot \hat{\mathbf{r}}\hat{\mathbf{r}} \cdot \mathbf{S}_2 - \mathbf{S}_1 \cdot \mathbf{S}_2 |\, {}^3\chi\rangle \end{aligned} \tag{5.3}$$

where

$$B_{SD}(r) = \alpha^2 a_0^2 e^2 \int d^3r_1 d^3r_2 \frac{3z_{12}^2 - r_{12}^2}{2r_{12}^5} |\psi(\mathbf{r}_1, \mathbf{r}_2)|^2. \tag{5.4}$$

I made the simplifying assumption that φ can be approximated as the unperturbed wavefunction of the alkali atom in its ground state. I then evaluated the integral 5.4 for K, Rb and Cs numerically using the valence electron wavefunction of ref. [Clementi74].

The effects of this averaging are shown for Rb in Fig. 5.2. Note that the electron correlation reduces the value of $B_{SD}(r)$ as compared to the point dipole approximation. The predicted relaxation rate is therefore also reduced slightly, as I discuss quantitatively in section 5.4.

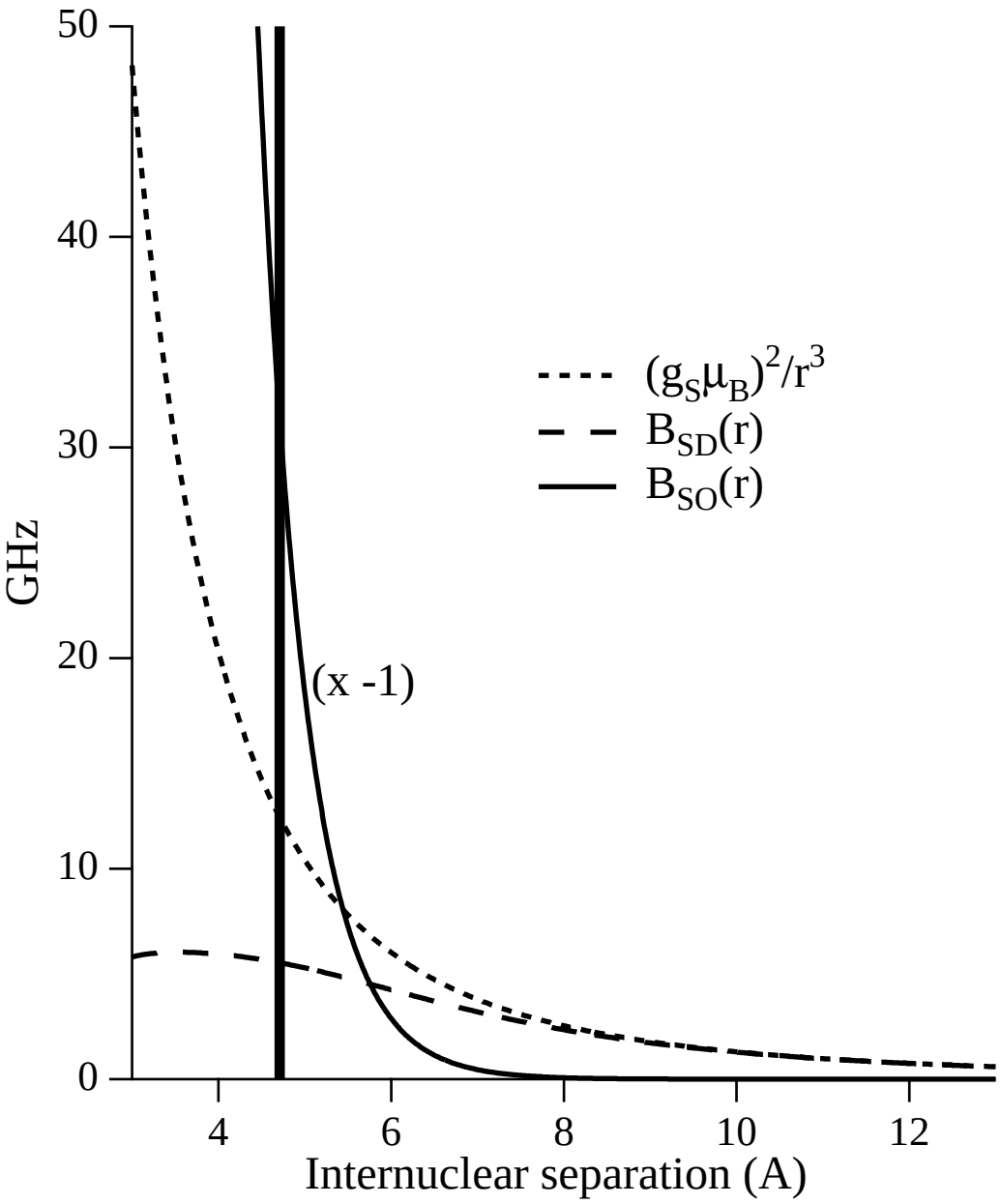

Figure 5.2: *ab initio* calculations of $B_{SO}(r)$ from ref. [Mies96], and $B_{SD}(r)$ for Rb (r is the internuclear separation). This shows the effect of electron correlations on the spin-dipolar interaction as compared to the uncorrected ($\sim 1/r^3$) interaction. The vertical solid line is at the classical turning point for a zero-impact parameter collision at kT collision energy. Note that B_{SO} is negative, so I have plotted -B_{SO} for comparison to the other quantities.

5.2.3 Second Order Spin-Orbit Coupling

The spin-dipolar is probably the largest spin-relaxation interaction in alkalis lighter than (and maybe including) K. However, the second order spin-orbit coupling is thought to be larger in Rb and Cs [Mies96].

The spin-orbit interaction arises from fine structure coupling of the electron spin to the admixture of $p_{\hat{\mathbf{r}}}$ in the Born-Oppenheimer ground state of two alkali atoms (hence the increase with alkali weight). Its first nonvanishing term is in second order, and it depends on the electron spins in the same way as the spin-dipolar interaction, but at short distance is proportional to wavefunction overlap.

In the context of ultracold collisions, Mies *et al.* [Mies96] recently published *ab initio* calculations of the second order spin-orbit interaction, which they parameterized as

$$B_{SO}(r) = -C\alpha^2 e^{-B(r-r_S)} \tag{5.5}$$

where, in atomic units, $B = 0.975, C = 0.001252, r_S = 10$ in Rb, $B = 0.830, C = 0.02249, r_S = 10$ in Cs, and C is assumed to be small in K.

5.2.4 Spin-Axis Interaction

The interaction is therefore the sum of the spin-orbit and spin-dipolar couplings. I will refer to the total interaction as the spin-axis coupling, which can be written in general as

$$V_{SA} = B_{SA}(r)\mathbf{S_1} \cdot (3\hat{\mathbf{r}}\hat{\mathbf{r}} - 1) \cdot \mathbf{S_2} \tag{5.6}$$

where $B(r) = B_{SD}(r) + B_{SO}(r)$. Equation 5.6 can also be written in the coupled spin basis $\mathbf{S} = \mathbf{S_1} + \mathbf{S_2}$ as

$$V_{SA} = \frac{B(r)}{2}\mathbf{S} \cdot (3\hat{\mathbf{r}}\hat{\mathbf{r}} - 1) \cdot \mathbf{S}. \tag{5.7}$$

5.3 Classical Trajectory Relaxation Rate Calculation

In a binary collision at temperatures of a few hundred Kelvin, many partial waves contribute to spin relaxation, so a classical path treatment should be adequate. We have published one such treatment in ref. [Kadlecek98C]. I present another, somewhat

different calculation below which leads to a slightly modified functional form of the answer, although the two results are exactly equivalent.

Once the potential between two alkali atoms is known, a collision can be completely described by specifying its impact parameter b, the initial relative velocity v and the angles θ and ϕ as shown in fig. 5.3. θ and ϕ represent rotations of the trajectory around two of the Euler angles. The problem is invariant under the third Euler rotation.

In order to compare the results of this calculation to the measurements presented in chapter 4, I define the rate coefficient κ in terms of the predicted relaxation rate Γ and alkali density $[A]$ as $\Gamma = \kappa[A]$. If I denote the fractional polarization loss along a trajectory as $F(b, v, \theta, \phi)$, the expected value of κ is found by averaging $F(b, v, \theta, \phi)$ over a Maxwellian velocity distribution $f(v)$ and a uniform distribution of collision directions as

$$\kappa = \frac{1}{1+\epsilon} \int_0^\infty f(v)\ v\ dv \int_0^\infty b\ db \int_0^{2\pi} d\phi \frac{1}{2} \int_0^\pi F(b, v, \theta, \phi) \sin(\theta) d\theta. \tag{5.8}$$

Note the inclusion of a slowing down factor $1/(1+\epsilon)$, which is a consequence of the hyperfine interaction acting between collisions (see appendix B). Since the collision time is so short, we may ignore the hyperfine interaction during the collision.

We can now calculate $F(b, v, \theta, \phi)$ by evolving the atomic density matrix $\rho_0 \rightarrow \rho_F$ during the collision. Since we are interested in predicting relaxation rates and their magnetic field dependences, I will evolve the density matrix according to the interaction Hamiltonian

$$H = V_{SR} + g_S \mu_B B\ S_Z \tag{5.9}$$

If we introduce the polarization operator $P(\rho) = \sum_m m\rho_{mm}$ then

$$F(b, v, \theta, \phi) = \frac{P(\rho_0 - \rho_F)}{P(\rho_0)} \tag{5.10}$$

Note that eq. 5.9 does not cause transitions between the singlet and triplet manifolds, so we need only consider the triplet manifold in this calculation. The polarization operator is therefore simply $P(\rho) = \rho_{11} - \rho_{-1-1}$.

Next, we calculate $\rho_F = U^\dagger \rho_0 U$ by expanding the time evolution operator U as

$$U = 1 + (-\frac{i}{\hbar}) \int_{-\infty}^{\infty} dt\ H(t) + (-\frac{i}{\hbar})^2 \int_{-\infty}^{\infty} dt \int_{-\infty}^{\infty} dt' H(t) H(t') + \ldots \tag{5.11}$$

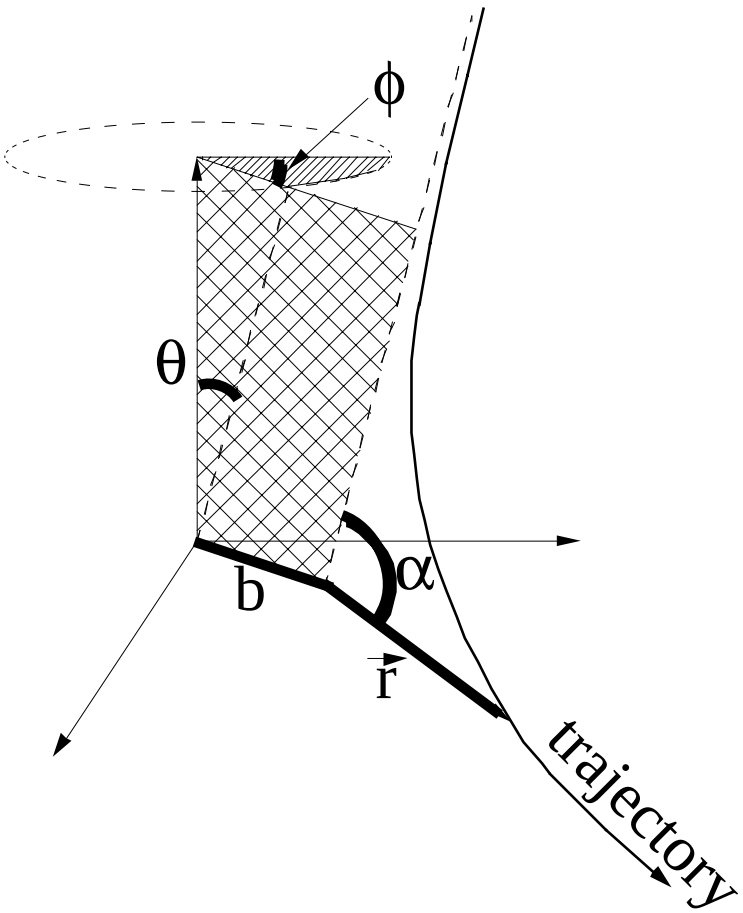

Figure 5.3: Classical alkali-alkali binary collision trajectory. The shape of the trajectory is entirely determined by electrostatic forces, so we calculate a reference trajectory once for each initial velocity v and impact parameter b. The reference trajectory is in the xz plane, its initial velocity is in the -$\hat{\mathbf{z}}$ direction, and the internuclear separation $\hat{\mathbf{r}}_{\mathbf{ref}}(\mathrm{t})$ makes angle $\alpha(\mathrm{t})$ with the $\hat{\mathbf{z}}$ axis. Having calculated this trajectory once, any trajectory with the same b and v can be found by rotating the reference trajectory through the Euler angles $R_x(\theta)R_z(\phi)$. The problem is invariant under the third Euler rotation.

Combinding eqs. 5.11 and 5.10, and keeping only terms up to second order gives

$$\begin{aligned} F(b,v,\theta,\phi) &= -\frac{i}{\hbar}\int_{-\infty}^{\infty}\frac{P([H(t),\rho_0])}{P(\rho_0)} \\ &\quad +\frac{1}{\hbar^2}\int_{-\infty}^{\infty}dt\int_{-\infty}^{\infty}dt'\frac{P\left(H(t)\rho_0 H(t') - \frac{1}{2}[H(t)H(t'),\rho_0]\right)}{P(\rho_0)}. \end{aligned} \tag{5.12}$$

Substituting the explicit form of H from eq. 5.9 and assuming that the initial state ρ_0 is in spin temperature equilibrium (see appendix B), eq. 5.12 reduces to

$$F(b,v,\theta,\phi) = \frac{9}{32\hbar^2}\int_{-\infty}^{\infty}dt\int_{-\infty}^{\infty}dt' B(r)B(r')\left(r_+ r_z r'_- r'_z + r_+^2 r'^2_-\right) \tag{5.13}$$

where $r_{+,-,z}$ and $r'_{+,-,z}$ are the components of the unit vector between the alkali nuclei at time t and t', respectively. Note that there is no dependence on magnetic field up to second order. Although the field does have a small effect in third and higher orders, I have verified that the predicted field decoupling in all three alkalis is less than 1% at 1 Tesla. The effect of the field is therefore negligible, in agreement with the qualitative discussion of section 4.4.

Finally, we must integrate eq. 5.8 over angles (θ,ϕ). Since the trajectory is entirely determined by rotationally invariant electrostatic interactions, we can do this by calculating a reference trajectory $\vec{\mathbf{r}}_{ref}$(t) and rotating it as $\vec{\mathbf{r}}(t) = R_x(\theta)R_z(\phi)\vec{\mathbf{r}}_{ref}$. We may choose the reference trajectory to be in the xz plane with $\vec{\mathbf{r}}_{\mathbf{ref}}(-\infty) = \hat{\mathbf{z}}$. If we define the angle α as $\cos(\alpha) = \vec{\mathbf{r}}_{\mathbf{ref}}\cdot\hat{\mathbf{z}}$ (see fig. 5.3), then we may substitute $\vec{\mathbf{r}} = \mathbf{R_x}(\theta)\mathbf{R_z}(\phi)\left(\hat{\mathbf{z}}\cos(\alpha)+\hat{\mathbf{x}}\sin(\alpha)\right)$ and perform the integrals over θ and ϕ in eq. 5.8 yielding

$$\kappa = \frac{3\pi}{8(1+\epsilon)}\int_{-\infty}^{\infty} f(v)\, v\, dv\int_{-\infty}^{\infty} b\, db\left(\varphi_0^2 + 3(\varphi_{sc}^2 - \varphi_{ss}\varphi_{cc})\right) \tag{5.14}$$

where

$$\varphi_0 = \hbar\int_{-\infty}^{\infty}dt\; B(r(t)) \qquad \varphi_{sc} = \hbar\int_{-\infty}^{\infty}dt\; B(r(t))\sin(\alpha(t))\cos(\alpha(t))$$

$$\varphi_{ss} = \hbar\int_{-\infty}^{\infty}dt\; B(r(t))\sin^2(\alpha(t)) \qquad \varphi_{cc} = \hbar\int_{-\infty}^{\infty}dt\; B(r(t))\cos^2(\alpha(t)) \tag{5.15}$$

	Prediction	Experiment
K	$4.3\times10^{-16}\mathrm{cm}^{-3}/\mathrm{s}$	$1.6\times10^{-14}\mathrm{cm}^{-3}/\mathrm{s}$
Rb	$2.5\times10^{-16}\mathrm{cm}^{-3}/\mathrm{s}$	$4.1\times10^{-14}\mathrm{cm}^{-3}/\mathrm{s}$
Cs	$2.0\times10^{-14}\mathrm{cm}^{-3}/\mathrm{s}$	$3.7\times10^{-13}\mathrm{cm}^{-3}/\mathrm{s}$

Table 5.2: Predicted spin-relaxation rate coefficients using the second order spin-rotation interactions of ref. [Mies96] and the theory developed in this chapter. For comparison, the experimentally determined alkali-alkali relaxation coefficients from chapter 4 are included as well. Note that the theoretical rates are an order of magnitude too small for all of the alkalis and two orders of magnitude too small for Rb.

5.4 Numerical Results and Comparison to Experiment

I integrated eq. 5.14 numerically by calculating the classical trajectories $r_{ref}(t), \alpha(\mathrm{t})$ for $0 \leq b \leq 100a_0$ in 0.1 a_0 increments and $0 < v < 10\sqrt{2kT/m}$ in $0.01\sqrt{2kT/m}$ increments. The resulting rate coefficients are given in table 5.2 along with the experimental values for alkali-alkali relaxation from chapter 4. Note that the predicted relaxation rates are one or two orders of magnitude smaller than the experimentally observed rates.

In addition, the theory predicts negligible decoupling in a magnetic field, which is at odds with the substantial field dependence shown in chapter 4.

These significant discrepancies lead me to reject the idea that alkali-alkali relaxation is taking place during binary alkali collisions. Even if one supposes that the second order spin-orbit calculations of Mies, *et al.* are sufficiently in error to explain our measured rates, the observed field dependence is impossible to explain with the model presented here. Note that because of its failure to account for resonance effects, the semi-classical approach is certainly suspect for collisions near the top of the molecular rotational barrier. However, as I show in chapter 6, there are few enough such collisions that treating them correctly does not change the results quoted in this chapter appreciably.

It is possible that relaxation in binary collisions could explain the field-independent part of alkali-alkali relaxation. If we scale the second order spin-orbit calculations of ref. [Mies96] by a 2.5 for Cs, 7 for Rb, and suppose that the spin-orbit coupling is not negligible in K, the predicted relaxation rates can be brought into agreement. However, this leaves us to explain the field-dependent component of alkali-alkali relaxation by an entirely different microscopic mechanism. In addition, such an increase in the spin-orbit couplings presents difficulties because the predicted relaxation rate in alkali triplet

dimers becomes larger than the observed alkali-alkali relaxation rate. Thus, we must additionally suppose that relaxation in triplet dimers is somehow suppressed. This issue is discussed in detail in the next chapter.

Chapter 6

Model of Relaxation in Alkali Triplet Molecules

In this chapter, I describe a model of relaxation in alkali triplet dimers, including metastable dimers formed thorough resonant alkali-alkali collisions. I will show that the expected relaxation rate is strongly pressure dependent, and therefore does not explain the pressure-independent alkali-alkali relaxation.

In section 6.1, I explain the method I used to calculate the equilibrium triplet dimer density and give the resulting chemical equilibrium coefficient. I discuss the spin-axis interaction in triplet molecules in section 6.2 and present estimates of three-body molecular formation, dissociation and reorientation rates in section 6.3. In section 6.4, I use the results of the previous sections to calculate the expected relaxation rate in triplet dimers, highlighting in particular its strong dependence on buffer gas pressure. I clarify the circumstances under which the hyperfine interaction can mimic a pressure-independent relaxation mechanism in section 6.5, and show that this limited pressure independence is not sufficient to explain alkali-alkali relaxation. Finally, I discuss how this model could be made pressure independent if triplet molecules form without the presence of a third body. I estimate the formation rates from two such mechanisms in section 6.6, and show that they are far too small to explain alkali-alkali relaxation.

As might be expected, there are substantial similarities between a model describing relaxation in triplet molecules and the model for singlet molecular relaxation presented in chapter 3. I will therefore refer to chapter 3 where appropriate, but point out where

the larger spin-axis coupling strength and the smaller molecular binding energy in triplet molecules cause different behavior. It is important to note, however, that in contrast to chapter 3, the purpose of this chapter is to show that that triplet dimers can *not* explain the observed alkali-alkali relaxation rates. Therefore, instead of using experimental data to fix model parameters as in chapter 3, I must estimate the parameter values and show that the model does not work for any reasonable modifications of those values.

6.1 Equilibrium Triplet Dimer Density

The triplet dimer differs from the singlet dimer in two important respects. First, because the electrons are coupled into a triplet state, relaxation is possible through direct magnetic coupling to the electron spins. This is likely to produce much faster relaxation rates due to the larger magnetic moment. However, the binding energy of the triplet dimer is only about $k_B T$, which is more than an order of magnitude less than that of the singlet dimer. Therefore, the equilibrium density is reduced by more than a factor of 10^4.

The first step in calculating the equilibrium triplet dimer density is to find the eigenstates of the Born-Oppenheimer potential. The ${}^3\Sigma_u^+$ potential is the same one that governs the dynamics of binary collisions as discussed in chapter 5. See section 5.1 for a plot and a convenient parameterization of this potential.

As in section 3.1 for the singlet dimers, I determined eigenstate energies of this potential numerically and summed over the states, weighted by a Boltzmann factor, to determine the chemical equilibrium coefficient as

$$\begin{aligned} {}^3k_{chem} &= \sum_i {}^3k_{chem,i} \\ {}^3k_{chem,i} &= \frac{3}{8}\left[\frac{h^2}{\pi m k T}\right]^{3/2} e^{-E_i/kT}(2\mathrm{J}_i+1) \end{aligned} \tag{6.1}$$

where m is the atomic mass and E_i, J_i are the energy and rotational angular momentum of the i'th energy eigenstate (see fig. 6.1 for the calculated eigenstate energies). Note that eq. 6.1 is identical to eq. 3.1 except for a factor of 3 to account for the spin degeneracy of the triplet state, and the introduction of the individual chemical equilibrium coefficient $k_{chem,i}$ of each energy eigenstate. The density of triplet dimers of alkali species A is

	a_0	a_1	a_2
K	2548	-6.845	5.302×10^{-3}
Rb	1834	-4.866	3.741×10^{-3}
Cs	3269	-8.808	6.842×10^{-3}

Table 6.1: Parameterized fit to ${}^3k_{chem}$. ${}^3k_{chem} = \sum a_n (T/K)^n \mathring{A}^3$

then

$$\begin{aligned} \left[{}^3A_2\right]_i &= {}^3k_{chem,i}\left[A\right]^2 \\ \left[{}^3A_2\right] &= {}^3k_{chem}\left[A\right]^2 . \end{aligned} \tag{6.2}$$

Table 6.1 gives a parameterized fit to ${}^3k_{chem}(T)$ for K, Rb and Cs, and Fig. 6.2 shows $k_{chem}(T)$ and the calculated fraction of alkali atoms bound in triplet dimers.

One interesting feature of triplet dimers is that a significant fraction of them have positive energy with respect to dissociation, as can be seen in fig. 6.1. This opens up the possibility of spontaneous dimer formation and breakup and is discussed in more detail in section 6.6.

6.2 Spin-Axis Coupling

Relaxation in a triplet dimer and in a binary collision are similar in that the electrons are coupled in the triplet state, so relaxation is almost certainly caused by the same spin-axis interaction in either case. The one significant difference, however, is that the interaction time in a triplet dimer is sufficiently long that the arguments of section 4.4 do not apply, and we would expect relaxation in a triplet dimer to be decoupled by a magnetic field.

As in section 5.2, the total electronic spin relaxes through the interaction

$$V_{SA} = \frac{B_{SA}}{2}(r)\mathbf{S}\cdot(3\hat{\mathbf{r}}\hat{\mathbf{r}} - \mathbf{1})\cdot\mathbf{S} \tag{6.3}$$

in which $\hat{\mathbf{r}}$ is the unit vector between the two nuclei. To calculate an effective interaction for each molecular eigenstate, we must average $B(r)$ over the radial part and $(3\hat{\mathbf{r}}\hat{\mathbf{r}} - \mathbf{1})$ over the angular part of the molecular wavefunction.

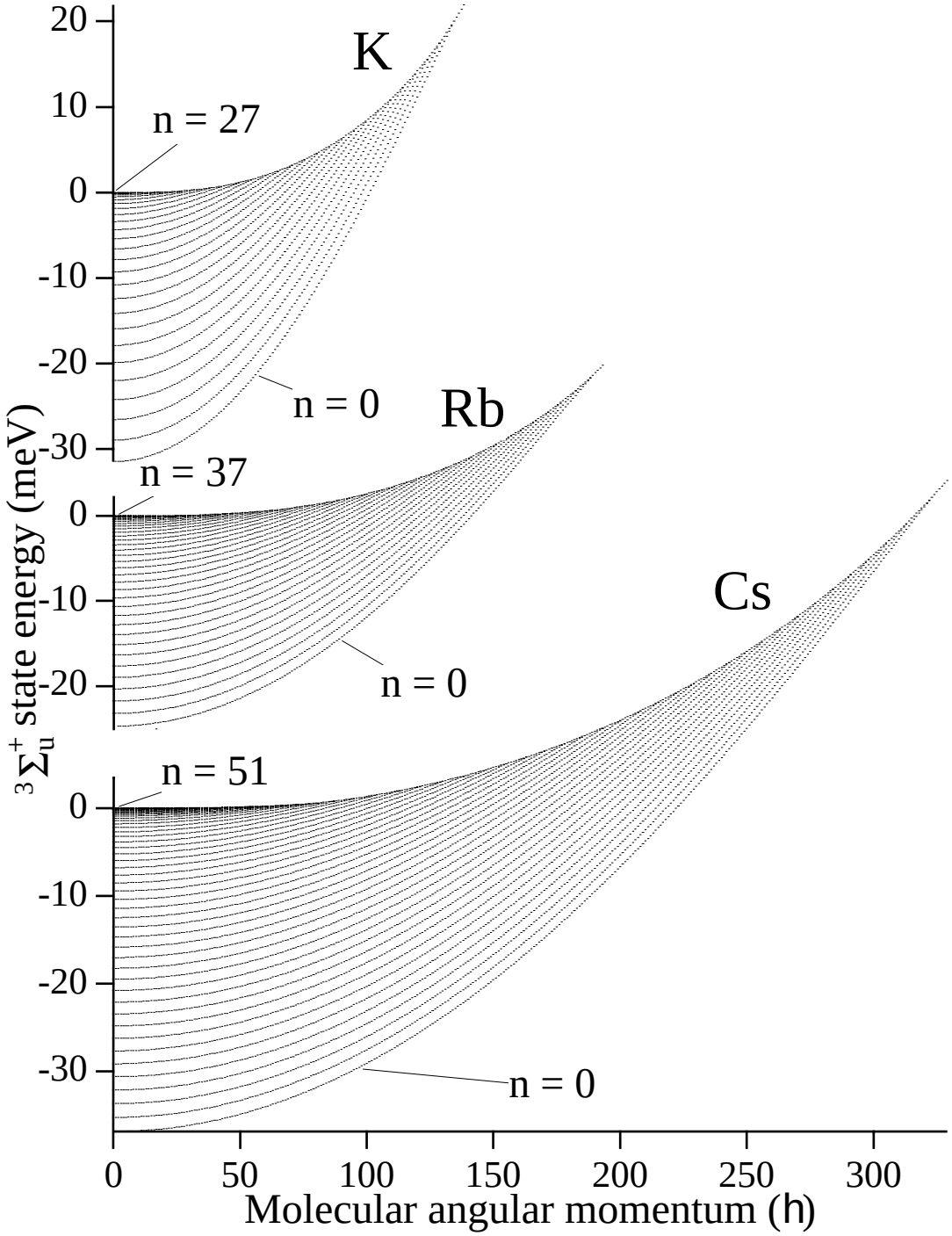

Figure 6.1: Alkali $^3\Sigma_u^+$ molecular eigenstate energies. Each upward-curving series corresponds to a different vibrational quantum number, starting from n = 0 at the bottom. The number of bound states for J=0 is listed for each alkali. All three alkalis have the same horizontal scale.

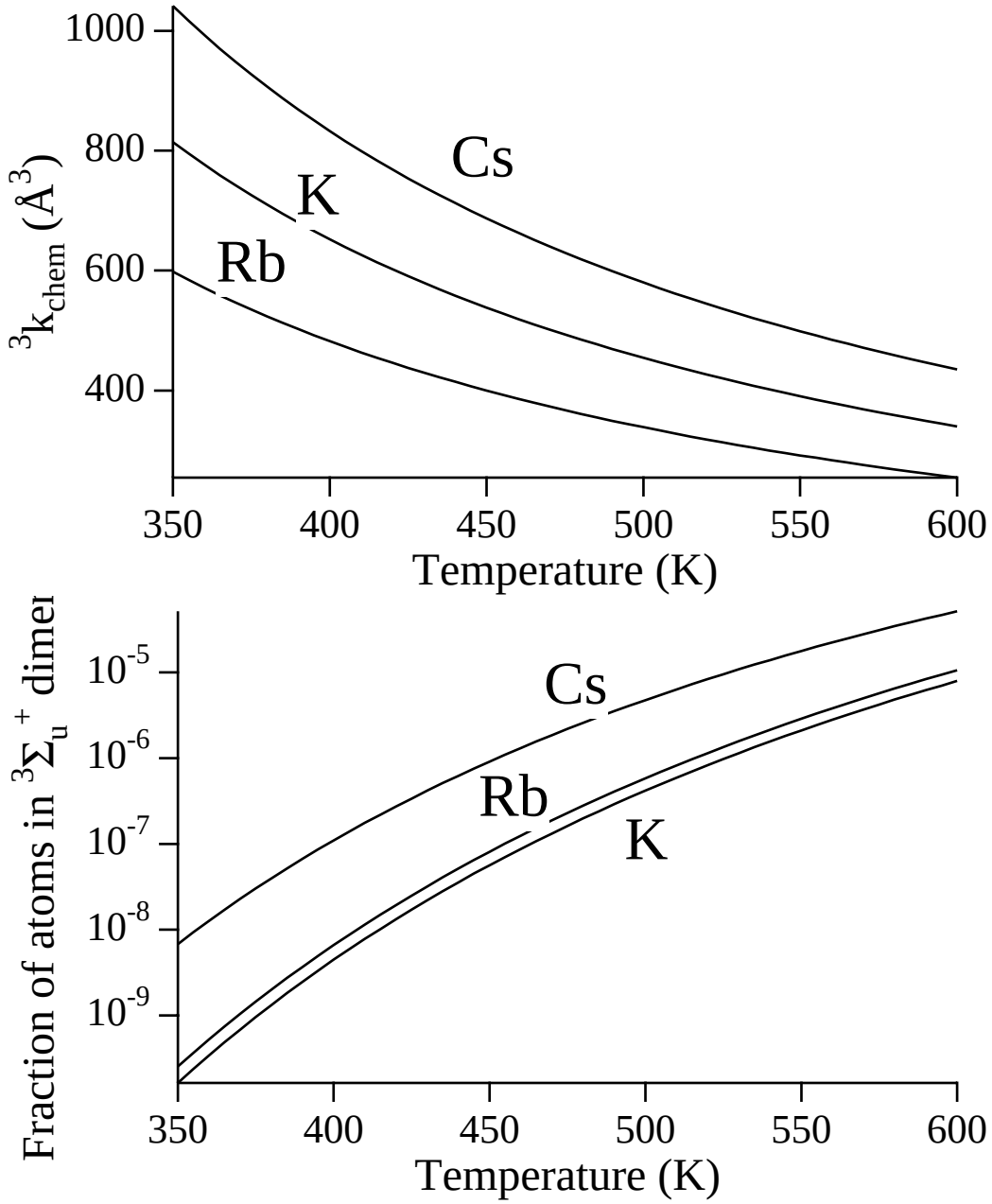

Figure 6.2: Chemical equilibrium coefficients for the alkali $^3\Sigma_u^+$ dimers, and fraction of the atoms in the vapor contained in triplet dimers. Note the extremely weak temperature dependence of the chemical equilibrium coefficient. This is due to the small binding energy of triplet dimers.

The angular average of $3\hat{\mathbf{r}}\hat{\mathbf{r}} - \mathbf{1}$ for a molecular state $|Jm_J\rangle$ is well known (see, for instance, ref. [Townes]) and can be used to replace $\hat{\mathbf{r}}$ by the more convenient molecular angular momentum $\mathbf{J}$. This averaging was used to arrive at eq. 3.3. By analogy with the approximations used to turn eq. 3.3 into the simpler eq. 3.5, it is sufficient to keep only one term of the angular average

$$\langle 3\hat{\mathbf{r}}\hat{\mathbf{r}} - \mathbf{1}\rangle \approx \frac{\mathbf{1}}{\mathbf{2}}(\mathbf{3}\hat{\mathbf{J}}\hat{\mathbf{J}} - \mathbf{1}) \tag{6.4}$$

Unfortunately, because of the strong anharmonicity of the triplet potential, the radial average of $B_{SA}(r)$ has no comparable analytic approximation. I have therefore calculated the averaged coupling strengths individually for each molecular ro-vibrational state i

$$B_{SA,i} = \int dr\ u_i^* u_i B_{SA}(r) \tag{6.5}$$

with $B_{SA}(r)$ as specified in section 5.2 and the radial wavefunctions $u(r)$ calculated numerically. Figure 6.3 shows the values of this interaction for each Rb_2 molecular state. This gives a sense of the scale and variability of B_{SA}. The corresponding values have a similar variability in K_2 and Cs_2, although the scale is slightly smaller for K and about an order of magnitude larger in Cs.

Having performed these averages, I now write the spin-axis interaction for molecular state i as

$$V_{SA,i} = \frac{B_{SA,i}}{4}\mathbf{S}\cdot(\mathbf{3}\hat{\mathbf{J}}\hat{\mathbf{J}} - \mathbf{1})\cdot\mathbf{S} \tag{6.6}$$

6.3 Three-Body Dissociation, Formation and Reorientation

As is the case with singlets, triplet molecules are formed, dissociated and reoriented by collisions with the buffer gas. Unlike singlet molecules, however, the small triplet binding energy leads to essentially no suppression of three-body formation and breakup. So, whereas these processes can be safely ignored when dealing with relaxation in singlet dimers, they almost certainly dominate triplet molecular dynamics. To verify this claim, I include a calculation of triplet dimer formation via alternate mechanisms (section 6.6), and show that three-body formation gives by far the largest contribution at pressures above a few Torr.

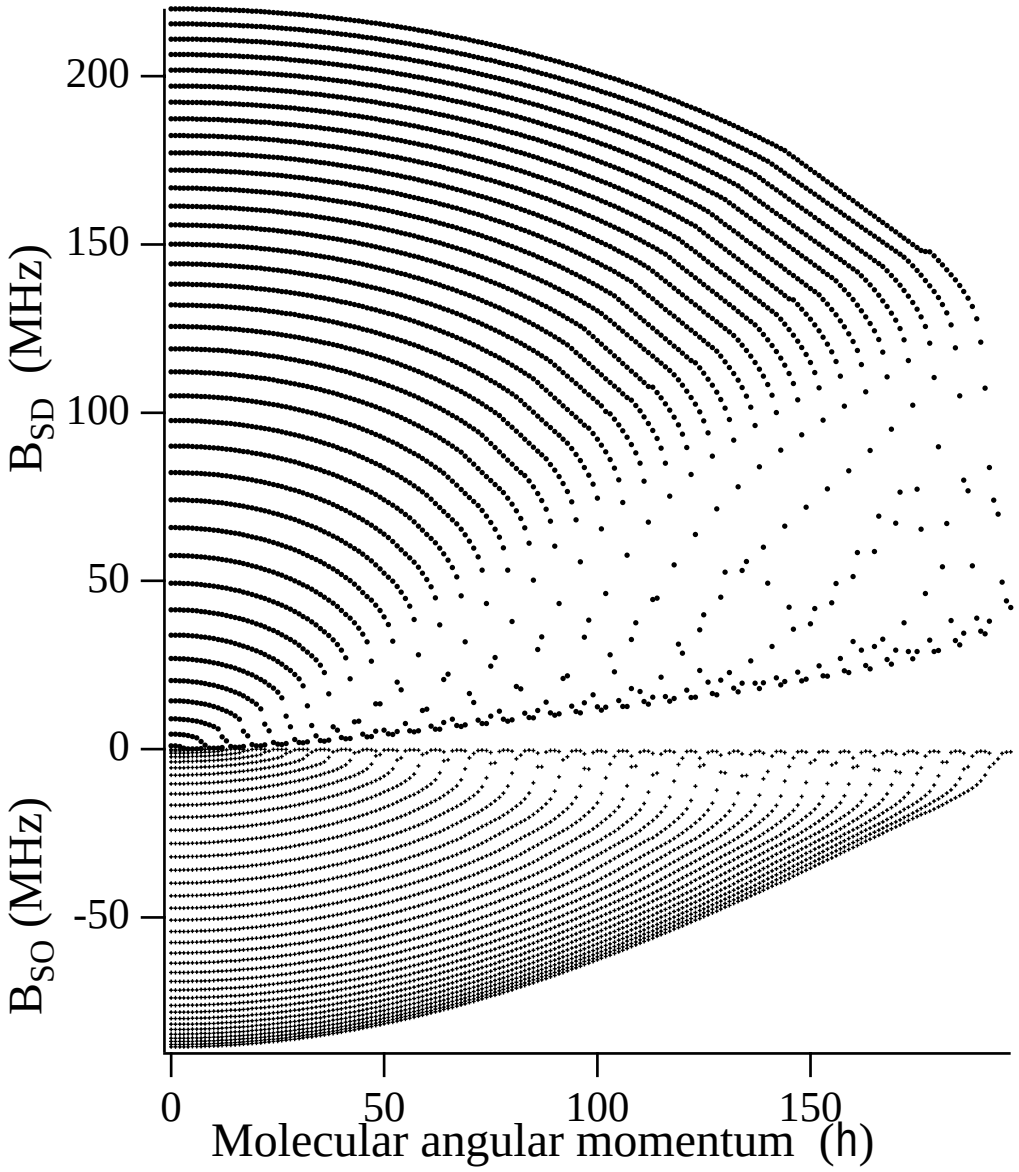

Figure 6.3: Average spin-dipolar (positive values) and spin-orbit (negative) couplings for a $^3Rb_2$ molecule as a function of molecular state. The total spin-axis interaction is the sum of these two interactions and is therefore approximately the same size as the spin-orbit coupling alone. Each curving series of points corresponds to a different vibrational quantum number. Note the large variation in coupling strength with molecular state. The magnitude of the coupling decreases with vibrational and rotational quantum number.

	σ_b	σ_J
K in He	$0.95\mathring{A}^2$	$6.1\mathring{A}^2$
K in N_2	$3.1\mathring{A}^2$	$17\mathring{A}^2$
Rb in He	$1.1\mathring{A}^2$	$3.3\mathring{A}^2$
Rb in N_2	$3.4\mathring{A}^2$	$12\mathring{A}^2$
Cs in He	$0.23\mathring{A}^2$	$2.0\mathring{A}^2$
Cs in N_2	$0.95\mathring{A}^2$	$8.8\mathring{A}^2$

Table 6.2: Estimates of reorientation (σ_J) and breakup (σ_b) cross-sections for alkali dimers in He and N_2. These values are a result of a classical-trajectory simulation described in appendix D.

I characterize three-body formation and breakup using the breakup cross-section σ_b for alkali triplet dimer ${}^3A_2$ and buffer gas species B in terms of the mean molecular lifetime $1/\tau_b = [B]\langle\sigma_b v_{A_2\cdot B}\rangle$. I characterize molecular reorientation using σ_J, τ_J as in section 3.3.2. Note that it does not take very many buffer gas collisions to break up the weakly bound triplet molecule, and molecular reorientation is essentially the same in both types of molecules. Therefore, we expect both the breakup and reorientation cross-sections to be roughly the kinetic cross-section, or $O(10\mathring{A}^2)$.

I used a classical trajectory molecular dynamics simulation (described in appendix D) to refine this estimate somewhat, and the results appear in table 6.1. The simulation was designed to reproduce measured value of σ_J for ${}^1Rb_2$ in N_2 (chapter 3). However, given the limitations of a classical approach and the lack of experimental ${}^3\Sigma_u^+$ binding energies, these values are still approximate.

Having calculated the equilibrium density of each state in section 6.1, and estimated the dissociation rate above, we may now write the rate at which alkali atoms enter triplet dimers ($1/\tau_F$) using detailed balance

$$2\,[{}^3A_2]/\tau_b = [A]/\tau_F \tag{6.7}$$

or, for each triplet state i,

$$\frac{1}{\tau_{F,i}} = 2\,{}^3k_{chem,i}[A][B]\langle\sigma_b v_{A_2\cdot B}\rangle \tag{6.8}$$

6.4 Relaxation Rate Calculation

The calculation of relaxation rates may now proceed in a manner analagous to section 3.4. The total relaxation rate is the product of the formation rate and the fraction of polarization lost during a typical molecular lifetime. Using eq. 3.26, we may write this as

$$\Gamma_{trip} = \sum_i \frac{1}{\tau_{F,i}} \frac{1 + \langle N \rangle) F_{J,i}(\tau_c)}{1 + \langle N \rangle F_{J,i}(\tau_c)} \tag{6.9}$$

where $F_J(\tau_c)$ is the average fractional polarization lost before either a molecular reorientation or dissociation halts coherent evolution and $\langle N \rangle = \tau_b/\tau_J = \sigma_J/\sigma_b$. As in section 3.3, the periods of coherent evolution are distributed as $\frac{1}{\tau_c} e^{-\tau/\tau_c}$ with $1/\tau_c = 1/\tau_J + 1/\tau_b$.

In the absense of nuclear spin, F_J may also be calculated in the manner described in section 3.4, leading to the analytic form of eq. 6.12. However, the molecular lifetime is long enough that the hyperfine structure can not be ignored. Nor can it be treated perturbatively since, although the spin-axis coupling varies between molecular states, the two interactions are of similar strength. Therefore, as was true for singlet molecule relaxation in a magnetic field, the only solution is to diagonalize the full interaction Hamiltonian as per appendix C. The Hamiltonian I have used to describe relaxation in triplet molecules is

$$H_i = V_{SA,i} + \frac{A_1}{2} \mathbf{I}_1 \cdot \mathbf{S} + \frac{A_2}{2} \mathbf{I}_2 \cdot \mathbf{S} + g_S \mu_B B S_z \tag{6.10}$$

Thus, in order to calculate the appropriate values of $F_J(\tau_c)$ to use in eq. 6.9, I diagonalized eq. 6.10 numerically for many values of the spin-axis interaction strength B_{SA} and molecular coherence time τ_c, and for each of the alkali dimers $^{39}K_2$, $^{85,85}Rb_2$, $^{85,87}Rb_2$, $^{87,87}Rb_2$ and $^{133,133}Cs_2$. A typical $F_J(\tau_c)$ (for a $^{85,85}Rb_2$ dimer state with $B_{SA,i}$ equal to the hyperfine coupling constant A) is shown in fig. 6.4. Note the qualitative similarity to the analytic $F_J(\tau_c)$ calculated for singlet molecules in section 3.4– at short τ_c, the fractional relaxation is proportional to τ_c^2, and it saturates at a relaxation fraction of 2/3 (due to angular averaging of $\hat{\mathbf{J}}$) at a characteristic value of τ_c. As B_{SA} is changed, the qualitative behavior stays roughly the same, although the short time proportionality constant and saturation value of τ_c shift.

We may use this qualitative behavior and eq. 6.9 to predict the pressure dependence

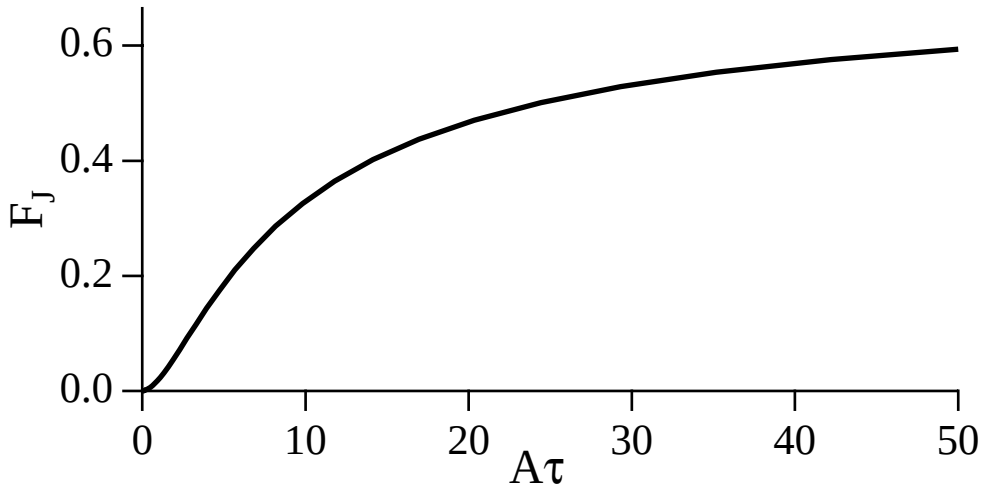

Figure 6.4: $F_J(\tau_c)$, the average fraction of polarization lost during molecular evolution of average duration τ_c (A is the hyperfine coupling and this calculation is for two spin 5/2 nuclei). Note the quadratic dependence on τ_c at small τ_c and the eventual saturation at $F_J = 2/3$ at sufficiently large τ_c. This behavior comes from very general principles of quantum mechanics, and is independent of the form of the relaxing interaction. The details of the interaction are manifest as the intermediate τ_c behavior.

of the total relaxation rate. At high pressure,

$$\Gamma_{trip} \rightarrow \Sigma_i \frac{1}{\tau_{F,i}}(1 + \langle N \rangle) F_{J,i}(\tau_c). \tag{6.11}$$

From eq. 6.8, $1/\tau_{F,i}$ is proportional to buffer gas pressure P, $(1+\langle N \rangle)$ independent of P and, since $F_{J,i}$ is proportional to $1/P^2$, the relaxation rate must fall off as $1/P$. Identical behavior was predicted, and observed, for relaxation in singlet molecules. In fact, this high pressure behavior is a general feature of short time evolution in quantum mechanics, so it is independent of the details of the interaction causing relaxation.

Similarly, as $F_{J,i}$ saturates at low pressure, the last factor of eq. 6.9 becomes pressure independent, giving a total relaxation rate that is proportional to pressure. This behavior is different from relaxation in singlet dimers because the dominant triplet molecule formation mechanism is three-body formation, which occurs at a rate proportional to buffer gas pressure, as opposed to chemical exchange, which is pressure independent.

If we use the full form of eq. 6.9, along with the $E_i, B_{SA,i}$, and cross-sections esti-

mated above, the calculated relaxation rate varies with pressure just as this qualitative discussion suggests. Figure 6.5 shows the expected rate coefficient for K, Rb and Cs in He and N_2 buffer gas, and its variation with buffer gas pressure. Note the linear pressure dependence at low pressure and inverse pressure dependence at high pressure. As summarized in chapter 4, I have measured alkali-alkali rate coefficients over the entire pressure range shown in fig. 6.5 (about three orders of magnitude) and I do not see any pressure dependence at all, much less the strong pressure dependence predicted by this model.

Except as noted in section 6.5, the shape of fig. 6.5 is a very general feature of relaxation in a weakly bound system. For instance, relaxation has been measured in the similarly weak Rb-Xe Van Der Waals molecule ([Bouchiat71]), and it exhibits a pressure dependence very similar to what I have predicted for alkali triplet dimers. In both cases, the pressure dependence can be argued from general quantum and statistical arguments that do not depend on the values of the model parameters, or even the form of the interaction causing relaxation. I therefore find that it is impossible to reproduce the pressure independence of alkali-alkali relaxation by changing the values of σ_b, σ_J or B_{SD}.

Certainly, the model presented above does not incorporate all of the many subtleties of triplet molecule dynamics. I have tried to consider all physically reasonable modifications, but I do not find any way that relaxation in triplet molecules can be made pressure independent. Pressure independence would require either that the shape of $F_J(\tau_c)$ be substantially changed, or that the formation and breakup of triplet dimers proceed other than via three-body processes. In the next two sections, I describe my investigations of both of these possibilities, and why I believe they cannot help resolve this discrepancy.

6.5 The Effect of Hyperfine Structure

Although hyperfine structure is included in the full interaction Hamiltonian of eq. 6.10 and the predictions shown in fig. 6.5, I include this section to give an intuitive feel for the effect of nuclear spin, the conditions under which the hyperfine coupling can lead to limited pressure independence, and why that pressure independence is insufficient to allow relaxation in triplet dimers to explain the observed alkali-alkali relaxation rates.

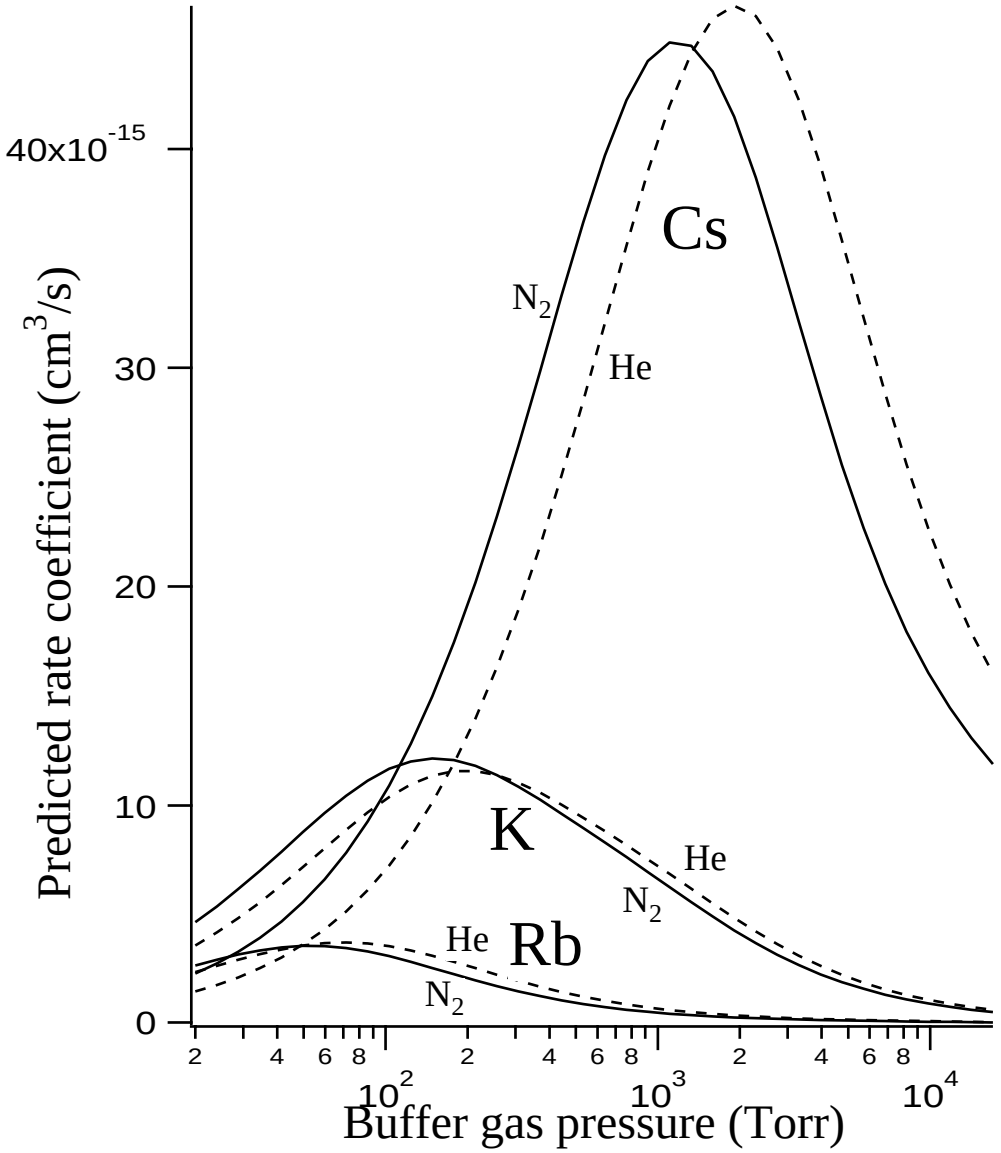

Figure 6.5: Predicted rate coefficients for K, Rb and Cs in He and N_2 buffer gas. Note that the predicted coefficients are less than, but within about an order of magnitude of, my measurements of alkali-alkali relaxation (chapter 4), but the large predicted pressure dependence does not match my observations.

We can extend the qualitative argument of section 6.4 to investigate what happens around the transition between the low pressure limit ($\Gamma_{trip} \propto$ buffer gas pressure P) and the high pressure limit ($\Gamma_{trip} \propto 1/P$). In the absense of nuclear spin, relaxation in a triplet molecule is formally identical to the relaxation of a spin 1 nucleus via the quadrupole interaction. Therefore, just as in section 3.4.2, we can write an analytic expression for $F_J(\tau_c)$

$$F_J(\tau_c) = \frac{2}{3}\frac{[(B_{SA}/\hbar)\tau_c[^2}{1+[(B_{SA}/\hbar)\tau_c]^2} \tag{6.12}$$

which leads to an analytic form for the relaxation rate

$$\Gamma_{trip} = \frac{4\ {}^3k_{chem}[A][B]\sigma v}{(3+2\langle N\rangle)+3\left([B]\sigma v/(B_{SA}/\hbar)\right)^2} \tag{6.13}$$

in which $\sigma v = \langle(\sigma_J+\sigma_b)v_{B\cdot A_2}\rangle$, $[A]$ and $[B]$ are alkali and buffer gas number density. The maximum relaxation rate, which marks the transition between the low and high pressure limits, occurs when the two terms in the denominator are equal. Note that eq. 6.13 transitions smoothly from linear to inverse pressure dependence. That behavior originates in the similarly smooth transition of eq. 6.12 from quadratic τ_c dependence to τ_c independence near $(B_{SA}/\hbar)\tau_c = 1$. In order for the relaxation rate to be independent of pressure, $F_J(\tau_c)$ must depend linearly on τ_c near $F_J = \sigma_J/\sigma_b$.

We might hope for some flattening of eq. 6.13 with the inclusion of hyperfine structure. Depending on which of the spin-axis or hyperfine interactions is larger, the nuclear coupling causes one of three things to happen; If $B_{SA} \ll A$, the coupled atomic spin $\mathbf{F}$ relaxes by interacting with the molecular angular momentum $\mathbf{J}$. This is formally identical to nuclear relaxation due to the electric quadrupole interaction (chapter 3), so $F_J(\tau_c)$ has a familiar shape, as is shown at the top of fig. 6.6 with a calculation of $F_J(\tau_c)$ for $B_{SA} = A/100$. There is no range of τ_c for which $F_J \propto \tau_c$.

If $B_{SA} \gg A$, the electrons relax quickly and we may ignore the nucleus for short times. Then, at times $\gg \hbar/A$, the nucleus relaxes by interacting with the strongly coupled $\mathbf{J}+\mathbf{S}$. I show this limit with a calculation of $F_J(\tau_c)$ for $B_{SA} = 100A$ in the middle of fig. 6.6. As before, there is no extended range for which $F_J \propto \tau_c$.

For $B_{SA} \approx A$, there is a range of τ_c for which $F_J \propto \tau_c$, as demonstrated at the bottom of fig. 6.6. This is the condition required for a pressure independent relaxation rate. Nonetheless, I find that this matching of coupling strengths can not explain our

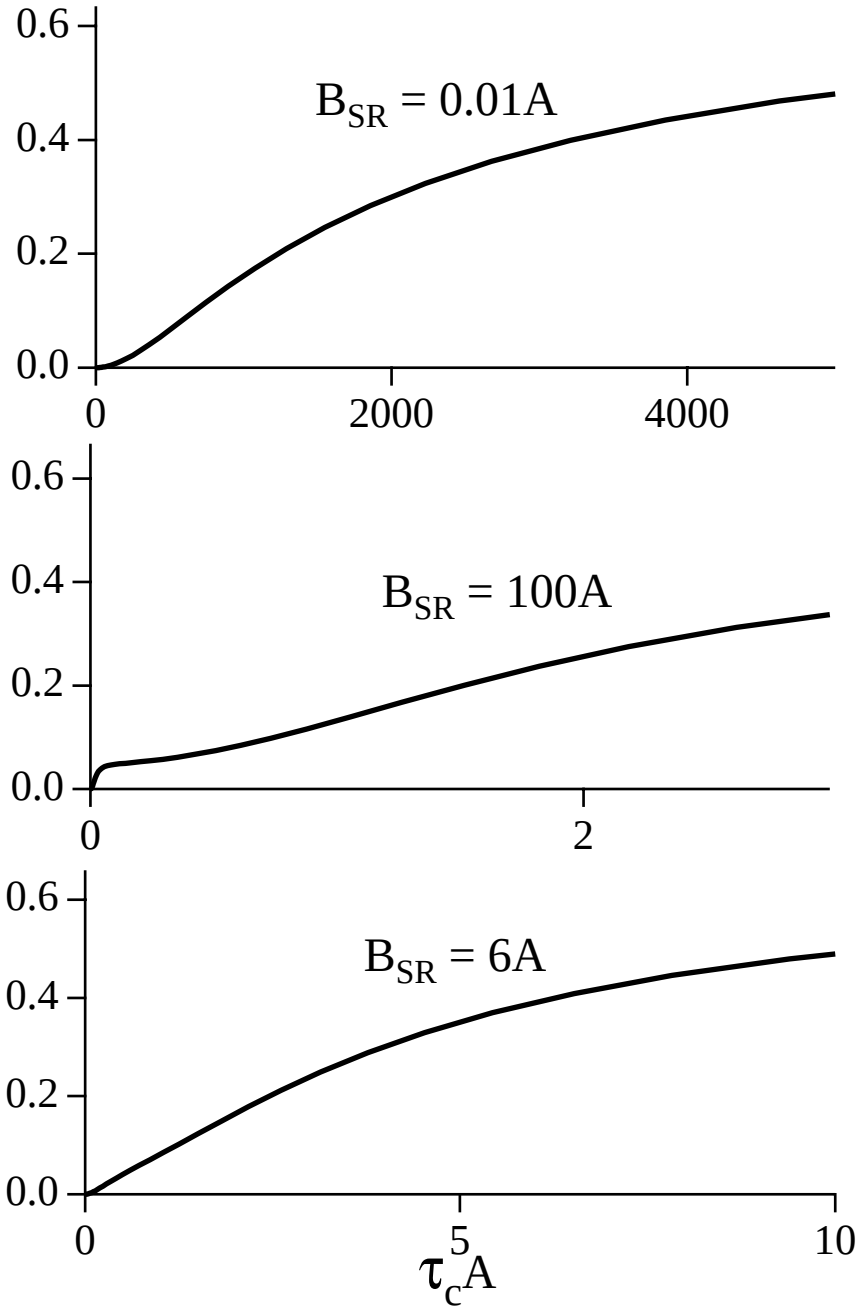

Figure 6.6: Calculated $F_J(\tau_c)$ for a $^{85,85}Rb_2$ triplet dimer. The qualitative shape of this function changes as the spin-axis coupling strength B_{SA} is changed relative to the hyperfine coupling strength A, but under no circumstances can it be made sufficiently flat to mimic the observed pressure independence of alkali-alkali relaxation.

observations for the following three reasons:

1 Although by carefully picking B_{SA} for each alkali pair I can make the predicted relaxation rate independent of pressure over about a factor of 10 (for the spin 3/2 K) to a factor of 50 (for the spin 7/2 Cs), this is far less than the observed pressure independence over three orders of magnitude for K.

2 In order to predict pressure independence, the interaction strength must be set such that the total predicted relaxation rate is about two orders of magnitude larger than the observed rate.

3 This pressure independence only appears in the absense of reorienting collisions ($\sigma_J \to 0$) because otherwise, the condition that $F_J \propto \tau_c$ near $F_J = \sigma_J/\sigma_b$ becomes impossible to meet. If σ_J/σ_b is about 10, as I have predicted in section 6.3, the relaxation rate can only be made pressure independent over about a factor of three in pressure, even with the most favorable choice of B_{SA}.

Therefore, I find that the inclusion of hyperfine structure does not allow for sufficient pressure independence to explain alkali-alkali relaxation.

6.6 Alternate Triplet Molecule Formation Mechanisms

The ultimate source of the pressure dependence in this model is that we are forced to rely on three-body processes to form and dissociate the triplet dimers. If dimers could form spontaneously, without the presence of the buffer gas, the predicted pressure dependence might be eliminated. In this section, I discuss two processes by which alkali atoms spontaneously associate into metastable molecular states, and show that the formation rates are not sufficient to explain alkali-alkali relaxation.

6.6.1 Tunneling Resonant Collisions

The triplet dimer potential curves as shown in fig. 5.1 are for a non-rotating molecule, and can support only bound states. However, with the addition of a $1/r^2$ centrifugal potential, the molecule develops a centrifugal barrier and can support quasi-bound

states of positive energy (see fig. 6.1). These states are referred to as quasi-bound (or resonances) because they may spontaneously dissociate into free atoms by tunneling through the centrifugal barrier.

The inverse process (spontaneous association) happens as well. This is an attractive candidate mechanism for alkali-alkali relaxation because it would match the nearly linear alkali dependence, third body independence, and might have a sufficiently long interaction time to explain the magnetic field dependence. Note that as the quasi-bound states approach the top of the centrifugal barrier, the resonances become increasingly broad and spontaneous association becomes essentially indistinguishable from the binary collisions addressed in chapter 5. Therefore, by calculating the expected relaxation rate in spontaneously associated molecules, I am recalculating the binary collision relaxation rate in the small region of phase space where quantum effects are important. A shown in section 6.6.3, the correct quantum treatment of these resonances makes a negligible change to the predicted relaxation rate. This justifies the semi-classical approach in chapter 5.

For each state of positive energy calculated in section 6.1, I determined the spontaneous dissociation rate $1/\tau_{tun}$. In accordance the theory of spontaneous decay well known in nuclear physics (see [Blatt], p. 401, for instance), a molecule in ro-vibrational state i decays at a rate

$$1/\tau_{tun,i} = \delta E_i/\hbar \tag{6.14}$$

where δE_i is the energy width of the resonance at energy E_i. The energy width is defined in terms of the asymptotic solutions to the Schrödinger equation $u(E_i \pm \delta E_i, r)_{r\to\infty} \sim \sin(kr + \phi(E_i \pm \delta E_i))$ such that

$$|\phi(E_i + \delta E_i) - \phi(E_i - \delta E_i)| = \pi/2. \tag{6.15}$$

I calculated the energy width numerically as follows:

1 For each angular momentum and $0 < E <$ the centrifugal barrier height, search for energies such that $u(E \pm \epsilon)$ changes sign in the tunneling region, but $u(E)$ does not, for some very small. ϵ. This is the center energy of a resonance.

2 Pick a small δE and integrate the Schrödinger equation outward, to a dis-

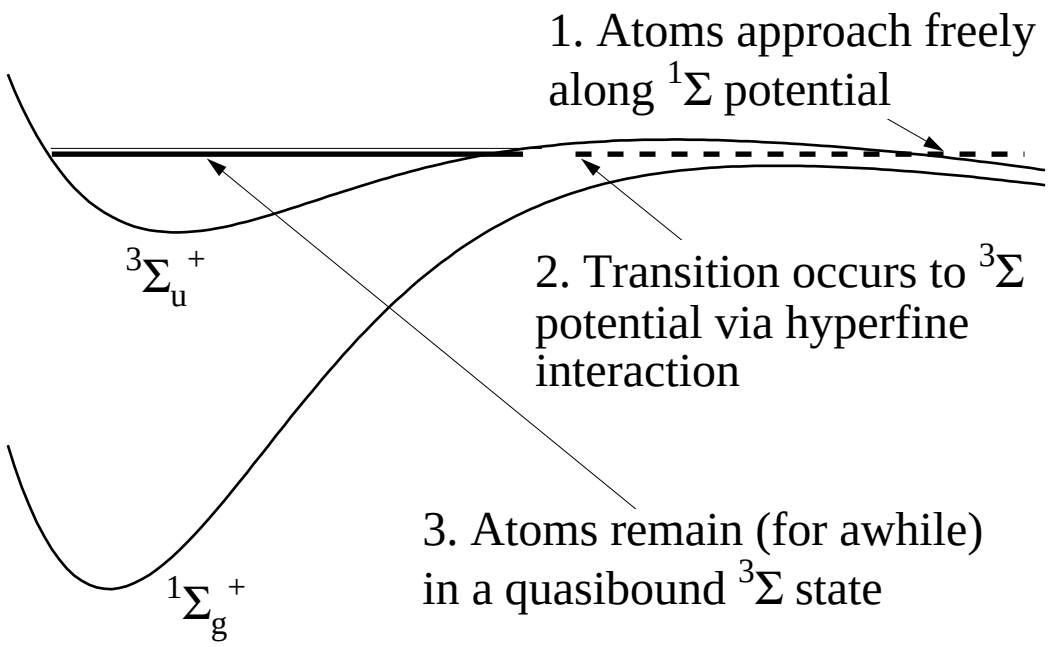

Figure 6.7: Schematic depiction of a Feshbach resonant collision

tance where the triplet potential is much smaller than E. By noting the positions of successive maxima, determine the phase shift $\phi(E \pm \delta E)$.

3 Keep adjusting δE and repeating step 2 until eq. 6.15 is met.

The resulting tunneling rates for the $^3K_2$ dimer states are summarized in fig. 6.8.

6.6.2 Feshbach Resonant Collisions

Since the singlet molecular potential is much deeper than the triplet potential, the centrifugal barrier for a given axis angular momentum is lower for a singlet molecular state. Therefore, another spontaneous dissociation/formation process can take place if the hyperfine interaction causes a transition between a quasibound triplet state and a free singlet at the same energy. I will refer to this mechanism as a Feshbach resonance. It is depicted schematically in fig. 6.7. Note that it has the same attractive characteristics for explaining alkali-alkali relaxation as the tunneling resonant collisions.

Dissociation via a Feshbach resonance is a bound→free process, so I have estimated the dissociation rate $1/\tau_{fesh}$ for each quasi-bound triplet molecular state using Fermi's Golden Rule. Thus, the transition rate from triplet molecular state $|1 m_S m_{I1} m_{I2} J m_J n\rangle$ to free singlet state $|0\ 0\ m_{I1'}\ m_{I2'}\ J\ m_J\ E\rangle$ is

$$1/\tau_{fesh} = \frac{2\pi}{\hbar}\int dE\, \langle 1 m_S m_{I1} m_{I2} J m_J n|H_{hyp}|0\,0\, m_{I1'}\, m_{I2'}\, J m_J E\rangle^2 g(E)\delta(E-E_n) \quad (6.16)$$

where $g(E)$ is the density of free singlet states with J, m_J at energy E and H_{hyp} is the free atom hyperfine Hamiltonian, $A_1\mathbf{I_1}\cdot\mathbf{S_1} + A_2\mathbf{I_2}\cdot\mathbf{S_2}$. In order to get the the normalization and $g(E)$, we can picture a system which has an infinite potential barrier at $r = R$. As $R \to \infty$, the sinusoidal oscillations of $u(r)$ at large r determine its normalization. So, $\int_0^R dr\ |u(r)|^2 \approx R/2$ and the correct normalization is such that the amplitude of large r oscillations is $\sqrt{2/R}$. To get $g(E)$, note that in order to fit one more half-wavelength into length R, we need to increase k by δk so that $kR + \pi = (k+\delta k)R$. This corresponds to an increase of the energy by $\delta E = h/R\sqrt{E/2\mu}$ yielding

$$g(E) = 1/\delta E = R/h\sqrt{2\mu/E}. \quad (6.17)$$

Now, to eliminate R, we change the normalization of the singlet state wavefunction so that the amplitude of oscillations at large r is 1. To keep everything the same, we divide $g(E)$ by $R/2$. This gives

$$1/\tau_{fesh} = 2\langle 1\ m_S\ m_{I1}\ m_{I2}|\frac{H_{hyp}}{\hbar}|0\ 0\ m_{I1'}\ m_{I2'}\rangle^2 \left(\int_0^\infty dr\ u^*_{J,n}(r)\ u_{J,E_n}(r)\right)^2 \sqrt{\frac{2\mu}{E}} \quad (6.18)$$

(the units of eq. 6.18 look odd because $u_{J,E_n}(r)$ is normalized such that $\int_0^\infty dr\ u^*u$ has units of $(distance)^{1/2}$).

We can now replace the the first matrix element by an average over initial and sum over final electron and nuclear spin projections

$$\frac{1}{3(2I_1+1)(2I_2+1)}\sum_{\substack{m_S,m_{I1},m_{I2}\\ m'_{I1},m'_{I2}}} \langle 1\ m_S\ m_{I1}\ m_{I2}|\frac{H_{hyp}}{\hbar}|0\ 0\ m_{I1'}\ m_{I2'}\rangle^2$$
$$= \frac{1}{12\hbar^2}\left(A_1^2 I_1(I_1+1) + A_2^2(I_2+1)\right) \quad (6.19)$$

to arrive at the total transition rate

$$1/\tau_{fesh} = \frac{A_1^2 I_1(I_1+1) + A_2^2 I_2(I_2+1)}{6\hbar^2}\sqrt{\frac{2\mu}{E}}\left(\int_0^\infty dr\; u^*_{J,n}(r)\; u_{J,E_n}(r)\right)^2 \tag{6.20}$$

or for a homonuclear molecule, with spin I and ground state hyperfine splitting $\Delta\nu$,

$$1/\tau_{fesh} = \frac{I(I+1)}{3}\sqrt{\frac{2\mu}{E}}\left(\frac{4\pi\Delta\nu}{2I+1}\int_0^\infty dr\; u^*_{J,n}(r)\; u_{J,E_n}(r)\right)^2 \tag{6.21}$$

with $\int dr\,|u_{J,n}(r)|^2 = 1$ and $u_{J,E_n}(r) \to \cos(kr+\phi)$ as $r \to \infty$. I performed the integral in eq. 6.21 numerically after calculating the singlet and triplet spatial wavefunctions numerically to arrive at a dissociation rate for each triplet molecular state via Feshbach resonant dissociation. Figure 6.8 shows the calculated dissociation rates for selected states of the K_2 triplet dimer.

6.6.3 Relaxation Rate in Spontaneously Associated Dimers

In order for spontaneously associated triplet states to explain alkali-alkali relaxation, they have to live sufficiently long to explain the observed magnetic field dependence. As discussed in section 4.4, this puts a lower limit of 300 ps on the lifetime of states we need consider. On the other hand, the states can not spontaneously dissociate too slowly, or three-body processes would become the dominant dissociation and formation mechanism, and the desired pressure independence would be lost. Thus, we can set an upper limit of about 1 ns on the lifetime of states that might contribute to alkali-alkali relaxation based on a conservative estimate of the three-body breakup rate at 10 atmospheres of buffer gas pressure. The two limits exclude all but about 1 percent of the spontaneously dissociating dimer states. In addition, those that do meet our criteria are very near the top of the centrifugal barrier and, as can be seen from fig. 6.3, have a very small spin-axis interaction. Thus, it is difficult to see how there can be significant relaxation in states primarily formed through spontaneous association without without it being dwarfed by the relaxation in stable dimer states formed by three-body processes.

We can make this argument more quantitative by including the spontaneous disso-

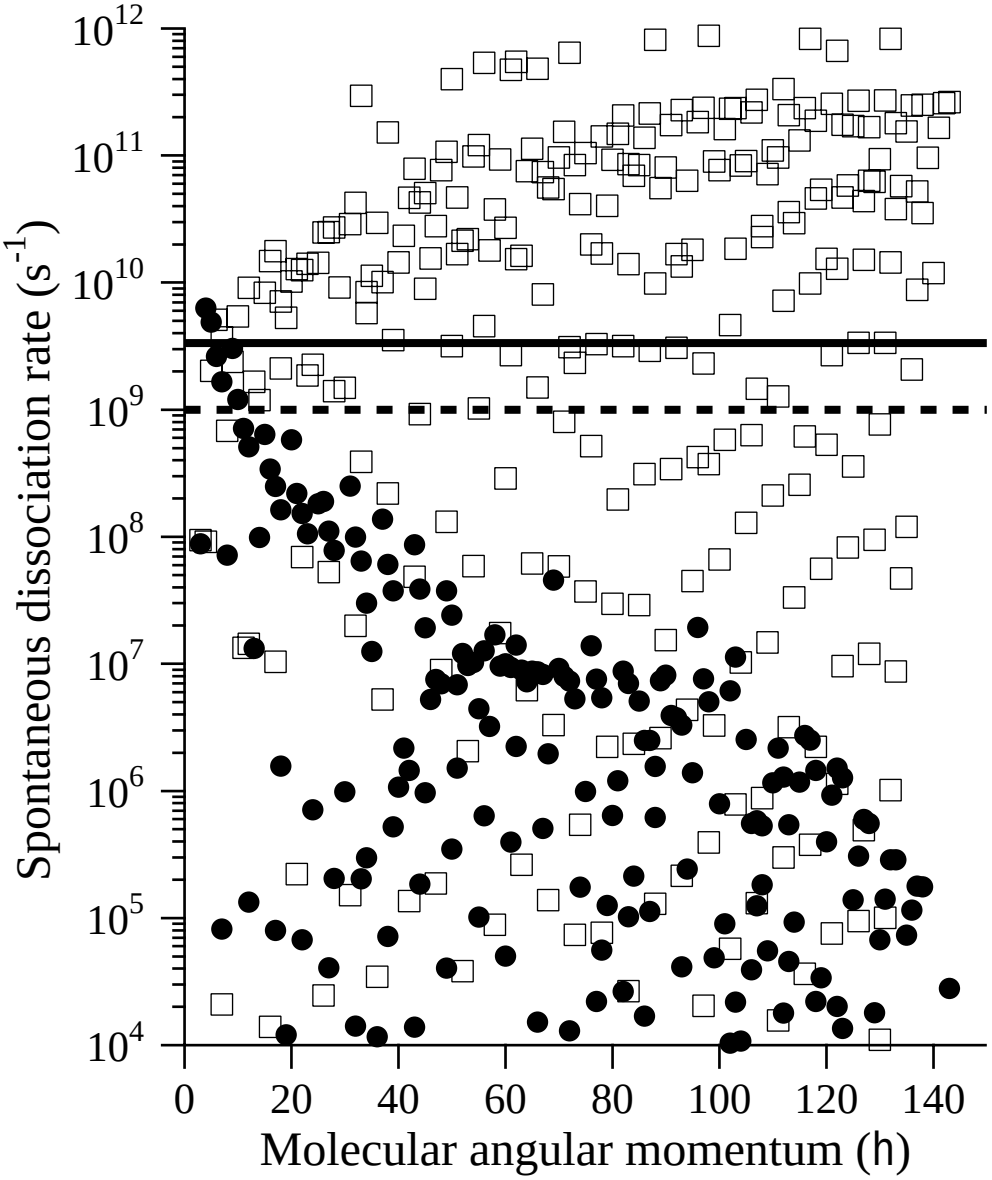

Figure 6.8: Calculated molecular dissociation rates for $^3K_2$ states due to tunneling (unfilled squares) and Feshbach resonances (filled circles). As discussed in chapter 4, the magnetic field width sets an upper limit on the dissociation rate of states that are to contribute to alkali-alkali relaxation (solid line) and we can arrive at an lower limit by requiring that spontaneous association dominate three-body formation (the dotted line shows the expected three-body breakup rate at 10 atmospheres of He). This leaves too few states to explain the alkali-alkali rate coefficients.

ciation rate as a breakup mechanism in eq. 6.8– that is,

$$\begin{aligned} 1/\tau_{d,i} &= [B]\langle \sigma_b v_{A_2 \cdot B} \rangle + 1/\tau_{fesh,i} + 1/\tau_{tun,i} \\ \frac{1}{\tau_{F,i}} &= 2\ k_{chem,i}[A]/\tau_{d,i} \\ \Gamma_{trip} &= \Sigma_i \frac{1}{\tau_{F,i}} \frac{(\tau_J + \tau_d) F_{J,i}}{\tau_{J,i} + \tau_{d,i} F_{J,i}} \end{aligned} \tag{6.22}$$

in which τ_d is the total dissociation rate of state i due to all three breakup processes. I have recalculated the predicted relaxation rates shown in fig. 6.5 and find that the difference made by including spontaneous association processes below the percent level at all buffer gas pressures above a Torr and therefore do not help explain the pressure independence of alkali-alkali relaxation.

Chapter 7

Model of Relaxation in Alkali Trimers

In this chapter, I assess the likelihood that alkali-alkali relaxation is taking place in alkali trimers. The alkali trimer potential energy surfaces are not particularly well known and, to the best of my knowledge, no calculations of spin-dependent interactions in trimers have ever been undertaken. Nonetheless, it is possible to reach some general conclusions based on statistical arguments and our knowledge of short-time evolution in quantum mechanics.

Sections 7.1.1-2 explain a simple model of electron spin coupling in alkali trimers and give an estimate of the trimer potential energy surface. I refer to and discuss a more sophisticaed calculation of the K_3 potential energy surface by Martins, *et al.* in section 7.1.3. I use this surface to estimate the equilibrium density of stable K_3 in section 7.2. I then explain in section 7.3 why I believe that no model of relaxation in stable trimers can be made to match the experimentally observed alkali-alkali relaxation rates.

The situation looks more hopeful for relaxation in metastable trimers, however. I discuss this possible explanation in section 7.4, including a description of a classical-trajectory simulation of metastable trimer dynamics in section 7.4.1 and an estimate of the spin-dependent coupling needed to match the experimentally observed K-K relaxation rate.

Considerable experimental and theoretical effort has been devoted to understanding alkali trimers ([Frederico99, Woste96, Martins83, Kornath98, Eckel93] and many others). As with the alkali dimers, Na has been studied most carefully, but only the low lying ro-vibrational states have been classified and even the Na_3 binding energy is largely unknown. Information is scarse or nonexistant for the heavier alkalis. In order

to estimate relaxation in trimers, I have had to make considerable simplifications and approximations. Therefore, this analysis is much more speculative than that of previous chapters.

7.1 Spin Coupling in Alkali Trimers

7.1.1 Review of Alkal Dimer Eigenstates

Being the simplest molecules, alkali dimers are discussed in nearly all introductory molecular physics texts (see, for example, [Woodgate]). I will quickly review the results to introduce formalism necessary for handling trimers.

Consider two alkali atoms with nuclei at $\vec{r_a}$ and $\vec{r_b}$. The spatial wavefunctions of their (ground state) valence electrons are $u(\vec{r}-\vec{r_a})$ and $u(\vec{r}-\vec{r_b})$ which I will abbreviate as u_a and u_b. The electrons are indistinguishable and therefore not necessarily tied to a particular atom, so I will refer to them as electrons 1 and 2.

The Hamiltonian that describes the atoms is the sum of the free atomic Hamiltonians, H_0, and the interaction Hamiltonian H_I which describes the repulsion between electrons and the attraction between the electrons and the other nuclei.

As the atoms approach each other, the eigenstates are the singlet and triplet

$$\begin{aligned} |\psi_s\rangle &= \frac{1}{2}(|u_a u_b\rangle + |u_b u_a\rangle) \times (|\uparrow\downarrow\rangle - |\downarrow\uparrow\rangle) \\ |\psi_t\rangle &= \frac{1}{2}(|u_a u_b\rangle - |u_b u_a\rangle) \times \{\sqrt{2}|\uparrow\uparrow\rangle, (|\uparrow\downarrow\rangle + |\downarrow\uparrow\rangle), \text{ or } \sqrt{2}|\downarrow\downarrow\rangle\} \end{aligned} \tag{7.1}$$

where the state of electron 1 is first and electron 2 is second in each ket.

If we define the direct and exchange integrals as

$$\begin{aligned} \text{direct}: \quad J &= \langle u_a u_b|\mathrm{H}_I|u_a u_b\rangle \\ \text{exchange}: \quad K &= \langle u_a u_b|\mathrm{H}_I|u_b u_a\rangle \end{aligned} \tag{7.2}$$

we find that the eigenenergies of H_I are

$$\begin{aligned} \langle\psi_s|\mathrm{H}_I|\psi_s\rangle &= J + K \\ \langle\psi_t|\mathrm{H}_I|\psi_t\rangle &= J - K \end{aligned} \tag{7.3}$$

The trimer eigenenergies depend on the same integrals, so it is useful to write them in terms of the experimentally measured singlet and triplet potentials V_s and V_t:

$$\begin{aligned} J &= \langle u_a u_b | \mathrm{H}_I | u_a u_b \rangle = (V_s + V_t)/2 \\ K &= \langle u_a u_b | \mathrm{H}_I | u_b u_a \rangle = (V_s - V_t)/2 \end{aligned} \tag{7.4}$$

7.1.2 Simple Approximation to Alkali Trimer Surfaces

Three separated alkali atoms have eight possible combinations of valence electron spin states. In order for the coupled spin representation to have the same number of states, the electrons must couple into a spin 3/2 manifold and two spin 1/2 manifolds. In the absence of magnetic field, each of these manifolds is degenerate, so we can find their energies by diagonalizing H_I in the space of the three states with projection 1/2.

The most general projection 1/2 state is a linear combination of states in which one electron is on each atom, two electrons have spin up and the third has spin down. Not all such states are independent, however, because the total electron wavefunction must be antisymmetric with respect to exchange of two electron labels. To enforce this, I introduce the permutation operator P such that P acting on a state gives the normalized sum of all permutations of electron label with appropriate signs. For instance,

$$\begin{aligned} P(|u_a\uparrow\, u_b\uparrow\, u_c\downarrow\rangle) = \frac{1}{\sqrt{6}}[&|u_a\uparrow\, u_b\uparrow\, u_c\downarrow\rangle - |u_b\uparrow\, u_a\uparrow\, u_c\downarrow\rangle + |u_b\uparrow\, u_c\downarrow\, u_a\uparrow\rangle - \\ &|u_c\downarrow\, u_b\uparrow\, u_a\uparrow\rangle + |u_c\downarrow\, u_a\uparrow\, u_b\uparrow\rangle - |u_a\uparrow\, u_c\downarrow\, u_b\uparrow\rangle] \end{aligned} \tag{7.5}$$

where as in the dimer states, $|u_a\uparrow\, u_b\uparrow\, u_c\downarrow\rangle$ has electron 1 in state u_a and spin up, electron 2 in state u_b and spin up and electron 3 in state u_c and spin down.

The most general projection 1/2 state that obeys the Pauli exclusion principle is therefore a linear combination of $P(|u_a\uparrow\, u_b\uparrow\, u_c\downarrow\rangle)$, $P(|u_a\uparrow\, u_b\downarrow\, u_c\uparrow\rangle)$, and $P(|u_a\downarrow\, u_b\uparrow\, u_c\uparrow\rangle)$. As a starting point for diagonalizing H_I, I somewhat arbitrarily choose the orthogonal states

$$\begin{aligned} |\psi_0\rangle &= \sqrt{\frac{1}{3}}[P(|u_a\uparrow\, u_b\uparrow\, u_c\downarrow\rangle) + P(|u_a\uparrow\, u_b\downarrow\, u_c\uparrow\rangle) + P(|u_a\downarrow\, u_b\uparrow\, u_c\uparrow\rangle)] \\ |\psi_1\rangle &= \sqrt{\frac{1}{6}}[P(|u_a\uparrow\, u_b\uparrow\, u_c\downarrow\rangle) + P(|u_a\uparrow\, u_b\downarrow\, u_c\uparrow\rangle)] + \sqrt{\frac{2}{3}}P(|u_a\downarrow\, u_b\uparrow\, u_c\uparrow\rangle) \end{aligned}$$

$$|\psi_2\rangle \;=\; \sqrt{\frac{1}{2}}[P(|u_a\uparrow\, u_b\uparrow\, u_c\downarrow\rangle) - P(|u_a\uparrow\, u_b\downarrow\, u_c\uparrow\rangle)]. \tag{7.6}$$

Note that the $|\psi_0\rangle$ factors into $P(|u_a u_b u_c\rangle)\ \times\ \mathrm{P}(|\uparrow\uparrow\downarrow\rangle)$, which gives it a pure triplet character, but the other two states have mixed triplet and singlet character.

As in the dimer case above, we may write the matrix elements of H_I in this space in terms of the exchange integrals J and K, although in this case the exchange integral acquires subscripts to identify the wavefunctions being exchanged. There is also a multiple-exchange integral of the form $\langle u_a u_b u_c|\mathrm{H}_I|u_b u_c u_a\rangle$ which is assumed to be very small compared to the direct and single-exchange integrals, and which I will therefore ignore.

$$H_I = J + \begin{pmatrix} -K_{ab}-K_{bc}-K_{ac} & 0 & 0 \\ 0 & \frac{1}{2}(K_{ab}+Kac) - K_{bc} & \frac{\sqrt{3}}{2}(K_{ac}-K_{ab}) \\ 0 & \frac{\sqrt{3}}{2}(K_{ac}-K_{ab}) & -\frac{1}{2}(K_{ab}+K_{ac}) + K_{bc} \end{pmatrix} \tag{7.7}$$

This shows that $|\psi_0\rangle$ is an eigenstate of H_I (which is true even if the multiple exchange terms are included). Note also that applying the spin raising operator to $|\psi_0\rangle$ gives $P(|u_a u_b u_c\rangle)\ \times\ |\uparrow\uparrow\uparrow\rangle$ which makes it part of the spin 3/2 manifold. Diagonalizing H_I with respect to the spin 1/2 states gives eigenvalues

$$E_\pm = J \pm \sqrt{\frac{1}{2}}[(K_{ab}-K_{ac})^2 + (K_{ab}-K_{bc})^2 + (K_{ac}-K_{bc})^2] \tag{7.8}$$

and the corresponding eigevectors

$$\begin{aligned} |\epsilon_+\rangle &= cos(\alpha)|1\rangle + sin(\alpha)|2\rangle \\ |\epsilon_-\rangle &= sin(\alpha)|1\rangle - cos(\alpha)|2\rangle \end{aligned} \tag{7.9}$$

with the mixing angle α given by

$$tan(2\alpha) = \frac{\sqrt{3}(K_{ac}-K_{ab})}{K_{ab}+K_{ac}-2K_{bc}}. \tag{7.10}$$

7.1.3 More Sophisticated Trimer Surfaces

The above calculation gives us a fairly good approximation to the trimer potential energy surfaces (as compared to the more sophisticated calculation referenced in this section). In addition, eq. 7.8 suggests that only the lowest lying spin 1/2 manifold is likely to be more deeply bound than the singlet molecule. Thus, all stable trimers are almost certainly in this spin 1/2 manifold, and any relaxation processes are limited to transitions between its Zeeman levels.

However, the approximate calculation does not take into account valence electron wavefunction distortions or core polarization effects, except to the extent that they determine the dimer potentials. I have therefore used the published potential energy surface of ref. [Martins83] for K_3. This calculation uses pseudopotentials, chosen to reproduce alkali ion energies, to describe the core electrons. The effect of correlation between valence electrons is treated using the local spin density approximation (see references in ref. [Martins83]). The potentials are parameterized in terms of the singlet dimer potential, which I have scaled by about 5 percent to match the recent experimental binding energy determination by [Amiot91].

At present, no published surfaces exist for Rb_3 or Cs_3.

Comparison of the two approaches show the the simple calculation of section 7.1.2 underestimates the trimer binding energy by about 10 percent. This is enough error to significantly change the predicted equilibrium trimer density, and the effects of core polarization almost certainly get more pronounced for Rb and Cs. Because of the uncertainty of calculations for the heavier alkalis, I have limited my estimates to K_3.

7.2 Stable Trimer Density

Ideally, we would calculate the chemical equilibrium coefficient for K trimers by counting eigenstates as I have done for the dimers (sections 3.1 and 6.1). Given the difficulty of finding three-body eigenstates, however, I have used a classical phase space derivation instead. The trimer potential surface is sufficiently floppy that I do not expect this approximation to introduce significant error.

Using standard statistical arguments (see [Reif], for example), we may write the trimer chemical equilibrium coefficient k_{chem} as a ratio of classical atomic (Z_A) and

trimer (Z_{A_3}) partition functions

$$[A_3] = k_{chem}[A]^3, \qquad k_{chem} = \frac{Z_{A_3}}{Z_A} \tag{7.11}$$

with

$$\begin{aligned} Z_A &= 2\frac{V}{h^3}\int_0^\infty 4\pi p^2 dp\, e^{-p^2/2mk_BT} \\ Z_{A_3} &= 2\frac{1}{6}\frac{V}{h^9}\int d^3r_1 \int d^3r_2 \int_0^{p_{max}} 4\pi p_1^2\, dp_1 \int_0^{\sqrt{p_{max}^2-p_1^2}} 4\pi p_2^2\, dp_2 \times \\ &\qquad \int_0^{\sqrt{p_{max}^2-p_1^2-p_2^2}} 4\pi p_3^2\, dp_2 e^{-(p1^2+p_2^2+p_3^2)/2mk_BT} \end{aligned} \tag{7.12}$$

where $\vec{\mathbf{r}}_\mathbf{1}$ and $\vec{\mathbf{r}}_\mathbf{2}$ are the positions of atoms 1 and 2 relative to atom 3, and $p_{max}^2/2m + V(\vec{\mathbf{r}}_1, \vec{\mathbf{r}}_2) = E_{max}$ is the maximum bound trimer energy. I have introduced E_{max} as a parameter because it is not clear which states are bound and which will dissociate into a singlet molecule and an atom, but we can get a lower bound on k_{chem} by taking E_{max} equal to the singlet dimer binding energy. The factors of 2 in front of each partition function take into account spin degeneracy, and the 1/6 multiplying Z_{A_3} reflects the 6-fold permutation symmetry of a trimer with respect to atom label.

Most of the integrals of eq. 7.12 can be done analytically, yielding

$$\begin{aligned} k_{chem} &= \frac{16\pi^{3/2}}{415}\int_0^\infty r_1^2 dr_1 \int_0^\infty r_2^2 dr_2 \int_{-1}^1 d(\cos\theta) \times \\ &\qquad e^{-V(r1,r2,\theta)/k_BT}\gamma(9/2, \frac{E_{max}-V(r1,r2,\theta)}{k_BT}) \end{aligned} \tag{7.13}$$

in which $\gamma()$ is the incomplete gamma function.

I have performed the spatial integrals of eq. 7.13 numerically using the (scaled) potential of ref. [Martins83]. Figure 7.1 shows the resulting chemical equilibrium coefficient for K_3 and the fraction of K atoms in stable trimers. Although absolute density of trimers is typically small (about 10^9-10^{10}cm^{-3}), there are more trimers than there are triplet dimers. In addition, if we assume that the cross-section for atom-trimer exchange is similar to the cross-section for atom-dimer exchange (section 3.4-5), trimer densities are large enough for each alkali atom to pass through several to tens of trimers per second. Thus, trimers are numerous enough to warrent further examination.

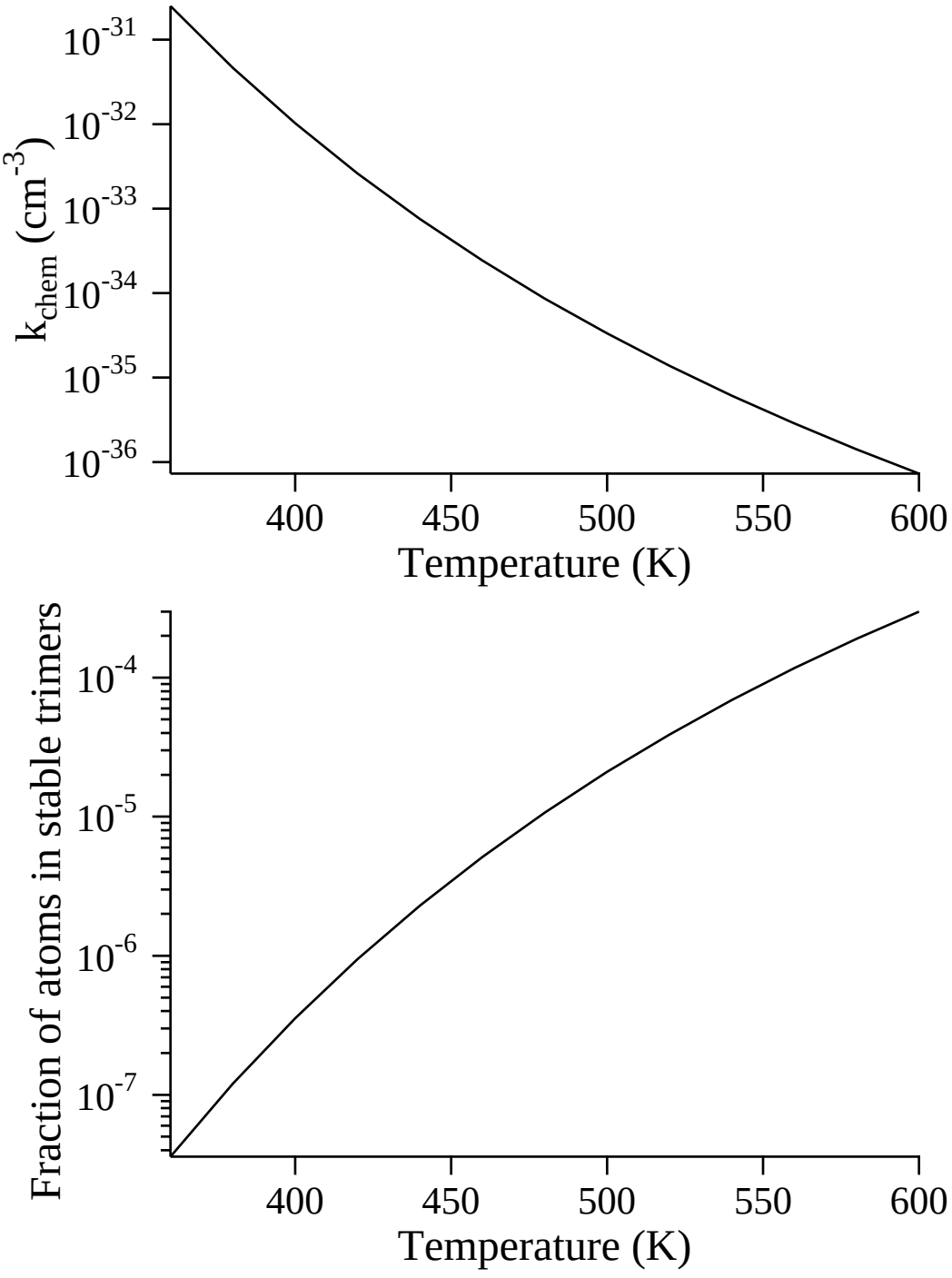

Figure 7.1: Lower limit on the K_3 chemical equilibrium coefficient and the fraction of K atoms in stable trimers, as a function of temperature.

7.3 Relaxation in Stable K_3

The interaction causing relaxation in a trimer would presumably be a spin-rotation coupling like that discussed in section 3.2. However, since the atomic wavefunctions (or classically, the atomic motions) are so complicated, it is quite difficult to estimate the effective interaction for a given bound trimer state, or even to classify the states in the first place. Nonetheless, it is possible to make some general observations that are difficult to reconcile with the notion that alkali-alkali relaxation is taking place in stable alkali trimers.

We can use the chemical equilibrium coefficients calculated in sections 7.2 and 3.1 to predict how the relaxation rate in trimers depends on alkali density and buffer gas pressure. Although we do not know the strength or form of the interaction causing relaxation, it must couple an atomic spin to trimer angular momentum because there is nowhere else that polarization can be lost. In addition, I will assume that, although the trimer eigenstates can not be classified in the straightforward manner used for dimers, they are discrete, so the transition rate for small time τ is proportional to τ^2.

If we accept those two core assumptions, we can estimate relaxation rates in trimers by classifying all possible relaxation models as follows:

1 The dominant mode of entry into a trimer is one of the following

$$\begin{aligned}
&\text{I.} && K + K + K + B \rightarrow K_3 + B \\
&\text{II.} && K + K_2 + B \rightarrow K_3 + B \\
&\text{III.} && K + K_3 \rightarrow K + K_3 \quad \text{(chemical exchange)} \\
&\textit{IV.} && K_2 + K_2 \rightarrow K + K_3
\end{aligned}$$

All other formation mechanism involve at least five bodies and are therefore greatly suppressed.

2 Once an atom becomes part of a trimer, it relaxes governed by an interaction that has one of the following characteristics

strong. If the interaction causing relaxation in trimers is strong, the spins relax to a constant polarization (possibly zero) during a typical dwell time

	Formation Mechanism	strong	weak, A	weak, B
I.	$K + K + K + B \rightarrow K_3 + B$	$[K]^2[B]$	$[B]$	$[K]^2/[B]$
II.	$K_2 + K + B \rightarrow K_3 + B$	$[K_2][B]$	$[K_2][B]/[K]^2$	$[K_2]/[B]$
III.	$K_3 + K \rightarrow K_3 + K$	$[K_3]$	$[K_3]/[K]^2$	$[K_3]/[B]^2$
IV.	$K_2 + K_2 \rightarrow K_3 + K$	$[K_2]^2/[K]$	$[K_2]^2/[K]^3$	$[K_2]^2/[K]/[B]^2$

Table 7.1: Predicted potassium ($[K]$) and buffer gas ($[B]$) density dependence of relaxation in stable trimers.

in a trimer. The relaxation rate is then simply proportional to the rate that an alkali atom enters trimers.

weak, A. If the interaction causing relaxation is weak, relaxation is not complete during the typical dwell time in a trimer. If, further, the end of coherent relaxation is caused by an interaction with an alkali atom, the relaxation rate should vary as the ratio of the rate that an alkali atom enters trimers to the square of the alkali density.

weak, B. Similarly, if the interaction causing relaxation is weak and coherent relaxation is brought to an end by an interaction with the buffer gas, the relaxation rate should vary as the ratio of the rate that an alkali atom enters trimers to the square of the buffer gas density.

I have listed all of the possible combinations in table 7.1, and the predicted dependences of the relaxation rate in each case. Note that if the relaxation rate is to be independent of buffer gas pressure, the dominant route for alkali atoms to enter trimers must be either III or IV. Additionally, the relaxation must either be strong, or immune to decoherence from collisions with the buffer gas.

Next, we can examine the [K] dependence of each table entry more closely. Because the chemical equilibrium coefficients are strongly temperature dependent, it is convenient to use the following rules of thumb; for temperatures near 500 K,

$$\begin{aligned} [K_2] &= {}^1k_{chem}[K]^2 \approx [K]^{1.33} \\ [K_3] &= k_{chem}[K]^3 \approx [K]^{1.80}. \end{aligned} \tag{7.14}$$

Using these approximate relationships, we see that the relaxation rate's nearly linear dependence on alkali density can be explained only if the dominant trimer formation

mechanism is II.

It therefore seems that there is no model of relaxation in alkali trimers that is consistent with all of the observations of alkali-alkali relaxation. Of course, this conclusion is based on relatively poor knowledge of the trimer potential energy surface and eigenstates. Thus, if the energy surface turns out to be significantly in error, or if trimer dynamics are sufficiently exotic to invalidate one of the core assumptions made above, this notion may have to be revisited. In principle, it is also possible several different trimer formation mechanisms conspire to mimic pressure independence and linear alkali density dependence, although given the range of alkali species, densities and buffer gas pressure covered experimentally, this seems highly unlikely.

7.4 Relaxation in Metastable Trimers

Just as metastable triplet dimers can form without the presence of a third body (section 6.6), metastable trimers can form without the presence of a fourth body. The two processes are quite different, however. While we need quantum mechanics to understand metastability in dimers, it can be thought of classically in a trimer as follows; during a collision between a singlet dimer and an atom, the incident atom may give up enough energy to the dimer's ro-vibrational motion that it is energetically unable to leave. It will then return and collide again until, by chance, the dimer is returned to a low enough energy state to allow the atom to escape. Alternatively, the initially free atom may capture one of the dimer's atoms into a sufficiently low energy molecular state to allow the other atom to escape. This is a chemical exchange collision as measured in the context of singlet molecule relaxation (chapter 3).

7.4.1 Classical Trajectory Simulation

To assess the possibility of relaxation in metastable trimers, I used the classical trajectory simulation described in appendix D. This allowed me to get a rough idea of the frequency of metastable trimer formation and the distribution of dwell times once a trimer is formed. The results for K-^{1}K$_2$ collisions can be summarized as follows:

1 The cross-section for K - ^{1}K$_2$ exchange collisions (σ_{ex}) is about $180\mathring{A}^2$ at 500 K.

2 The average amount of time that the atoms spend within a $10\mathring{A}$ diameter circle (the dwell time) is about 100 ps.

3 Long duration collisions are suprisingly common– the distribution of dwell times τ_{dwell} fits reasonably well to

$$P(\tau_{dwell}) \propto e^{-20[(\tau_{dwell}/ps)+10]^{1/15}}. \tag{7.15}$$

Since they are based on limited knowledge of the potential energy surface and a classical approach, the above observations are certainly tentative. Nonetheless, they suggest that the fraction of time that each atom spends in a metastable trimer at 500 K is $3\ {}^1k_{chem}[K]^2\langle\sigma_{ex}v_{K\cdot K_2}\rangle\langle\tau_{dwell}\rangle \approx 5\times10^{-6}$, which is comparable to the fraction of time it spends in a stable trimer. In addition, each atom passes through thousands of metastable trimers per second. This is much faster than the corresponding formation rate for stable trimers and, depending on the details of the relaxing interaction, may lead to a correspondingly larger relaxation rate.

We would expect the relaxation rate in metastable trimers to be independent of buffer gas pressure and to scale roughly as the density of singlet dimers (possibly modified for a temperature-dependent chemical exchange cross-section and dwell time). This is sufficiently close to the measured alkali-alkali relaxation scaling (see fig. 4.11) to make metastable trimers a strong candidate explanation.

7.4.2 Tentative Relaxation Rate Estimates

I have made further tentative estimates of this relaxation process by postulating a spin-rotation interaction in metastable trimers of the form

$$V_{SR,trimer} = \hbar\Omega_{trimer}\mathbf{S}\cdot\mathbf{J} \tag{7.16}$$

where $\mathbf{J}$ is the trimer rotational angular momentum and $\mathbf{S}$ is the total electron spin coupled into a spin 1/2 manifold. I have postulated this form because it the simplest spin-rotation coupling possible, and other interactions, such as the rank 2 $\mathbf{S}(3\hat{\mathbf{J}}\hat{\mathbf{J}}-1)\mathbf{S}$, do not cause relaxation in a spin 1/2 manifold. Spin-rotation couplings of this type are not uncommon (see refs. [Huber80, VanEsbroeck85], for instance), but I do not know

how large it would be in an alkali trimer.

Nonetheless, I have tried several values of Ω_{trimer} and calculated the implied relaxation rate in metastable trimers for each by diagonalizing the interaction Hamiltonian

$$H_I = V_{SR,trimer} + \frac{A}{3}(\mathbf{I}_1 + \mathbf{I}_2 + \mathbf{I}_3) \cdot \mathbf{S} + g_S \mu_B B/\hbar S_z \tag{7.17}$$

numerically (as described in appendix C). I find that by choosing $\Omega_{trimer} \approx 2\pi(3 \text{ MHz})$, the predicted zero field relaxation rate is in good agreement with the measured alkali-alkali relaxation rate. Figure 7.2 shows the predicted relaxation rate in metastable K_3 trimers at 500 K ($[K] = 4.6\times10^{14}\text{cm}^{-3}$) as a function of magnetic field. For comparison, the figure also includes measured alkali-alkali relaxation rate at the same temperature. Note that the predicted magnetic decoupling for small fields is similar to that observed for alkali-alkali relaxation, although the partial decoupling is not very well reproduced. It is not yet clear whether this discrepancy is due the approximate nature of this model or is a fundamental problem with all models of relaxation in metastable trimers, but it certainly premature to identify this mechanism as the source of alkali-alkali relaxation. Nonetheless, I believe it to be a plausible explanation that should be revisited when more about the heavy alkali trimers is known.

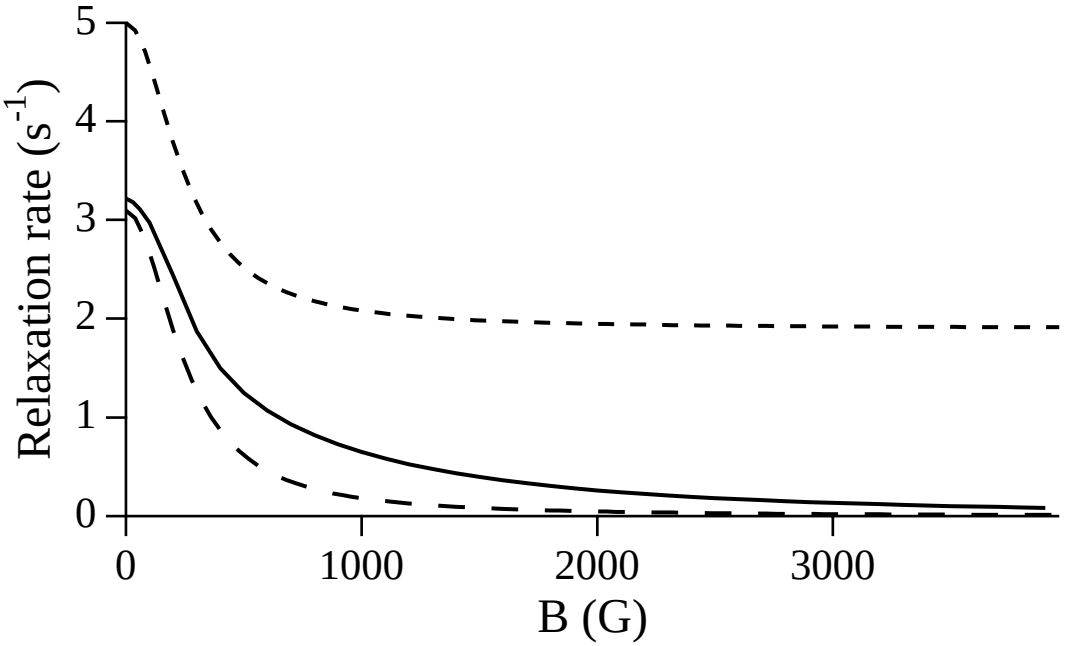

Figure 7.2: Predicted relaxation rate (solid line) in metastable K_3 complexes as a function of magnetic field B at 500 K. For this calculation, I assume that the electron spin in K_3 is relaxed by the interaction $V_{SR,trimer} = \hbar\Omega_{trimer}\mathbf{S}\cdot\mathbf{J}$ with $\Omega_{trimer} = 2\pi(3$ MHz). The dashed lines represent the measured alkali-alkali relaxation (short dashes) and the field-dependent part of alkali-alkali relaxation (long dashes) under identical cell conditions for comparison.

Chapter 8

Summary and Future Outlook

In this dissertation, I have described a series of experimental and theoretical studies directed toward the understanding of spin-relaxation mechanisms in an alkali vapor. This final chapter summarizes the progress we have made, suggests an immediate application of this work, and explores possible directions for further research.

8.1 Summary

I have shown that relaxation of a polarized sample of ground-state alkali atoms arises from at least four different mechanisms. Two of these, relaxation on the cell walls and relaxation through alkali-buffer gas collisions, appear to be fairly well understood. I have made some new measurements of alkali-buffer gas relaxation cross-sections, in particular at high temperature, but the work presented in this here is entirely consistent with existing theories.

The third mechanism, relaxation in alkali singlet dimers, had not been directly measured before, although its existence could certainly have been guessed based on previous measurements of the electric quadrupole interaction. I have demonstrated that this mechanism becomes quite important at low buffer gas pressure– in fact it is larger than might have been supposed from existing data. This suggests that the quadrupole interaction depends strongly on the molecular ro-vibrational state and is larger than had previously been thought. In addition, I have shown how we can use measurements of relaxation in singlet dimers to learn about the dynamics of atom-dimer

chemical exchange collisions and dimer reorientation in the vapor.

The final relaxation mechanism, alkali-alkali relaxation, does not yet have a complete explanation. Alkali-alkali relaxation was previously thought to occur in short-duration binary alkali collisions, but I have shown that it is largely decoupled by a $\sim kG$ magnetic field and explained why this observation is inconsistent with the previously held belief. In subsequent chapters, I have demonstrated why it appears to be impossible to explain alkali-alkali relaxation with a model based on relaxation in alkali triplet dimers or stable alkali trimers. Finally, I have put forth the tentative suggestion that a spin-rotation interaction in metastable trimers formed during atom-singlet dimer collisions may be the relaxation mechanism.

8.2 Implications

Even lacking a consistent explanation for the magnetic decoupling of alkali-alkali relaxation, this discovery may have important implications for the production of polarized noble gases and their subsequent use in MRI, spin-polarized targets, and other applications. Since alkali-alkali relaxation can be mostly eliminated, we estimate that the ^{3}He production rate in a typical Spin-Exchange Optical Pumping apparatus can be increased by at least a factor of two simply by putting the optical pumping cell in a few kG magnet. Hopefully, this will help bring the production cost of polarized gases down and make them more readily available for their many scientific and medical applications.

8.3 Continuations of This Work

The obvious direction for furture research is toward a more thorough understanding of alkali-alkali relaxation. Unfortunately, it is not as clear how to design an experiment that will get us there. We are currently exploring a few remaining options but, having varied the magnetic field, alkali density and buffer gas over all of the easily accessible values, future experimental work will almost certainly require a substantial redesign of the apparatus. Below, I discuss two ideas that are currently being pursued, and I have listed a few possible areas of future work as well.

1 We are currently pursuing studies of relaxation at high polarization fraction.

If, as suggested in chapter 7, relaxation is taking place during alkali atom-singlet dimer collisions, we should see a lower relaxation rate at sufficiently high polarization because the number of singlet molecules is diminished (two polarized atoms cannot form a singlet molecule). Unfortunately, it is somewhat difficult to interpret the relaxation rate at high polarization because of the changing nuclear slowing down factor (see appendix B). In addition, we must work at large alkali number density so that alkali-alkali relaxation is the dominant spin-relaxation mechanism. Since our optical pumping power is limited, we have not thus far been successful in achieving the required polarization fraction.

2 Christopher Erickson and William Happer at Princeton University are currently working to measure alkali-alkali relaxation in separated Rb isotopes.

3 The tentative calculations of alkali trimer chemical equilibria and the simulations of metastable trimer dynamics could be improved with a better estimate of the trimer Born-Oppenheimer potential energy surface.

4 Future experiments might be designed so that the vapor temperature and alkali number density could be varied independently. We have implicitly assumed that the rapid variation of alkali-alkali relaxation rate with temperature is almost entirely due to changes in the alkali vapor pressure, and it might be important to check that assumption. In addition, a strong temperature dependence that is independent of alkali number density would be a clue about the binding energy of the relaxing system. Such an apparatus would require large temperature gradients, however, and achieving the stability necessary for this work might be a considerable technical challenge.

Appendix A

Physical and Optical Properties of the Alkalis

This appendix summarizes important physical characteristics of the alkalis K, Rb and Cs, and their interaction with light. Section A.1 gives some thermodynamic properties of alkali metals, followed by a description of the relevant atomic energy levels in section A.2. This leads to a brief treatment of the interaction between a free alkali atom and near-resonant light, including Optical Pumping, Faraday Rotation and pressure effects in section A.3.

A.1 Physical Characteristics of the Alkalis

In pure form, the alkalis are metallic and are solid at room temperature. The three heaviest alkalis, K, Rb and Cs, are commonly used for Spin-Exchange Optical Pumping because of their relatively low melting point and high vapor pressure (given in fig A.1 and because their first resonance is reachable by solid state lasers. All of the alkalis are very reactive, particularly with water and oxygen, but to a lesser extent with many substances.

Spin-Exchange Optical Pumping is usually performed at alkali vapor pressures between 10^{13} and 10^{15} cm-3, so we are particularly interested in understanding relaxation processes in that range. This requires the alkali to be enclosed in a cell and heated to 450-550 K. For various technical reasons (see chapter 2), it is necessary to have a buffer

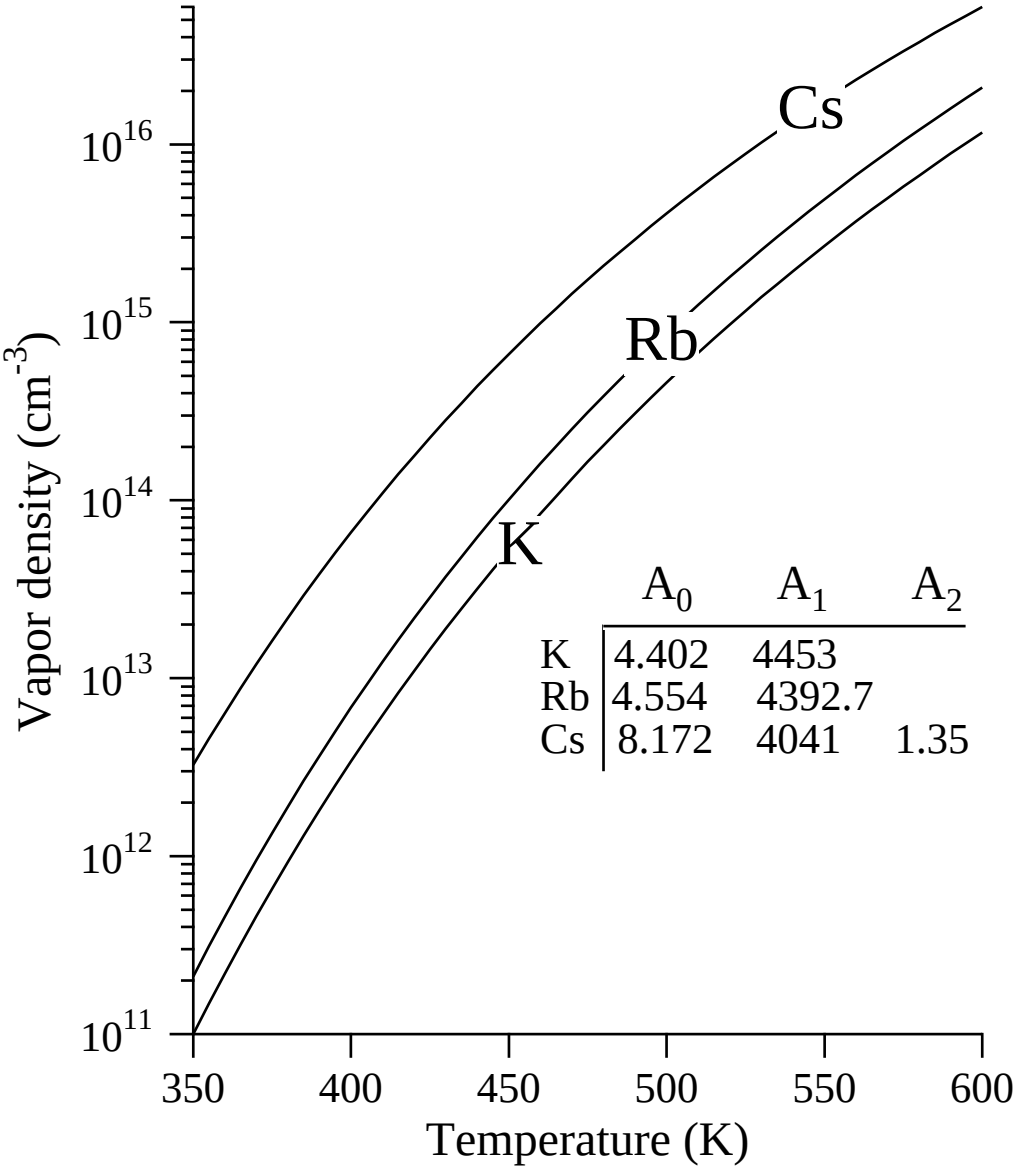

Figure A.1: Vapor pressure of alkali atoms K, Rb and Cs as a function of temperature T. The inset gives melting points and parameterizes the vapor pressures in terms of A_0, A_1, A_2 and T as $\log_{10}(\mathrm{P/Torr}) = A_0 - A_1(^oK/\mathrm{T}) - A_2\log_{10}(\mathrm{T}/^o\mathrm{K})$. Atomic number densities $[A]$ are $[A] = 9.63 \times 10^{18}\mathrm{cm}^{-3}(P/\mathrm{Torr})(^oK/T)$. These curves represent a compromise by [Nesmeianov63] between experiemental results covering temperatures below about 1000 K.

gas in the cell as well, so we choose gases with which the alkalis are non-reactive (He, Ne, Ar, Kr, Xe, CH_4) or minimally reactive such as N_2 and H_2 (see ref. [Happer76]).

A vapor of heavy alkalis is composed of about 99% free atoms, 1% singlet dimers, and a smaller fraction of stable trimers (10^{-5}), triplet dimers (10^{-6}), metastable trimers (10^{-7}). Tetramers and all other molecular forms have fraction $< 10^{-9}$. The dynamics in the vapor are therefore complicated and interesting, as each of the free atoms is cycled through many dimers and timers each second. These processes are discussed in detail in chapters 3 and 7.

A.2 Atomic Energy Levels

A.2.1 Fine Structure

To summarize the gross features of the energy levels for a free alkali atom, we first look at the fine structure, which ignores nuclear orientation. Because alkali atoms can be treated by looking at their single valence electron, excited states with electron orbital angular momentum L $\neq 0$ may have total electron angular momentum J = L + 1/2 or L - 1/2. The energy difference between the two is fairly small, and the states are referred to as an excited state doublet. Figure A.2 shows the energies of the excited states of interest in this experiment for K, Rb and Cs and their natural linewidths. The addition of a magnetic field splits each of the fine structure states into 2J + 1 Zeeman levels corresponding to values of the quantum number m_J. For the B $\leq$ 1T fields achievable in our laboratory, however, the splitting is not visible at the level of detail in fig. A.2 and J remains a good quantum number.

A.2.2 Hyperfine Structure

Each of the fine structure states is further split into a hyperfine manifold by interaction with the nuclear magnetic moment. This splitting is also not visible at the level of fig. A.2, and under the conditions used in this experiment, does not significantly effect the interaction between the atom and light, as I will show in the next section.

The hyperfine structure does play a role in the free evolution of the atom, however. Appendix B shows how its influence can be characterized as a nuclear slowing down

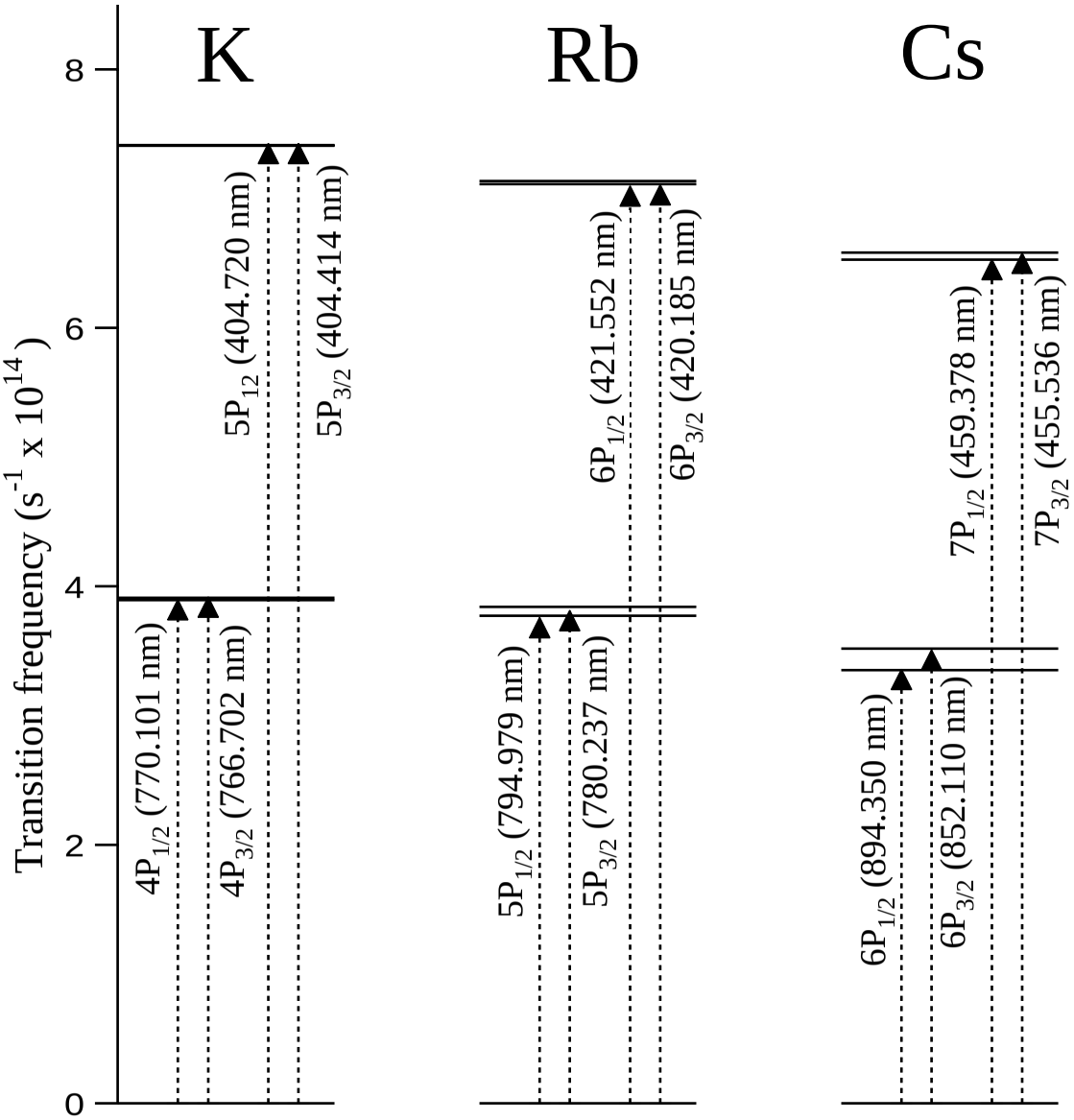

Figure A.2: Lowest fine structure transitions of K, Rb and Cs, and their vacuum wavelengths

factor.

A.3 Semi-Classical Interaction with Light

We use near resonance laser light to polarize the atoms, measure the atomic polarization and to measure the alkali vapor pressure. This section provides the theoretical tools necessary to calculate all of these effects. The treatment is a generalization of ref. [Wu86].

In the absense of light, the Hamiltonian for an alkali atom is

$$H_A = \hbar\omega_{nJm_J}|nJm_J\rangle\langle nJm_J| + g_J\mu_B J_z B + A\mathbf{I}\cdot\mathbf{J} + \ldots \tag{A.1}$$

in which $|nJm_J\rangle$ is a fine structure coupled state and the ellipsis denotes higher order terms such as the nuclear magnetic dipole, electric quadrupole, etc. Atomic center of mass motion is not included explicitly, but it leads to Doppler broadening (see section A.3.2).

We write the most general atomic state $|\psi\rangle$ in the interaction picture as

$$|\psi\rangle = \sum_\alpha c_\alpha|\alpha\rangle e^{i\omega_\alpha t} + \sum_\beta c_\beta|\beta\rangle e^{i\omega_\beta t} \tag{A.2}$$

where $\{|\alpha\rangle\}$ is a set of ground states and $\{|\beta\rangle\}$ is a set of excited states that together diagonalize H_A.

If we now add the interaction with a classical light field,

$$H = H_A - \vec{\mathbf{E}}\cdot\vec{\mathbf{D}} \tag{A.3}$$

where $\vec{\mathbf{E}} = \vec{\mathcal{E}}\mathbf{e}^{-\mathbf{i}\omega\mathbf{t}} + \mathbf{c.c.}$ is the applied electric field and $\vec{\mathbf{D}} = -\mathbf{e}\vec{\mathbf{r}}$ is the induced atomic dipole moment, we may solve for the polarizability dyadic $\overleftrightarrow{\alpha}$

$$\vec{\mathbf{D}} = \overleftrightarrow{\alpha}\,\vec{\mathbf{E}}. \tag{A.4}$$

We therefore calculate $\vec{\mathbf{D}}$ in order to solve for $\overleftrightarrow{\alpha}$, which completely characterizes the light-atom interaction.

The amplitudes c_α and c_β obey the Schrödinger equation

$$\begin{aligned} \dot{c_\alpha} &= \frac{1}{i\hbar} e \sum_\beta c_\beta \mathcal{E} \cdot \langle \alpha | \vec{\mathbf{r}} | \beta \rangle \mathbf{e^{i\Delta_{\alpha\beta} t}} \\ \dot{c_\beta} &= \frac{1}{i\hbar} e \sum_\alpha c_\alpha \mathcal{E} \cdot \langle \beta | \vec{\mathbf{r}} | \alpha \rangle \mathbf{e^{-i\Delta_{\alpha\beta} t}} - \frac{\gamma_\beta}{\mathbf{2}} \mathbf{c}_\beta \end{aligned} \tag{A.5}$$

where I have introduced the phenominological damping rate γ_β to represent spontaneous decay and the effect of buffer gas collisions. The detuning from resonance is $\Delta_{\alpha\beta} = \omega - (\omega_\beta - \omega_\alpha)$. Solving this for the excited state amplitude gives

$$c_\beta = e \sum_\alpha \frac{\vec{\mathcal{E}} \cdot \langle \beta | \vec{\mathbf{r}} | \alpha \rangle \mathbf{e^{-i\Delta_{\alpha\beta} t}} \mathbf{c}_\alpha}{\hbar(\Delta_{\alpha\beta} + i\gamma_\beta/2)}. \tag{A.6}$$

Using this result, and recognizing that coherences such as $c_\alpha^\star c_{\alpha'}$ vanish when averaged over the ensemble, we may calculate

$$\begin{aligned} \langle \vec{\mathbf{D}} \rangle &= -e \langle \psi | \vec{\mathbf{r}} | \psi \rangle \\ &= e^2 \sum_{\alpha\beta} \frac{\langle \alpha | \vec{\mathbf{r}} | \beta \rangle \vec{\mathcal{E}} \cdot \langle \beta | \vec{\mathbf{r}} | \alpha \rangle \mathbf{e^{-i\omega t}}}{-\hbar(\Delta_{\alpha\beta} + i\gamma_\beta/2)} P_\alpha \end{aligned} \tag{A.7}$$

in which $P_\alpha = |c_\alpha|^2$ is the probability to be in ground state α. Combinbing eq. A.4 and A.7 gives

$$\overleftrightarrow{\alpha} = e^2 \sum_{\alpha\beta} \frac{\langle \alpha | \vec{\mathbf{r}} | \beta \rangle \langle \beta | \vec{\mathbf{r}} | \alpha \rangle}{-\hbar(\Delta_{\alpha\beta} + i\gamma_\beta/2)} P_\alpha. \tag{A.8}$$

Because the states $\{|\alpha\rangle, |\beta\rangle\}$ have a definate angular momentum projection, the tensor structure of A.8 simplifies considerably in the spherical basis $r_\pm, r_0 = (x \pm iy)/\sqrt{2}, z$:

$$\overleftrightarrow{\alpha} = e^2 \sum_{\alpha\beta\mu} \frac{\langle \alpha | r_{-\mu} | \beta \rangle \langle \beta | r_\mu | \alpha \rangle}{-\hbar(\Delta_{\alpha\beta} + i\gamma_\beta/2)} P_\alpha \hat{r}_\mu \hat{r}_{-\mu}. \tag{A.9}$$

The interaction can therefore be described by two (complex) polarizabilities:

$$\begin{aligned} D_\pm = -e r_\pm &= \alpha_\pm \mathcal{E}_\pm, \quad \text{where} \\ \alpha_\pm &= -e^2 \sum_{\alpha\beta} \frac{|\langle \beta | r_\pm | \alpha \rangle|^2}{\hbar(\Delta_{\alpha\beta} + i\gamma_\beta/2)} P_\alpha. \end{aligned} \tag{A.10}$$

In principle, the atom-light interaction can be calculated under all conditions by diagonalizing A.1. For our work, however, that amount of effort is not necessary because the high buffer gas pressure suitable for optical pumping causes unresolved hyperfine structure. In addition, we work at detunings many times greater than the hyperfine splitting, and the effect of hyperfine structure on both α and $\alpha_+ - \alpha_-$ (the quantity used to calculate Faraday Rotation) decreases as (splitting/detuning)^2. We therefore find that we can ignore the hyperfine interaction and all higher order terms while introducing negligible error for any of our calculations, and write α as

$$\alpha_\pm = -e^2 \sum_{J' m_J} \frac{|\langle J' m_J \pm 1 | r_\pm | \frac{1}{2} m_J \rangle|^2}{\hbar(\Delta_{1/2, m_J \leftrightarrow J', m_J \pm 1} + i\gamma_{J'}/2)} P_\alpha \tag{A.11}$$

Using standard atomic theory (for instance, see ref. [Woodgate], p. 76), it is straightforward to calculate the detunings and to reduce the matrix elements in the usual way:

$$\begin{aligned} |\langle J' m_J \pm 1 | r_\pm | J m_J \rangle|^2 &= \frac{1}{2J'+1} |\langle J' m_J \pm 1 | J m_J, 1 \pm 1 \rangle|^2 |\langle J' || \vec{\mathbf{r}} || \mathbf{J} \rangle|^2 \\ &= \frac{3\hbar e^2 f_{JJ'}}{2m\omega} \frac{2J+1}{2J'+1} |\langle J' m_J \pm 1 | J m_J, 1 \pm 1 \rangle|^2 \end{aligned} \tag{A.12}$$

Thus,

$$\begin{aligned} \alpha_\pm = -\frac{e^2}{4m\omega} \Bigg(& \frac{P_{\mp 1/2} f_{3/2}}{\Delta_{3/2} \mp \frac{5}{3}\Omega + i\gamma_{3/2}/2} + 3 \frac{P_{\pm 1/2} f_{3/2}}{\Delta_{3/2} \mp \Omega + i\gamma_{3/2}/2} \\ & + 4 \frac{P_{\mp 1/2} f_{1/2}}{\Delta_{1/2} \mp \frac{4}{3}\Omega + i\gamma_{1/2}/2} \Bigg) \end{aligned} \tag{A.13}$$

in which $\Omega = \mu_B B/\hbar$ is the electron spin precession frequency in magnetic field B, $\Delta_{J'}$ is the detuning to the J' excited state at $B = 0$ (but including the pressure shift– see below) and $f_{J'}$ is the ground $\leftrightarrow J'$ oscillator strength. The excited state doublet most nearly in resonance is assumed.

A.3.1 Pressure Shifts/Line Broadening

In the above formalism, the effect of buffer gas collisions is introduced through the line broadening(γ_β) and a shift of the resonance frequency ($\omega_{\alpha\beta}$). Such collisions have no preferred orientation and are Poisson distributed in time, so all Zeeman and hyperfine

Table A.1: Collisional broadening and resonance shift, taken from ref.[Allard82]. Blank entries habe not been measured to date. All broadenings and shifts are in GHz/amagat (1 amagat = 2.69×10^{19} cm^{-3} = number density at STP)

	He		N_2	
Transition	$\delta\omega_{J'}/2\pi$	$\gamma_{J'}/2\pi$	$\delta\omega_{J'}/2\pi$	$\gamma_{J'}/2\pi$
K $4P_{1/2}$	1.01	0.295	1.60	-0.971
K $4P_{3/2}$	1.34	0.160	1.60	-0.861
K $5P_{1/2}$	2.35	0.910		
K $5P_{3/2}$	3.32	1.30		
Rb $5P_{1/2}$	1.25			
Rb $5P_{3/2}$	1.25	-0.100		
Rb $6P_{1/2}$				
Rb $6P_{3/2}$				
Cs $6P_{1/2}$	1.20	0.823	1.91	0.910
Cs $6P_{3/2}$	1.67	0.480	2.42	0.898
Cs $7P_{1/2}$	5.04			
Cs $7P_{3/2}$	3.65			

levels in a given $J \rightarrow J'$ transition are shifted and Lorentzian broadened together. Table A.3.1 gives measured pressure broadening and shifts for the alkali transition / buffer gas combinations used in this experiment.

Collisional broadening dominates at buffer gas pressures above a few Torr. At lower pressures, the dominant broadening mechanism at the high number densities used in this experiment is resonance broadening (see [Kantor85] for measurements and a detailed description of resonance broadening). Natural broadening can always be ignored in these calculations, as can Doppler broadening, because of its relatively narrow width and Gaussian shape.

I have also noted other broadening mechanisms that produce asymmetry in the far wings. Such effects are supposed to arise from quasi-static alkali-buffer gas interactions or, at high alkali densities, alkali-alkali interactions. At present, too little is known about these mechanisms to discuss them qualitatively.

A.3.2 Absorption

As $\sigma_\pm$ light propagates in the z direction through the alkali vapor, it is attenuated as

$$\frac{dI_\pm}{dz} = -I_\pm \, 4\pi N \frac{\omega}{c} \, \mathrm{Im}(\alpha_\pm) \tag{A.14}$$

To simplify this, we note that absorption is only used in this experiment under two circumstances; to measure the vapor pressure, which is done at zero magnetic field, and for optical pumping, which is done with circularly polarized light at large detuning. In either case, the Zeeman effect can be ignored while introducing negligible error. Therefore, we may write eq. A.14 as

$$\frac{dI_\pm}{dz} = -I_\pm \, \frac{\pi e^2 N}{mc} \left[\frac{f_{1/2}\gamma_{1/2}}{\Delta_{1/2}^2 + \gamma_{1/2}^2/4}(1 \mp P) + \frac{f_{3/2}\gamma_{3/2}}{\Delta_{3/2}^2 + \gamma_{3/2}^2/4}(1 \pm \frac{P}{2}) \right] \tag{A.15}$$

where I have replaced $P_{\pm 1/2}$ by the polarization $P = (P_{1/2} - P_{-1/2})/2$.

A.3.3 Optical Pumping

Since each circularly polarized photon absorption corresponds to a change in atomic polarization P, we see how one may control the ground state populations with light. This is known as optical pumping, and many excellent reviews have been written on the subject (for example, [Happer72, Happer87]). I will therefore not dwell on the subtleties, but briefly describe the case most often used for this experiment– pumping using the $P_{1/2}$ transition in the first excited doublet.

In this case, the laser frequency is kept much nearer the $J' = 1/2$ resonance than the $J' = 3/2$ (but still at large detuning compared to broadening or splittings of the $J' = 1/2$ line). We may therefore ignore the second term in eq. A.15. We use sufficient molecular buffer gas to randomize the excited state population after a photon absorption, thus avoiding radiation trapping. This has the effect of returning the atom to either ground state with equal probability. Therefore, a photon absorption transfers (on average) 1/2 unit of angular momentum. Thus,

$$\frac{dP}{dt} = \frac{1}{2N\hbar\omega}\frac{dI_+}{dz}$$

$$= \frac{\pi e^2}{6mc}\frac{I_+}{\hbar\omega}\frac{\gamma_{1/2}}{\Delta_{1/2}^2+\gamma_{1/2}^2/4}(1-P) \tag{A.16}$$

where I have replaced $f_{1/2}$ by its approximate value of 1/3. Note that eq. A.16 only takes into account changes in polarization due to the light.

A.3.4 Faraday Rotation

In addition to the absorption effects described above, the real part of the polarizability leads to an index of refraction that differs between the two helicies of light. The difference depends on both the alkali number density and its polarization, which makes it useful for measuring either quantity. We measure this different by the rotation of the polarization vector of linearly polarized light, known as Faraday Rotation.

Linearly polarized light can be decomposed into circular components, and the phase relationship between the circular components determines the angle of polarization. The difference between indices for the two circular polarization components,

$$n_- - n_+ = \sqrt{1+4\pi N\mathrm{Re}(\alpha_-)} - \sqrt{1+4\pi N\mathrm{Re}(\alpha_+)} \approx 2\pi N(\alpha_- - \alpha_+) \tag{A.17}$$

corresponds to a rotation of

$$\theta = \frac{\pi N l\omega}{c}(\alpha_- - \alpha_+). \tag{A.18}$$

Depending on the detuning, the two helicities of light may be attenuated by different amounts as well, although that does not change the validity of eq. A.18. Such an effect introduces ellipticity to the originally linearly polarized beam, and θ then refers to the angle between the incident linear polarization and the major axis of the ellipse.

Substituting eq. into eq. and expanding in $\Omega = \mu_B B/\hbar$ gives

$$\theta = \frac{\pi N l e^2}{3mc}\left[\left(\frac{\Delta_{3/2}}{\Delta_{3/2}^2+\gamma_{3/2}^2/4} - \frac{\Delta_{1/2}}{\Delta_{3/2}^2+\gamma_{1/2}^2/4}\right)P + \left(7\frac{\Delta_{3/2}^2-\gamma_{3/2}^2/4}{(\Delta_{3/2}^2+\gamma_{3/2}^2/4)^2} + 4\frac{\Delta_{1/2}^2-\gamma_{1/2}^2/4}{(\Delta_{1/2}^2+\gamma_{1/2}^2/4)^2}\right)\frac{\Omega}{3} + O(\Omega^2)\right] \tag{A.19}$$

and therefore

$$\frac{d\theta}{dP} = \frac{\pi N l e^2}{3mc}\left(\frac{\Delta_{3/2}}{\Delta_{3/2}^2+\gamma_{3/2}^2/4} - \frac{\Delta_{1/2}}{\Delta_{3/2}^2+\gamma_{1/2}^2/4}\right) \tag{A.20}$$

$$\frac{d\theta}{dB} = \frac{\pi N l e^2}{9mc}\frac{\mu_B}{\hbar}\left(7\frac{\Delta_{3/2}^2-\gamma_{3/2}^2/4}{(\Delta_{3/2}^2+\gamma_{3/2}^2/4)^2} + 4\frac{\Delta_{1/2}^2-\gamma_{1/2}^2/4}{(\Delta_{1/2}^2+\gamma_{1/2}^2/4)^2}\right). \tag{A.21}$$

For conditions of large (500 GHz) detuning and $B < 1T$ used in this experiment, ignoring the the $O(\Omega^2)$ and higher terms introduces error of about 1%.

We can therefore use Faraday rotation to make two independent measurements. By first measuring $d\theta/dB$ for an unpolarized vapor, we solve for the alkali number density N using eq. A.21. Then we fix B, measure $\theta(t)$ and convert to $P(t)$ using eq. A.20. I discuss both techniques in more detail in chapter 2.

Appendix B

Spin Exchange and Spin Temperature

This appendix summarizes how my measured relaxation rates are affected by alkali-alkali spin exchange collisions and the alkali hyperfine interaction. The explanations and derivations found here are mostly minor variations of work in refs. [Happer72, Anderson60].

B.1 Electron-Electron Spin Exchange

A spin-exchange collision between two alkali atoms A and B can be represented as

$$A(\uparrow) + B(\downarrow) \rightarrow A(\downarrow) + B(\uparrow) \tag{B.1}$$

in which the arrows refer to the orientation of valence electron spin. Conceptually, we may think of this as the precession of each individual electron spin around the singlet coupled state. We therefore expect spin exchange whenever

$$\int \frac{dt}{\hbar} V_S(r(t)) \gg 1 \tag{B.2}$$

where the integral is over collision trajectory and V_S is the singlet potential.

This simple picture gives an exchange cross-section very close to the experimentally observed value of $\tilde{2}00\mathring{A}^2$ for K, Rb and Cs ([Happer72]). In addition, since the precession can be much faster than the precession around any laboratory magnetic field, we do not expect this process to be decoupled.

Therefore, in a typical alkali vapor with 10^{15} atoms/cm^3, each alkali atom exchanges with its neighbors roughly 10^5 times each second. This is much faster than any optical pumping or relaxation rate in this experiment.

The effect of electron spin-exchange is to cause atomic coherences, such as hyperfine precession, to decay. A mathematical treatment, including the effect of spin-exchange collisions on the atomic density matrix, can be found in [Appelt98, Happer72].

B.2 The Hyperfine Interaction

Just as electron-electron spin exchange rapidly distributes polarization among alkali valence electrons, the hyperfine interaction distributes spin between the alkali valence electrons and nuclei. This process can also be very rapid. However, noting that the alkali hyperfine interaction is decoupled by a ∼kG magnetic field, Walker and Anderson (refs. [Walker93, Anderson95]) have shown that the rate of polarization exchange between electrons and nuclei is slowed down approximately as $1/(1+x^2)$ where $x = g_S \mu_B B/\Delta E_{hyp}$ is the Breit-Rabi parameter.

B.3 Spin Temperature

If the previous two processes proceed at rates much larger than any spin relaxation or optical pumping rate, the system remains in equilibrium with respect to spin exchange even while it is taken out of its global equilibrium with respect to relaxation. Such a system is said to be in spin temperature [Anderson60]. This characterization simplifies the analysis considerably, because the populations of all electron and nuclear Zeeman levels can be written in terms of one parameter, the inverse spin temperature β. For the case of a homonuclear alkali vapor, the spin temperature characterization can be understood quite intuitively. The following is a special case of the more general work in [Anderson60].

In spin temperature, the electron and nuclear Zeeman populations are in equilibrium with respect an exchange process

$$(m_S + 1, m_I) \leftrightarrow (m_S, m_I + 1) \tag{B.3}$$

In order for the forward and backward processes to proceed at the same rate, we must have the probabilities to be in m_S, m_I related by

$$P(m_S + 1)P(m_I) = P(m_S)P(m_I + 1) \tag{B.4}$$

for each m_I = -I ... I-1. These 2I equations, along with $\sum P(m_S) = \sum P(m_I) = 1$, allow us to eliminate all but one of the probabilities, although it is convenient to parameterize them all in terms of the inverse spin temperature parameter

$$e^{-\beta} = P(m_{1/2})/P(m_{-1/2}) \tag{B.5}$$

This use of β is analagous to the more familiar $\beta = 1/kT$ in that $\beta = 0$ corresponds to the maximally disordered (unpolarized) state and $\beta = \pm\infty$ corresponds to the most ordered (polarized) states. In terms of β, the solutions to eq. B.4 are:

$$\begin{aligned} P(m_S) &= e^{\beta m_S} \frac{2}{\cosh(\beta/2)} \\ P(m_I) &= e^{\beta m_I} \frac{\sinh(\beta/2}{\sinh(\beta(I + 1/2))}. \end{aligned} \tag{B.6}$$

Note that the probability of being in a spin state with z projection m_F is is proportional to $exp(\beta m_F)$. This is a general feature of a system in spin temperature equilibrium.

B.3.1 Nuclear Slowing Down Factors

From eq. B.6, we may calculate the expectation values of electron and nuclear spin.

$$\begin{aligned} \langle S_Z \rangle &= \sum P(m_S)m_S = (1/2)\tanh(\beta/2) \\ \langle I_Z \rangle &= \sum P(m_I)m_I = ([I]/2)\mathrm{ctnh}([I]\beta/2) - (1/2)\mathrm{ctnh}(\beta/2) \end{aligned} \tag{B.7}$$

in which $[I] = 2I + 1$.

In general, the fraction of polarization stored in the electrons is a nonlinear in β, which makes analysis of relaxation processes difficult. For instance, when measuring a

Table B.1: Slowing down factors appropriate for electron relaxation. The observed relaxation rate is the true electron relaxation rate multiplied by $1/(1+\epsilon)$.

	$1/(1+\epsilon)$
K	1/6
^{85}Rb	3/38
^{87}Rb	1/6
Rb (nat.)	1/10.8
Cs	1/22

relaxation process acting on the electron spin, the measured relaxation rate is slower than the true electron relaxation rate by a factor $1+\langle I_Z\rangle/\langle S_Z\rangle$ due to the polarization transferred from the nucleus. Likewise, the measured rate for a nuclear relaxation process is slower than the true rate by $1+\langle S_Z\rangle/\langle I_Z\rangle$.

We minimize this problem by keeping the polarization fraction low when making relaxation measurements. In the limit of low polarization,

$$\begin{aligned} \langle I_Z\rangle/\langle S_Z\rangle &\to \epsilon \\ \text{where } \epsilon &= \frac{4}{3}I(I+1) \end{aligned} \tag{B.8}$$

so the measured and true relaxation rates are related by a constant 'slowing down factor' of $1/(1+\epsilon)$ for processes acting on the electron and $\epsilon/(1+\epsilon)$ for processes acting on the nucleus. I find that this approximation leads to negligible error as long as the polarization fraction is kept below about 5%. The slowing down factors appropriate for electron relaxation are given in ref. [Happer72]. The slowing down factors for nuclear relaxation are given in table 3.3.

B.3.2 Departure From Spin Temperature

The results of the previous section depend on the assumption that the rate for electron $\leftrightarrow$ nuclear spin exchange greatly exceeds that of any optical pumping or relaxation rate. If we wish to measure relaxation rates under circumstances where this is not the case, a correction must be made for the departure from spin temperature. This effect can be analyzed more rigorously by coupling the electron and nuclear spin into 'eigenobservables' (independently decaying modes of the density matrix) as has been

done in ref. [Erickson99], but a simpler, rate equation model is sufficient for my purposes and provides some physical insight. Note that this model is only applicable to small deviations from spin temperature and relaxation processes acting on the alkali valence electron.

The return to spin temperature in the presence of electron relaxation at rate Γ_S can be described by rate equations governing electron and nuclear polarization (S_z and I_z)

$$\begin{aligned} \frac{dI_z}{dt} &= -\gamma_x(I_z - \epsilon S_z) \\ \frac{dS_z}{dt} &= -\gamma_x(\epsilon S_z - I_z) - \Gamma_S S_z \end{aligned} \tag{B.9}$$

where γ_x is the rate of polarization exchange between the alkali electrons and nuclei. As mentioned in section B.2,

$$\begin{aligned} &\gamma_x = \frac{\gamma_{x(B=0)}}{1 + (B/B_0)^2}, \\ &\text{with } B_0 = \frac{\Delta E_{hyp}}{g_S \mu_B}. \end{aligned} \tag{B.10}$$

As long as $\gamma_x \gg \Gamma_S$, the system will approach quasi-steady state at long times such that both electron and nuclear spin are relaxing as

$$S_z \propto e^{-\Gamma t}, \quad I_z \propto e^{-\Gamma t} \tag{B.11}$$

where Γ is the measured relaxation rate. Substituting eq. B.11 into B.9 and expanding in powers of Γ_S/γ_x gives

$$\begin{aligned} \Gamma &= \Gamma_S \frac{1}{1+\epsilon}\left[1 - \frac{\Gamma_S}{\gamma_x}\frac{4\epsilon}{(1+\epsilon)^2} + \cdots\right] \\ &= \Gamma_S \frac{1}{1+\epsilon}\left[1 - \frac{\Gamma_S}{\gamma_{x(B=0)}}\frac{4\epsilon}{(1+\epsilon)^2}\left(1 + (B/B_0)^2\right) + \cdots\right] \end{aligned} \tag{B.12}$$

Note the appearence of the slowing down factor $1/(1+\epsilon)$. In addition, for $\Gamma_S/\gamma_x \neq 0$, the measured relaxation rate decreases quadratically with the application of a magnetic field. This effect is particularly pronounced in K because of the small ground state hyperfine splitting, and can be clearly seen in fig. 4.6. The fits to measured relaxation

rate therefore contain an extra term quadratic in magnetic field.

Appendix C

Numerical Techniques

In several sections of this thesis, I refer to relaxation rate calculations performed by numerically diagonalizing the relaxing interaction. This appendix serves as a short description of how that process works.

I represent the state of a system at time t_0 with the density matrix ρ_0. For $t > t_0$, ρ evolves under the influence of a time-independent interaction Hamiltonian H_I. Typically, we are interested in the average fractional polarization loss after a period of coherent evolution. All periods of coherent evolution do not have the same length, but are distributed as $\mathrm{F}(\tau)$.

This problem can be approached numerically as follows:

1 Solve for the unitary matrix E such that $H_I' = E^\dagger H_I E$ is diagonal. I used the routine 'jacobi' in Numerical Recipies ([Press]).

2 Rotate ρ_0 to the primed basis set as $\rho_0' = E^\dagger \rho_0 E$

3 Subsequent time evolution in the primed basis set

$$i\hbar \frac{d\rho'}{dt} = -[\rho, H_I'] \tag{C.1}$$

can now be simplifed as

$$\rho'_{mn}(t) = \rho'_{0\,mn} e^{-i\omega_{mn}t} \tag{C.2}$$

where $\omega_{mn} = (H'_{I\,mm} - H'_{I\,nn})/\hbar$. Because the final answer is real, we may

replace $e^{-i\omega_{mn}t}$ by $\cos(\omega_{mn}t)$ without affecting the result. Averaged over the distribution of coherence times, we have

$$\rho'_{F\,mn} = \int_0^\infty dt\ F(t)\rho'_{0\,mn}\cos(\omega_{mn}t) \tag{C.3}$$

For the common situation

$$F(\tau) = \frac{1}{\tau_c}e^{-\tau/\tau_c} \tag{C.4}$$

this further simplifies to

$$\rho'_{F\,mn} = \rho'_{0\,mn}\frac{\omega_{mn}^2\tau_c^2}{1+\omega_{mn}^2\tau_c^2} \tag{C.5}$$

4 Finally, transform back to the original basis set as $\rho_F = E\rho'_F E^\dagger$ and compute the fractional polarization loss as

$$F = \frac{\sum_m \rho_{F\,mm}F_z(m)}{\sum_m \rho_{0\,mm}F_z(m)} \tag{C.6}$$

where $F_z(m)$ is the z projection of the total spin of state m.

Appendix D

Classical Trajectory Simulations

In this appendix, I briefly describe my classical-trajectory, Monte Carlo simulations of molecular dynamics. I have used these simulations to estimate the breakup and reorientation cross-sections for alkali dimers in a buffer gas, and to estimate the chemical exchange cross-section in alkali atom-dimer collisions. In addition, by simulating the full duration of a chemical exchange collision, I have estimated the density and lifetime of metastable trimers in the vapor.

All of these applications are similar in that a third body (alkali atom or buffer gas) is incident on a bound alkali dimer. For simulating chemical exchange and metastable K trimers, I used the three-body K potential surface of ref. [Martins83] to determine particle accelerations. This potential reduces to a singlet dimer potential when one of the atoms is at large distance. For simulating dimer breakup and reorientation, I used the singlet dimer potential as described in section 3.1 and treated collisions as classical hard-sphere interactions when one of the alkali atoms and the buffer gas approached to within $2R_0$ (R_0 is the hard-sphere radius). I chose $R_0 = 1.22\mathring{A}$ to reproduce the measured value of the cross-section for Rb reorientation in N_2 (section 3.5).

Each simulation then proceeded according to the following steps:

1 Choose the initial dimer rotational and vibrational energies from a thermal distribution. Pick the initial direction of the dimer's angular momentum from a uniform distribution on the unit sphere. Pick the initial phases of rotational and vibrational motion randomly. The dimer initially has no center-of-mass motion.

2 Choose the initial velocity of the third body from a thermal distribution using the reduced mass of the third body-dimer system and pick its impact parameter is from the distribution $P(b) = 2b/b_{max}^2$. b_{max} should be bigger than the largest impact parameter for which the atom and dimer are likely to interact– I find $b_{max} = 13\mathring{A}$ works well in all cases. The initial third body position is $25\mathring{A}$ from the dimer in a random direction.

3 Solve for the classical particle motions numerically until they are no longer contained in circle $40\mathring{A}$ in diameter.

4 For simulations of dimer reorientation and breakup, go back to step 2 unless one of the dimer atoms has escaped.

During each simulation, I kept track of constants of the motion to verify that numerical errors were not a problem. Under no circumstances did the total energy change by more than 10^{-6}eV or the total angular momentum change by more than one part in 10^5.

For simulations of chemical exchange and metastable trimers, I also added up the total amount of time that all three atoms were contained within a circle of $10\mathring{A}$, which I will refer to as τ_{dwell}, and recorded which atom escaped at the end of each simulation. For simulations of dimer reorientation, I kept track of the value of $Q = 3/2\cos^2(\theta) - 1/2$ after each collision, where θ is the total angle through which the dimer angular momentum has been rotated by collisions. The randomization rate of Q is a measure of the rate at which the interactions 3.5 and 5.7 are subject to decoherence.

I repeated each simulation at least 5000 times and averaged the above quantities as follows:

1 The dimer breakup cross-section (σ_b) is πb_{max}^2 divided by the average number of buffer gas collisions required to break up a dimer.

2 The dimer reorientation cross-section (σ_J) is πb_{max}^2 divided by the average number of buffer gas collisions required for Q to fall to 1/e.

3 The chemical exchange cross-section (σ_{ex}) is the πb_{max}^2 times the fraction of collisions for which the incident and escaping atom are different.

4 The distribution of metastable K_3 dwell times is displayed in figure D.1, along with the approximate fit I used in eq. C.3 and 7.17 to estimate the relaxation rate in metastable trimers. Note the surprisingly long lifetimes possible in a metastable trimer– if the atom and dimer interact at all, they stay together for an average of about 100 ps, and lifetimes of a nanosecond or longer are not uncommon. This result may help explain alkali-alkali relaxation, as discussed in chapter 7.

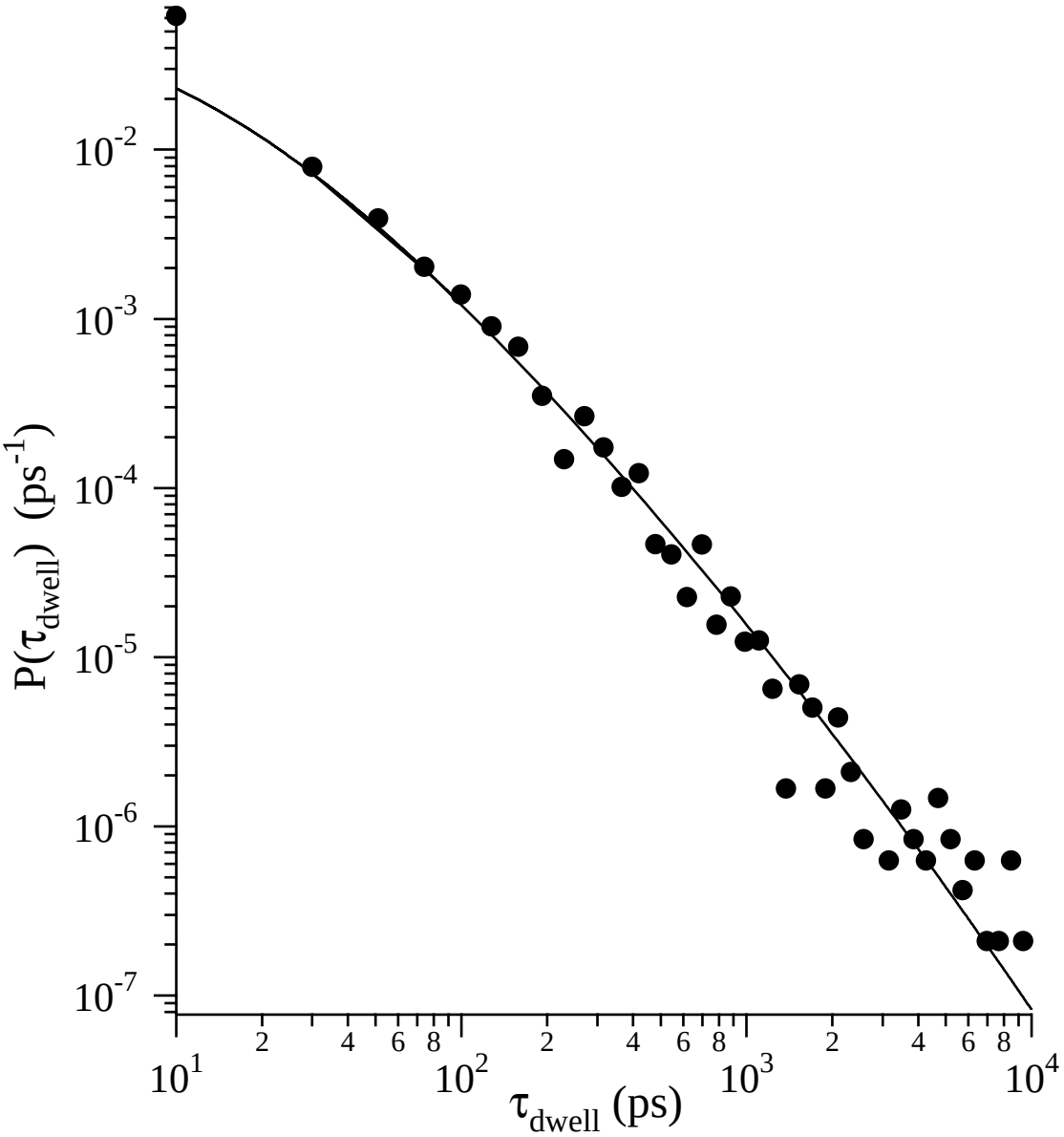

Figure D.1: Probability density for a simulated exchange complex $K + K_2 \rightarrow K_3 \rightarrow K + K_2$ to remain in the metastable K_3 state for a time τ_{dwell}. The fit shown is $P(\tau_{dwell}) \propto exp(-20[(\tau_{dwell}/ps) + 10ps]^{1/15})$. The leftmost point is abnormally high because a significant fraction of simulated atoms and dimers never interact at all, and therefore have an interaction time of zero. I have eliminated these when calculating both the exchange cross-section and average dwell time.

Appendix E

Knife-Edge Gaskets and Windows

This appendix describes our method for sealing windows with a knife-edge copper gasket. Our technique is a slight modification of the procedure developed by Noble and Kasevich for UHV work (described in ref. [Noble94]).

We have used this technique to successfully seal windows on 2 3/4" and 4 1/2" Conflat ports. Our attempts to seal windows on Conflat mini-flange (1 3/8") were not very successful as the windows broke frequently.

The seals held pressure from 10^{-9} Torr to 20 atmospheres, withstood temperatures up to 600 K and were not significantly affected by the presence of a dense (up to 10^{18} cm^{-3}) alkali vapor.

The window to be sealed in this manner should be at least as large as the Conflat gasket O.D. (2" diameter for 2 3/4" Conflat, 3 3/8" diamter for 4 1/2" Conflat). We used 3/8" thick Pyrex circles, although coated windows and windows made of other materials should work equally well.

First, we machine a knife-edge into a standard Conflat gasket as follows:

1 Mount a standard Conflat gasket on the jig shown in fig. E.1 using the bolts labeled A1-A3. Secure the jig in a lathe set to turn at about 250 rpm.

2 Use a tool bit with a 60 deg. included angle pointing at the gasket. For the first cut, put the tip of the tool bit 3 mils (1 mil = 1/1000 in.) farther from the axis of rotation than the middle of the gasket (see fig. E.2). Cut 5 mils deep and feed the tool bit outward to the edge of the gasket. (Note

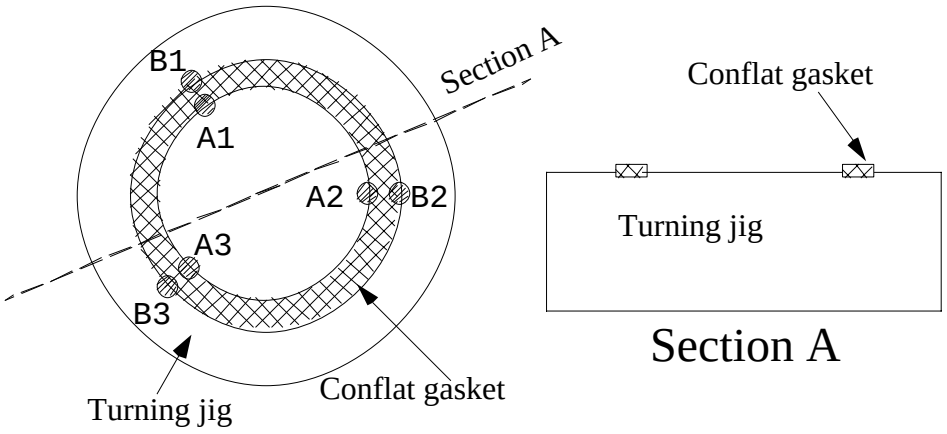

Figure E.1:

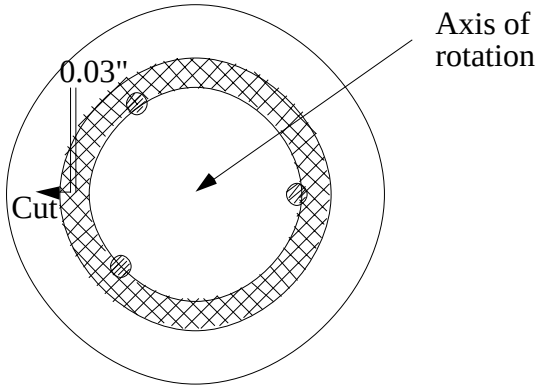

Figure E.2:

that most lathes show the diameter of the circle being cut, so the reading will show 6 mils rather than 3).

3 Make 5 more cuts, starting 3 mils farther from the axis of rotation and 5 mils deeper each time.

4 *leaving the jig in the lathe and bolts A1-A3 in place*, tighten bolts B1-B3. Now, remove bolts A1-A3.

5 Put the tip of the tool bit 3 mils closer to the axis of rotation than the middle of the gasket. Cut 5 mils deep and feed the tool bit inward to the edge of the gasket. Make 5 more cuts, starting 3 mils closer to the axis of rotation and 5 mils deeper each time.

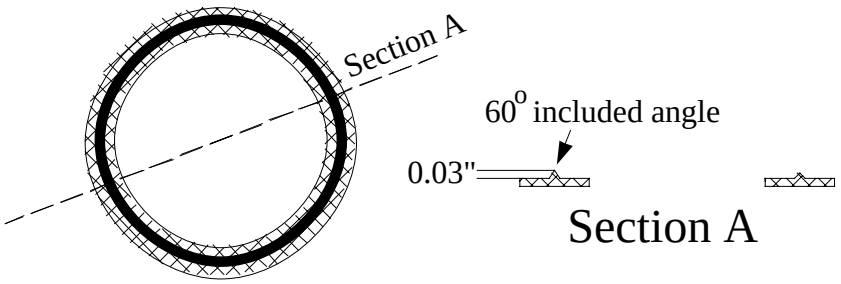

Figure E.3:

6 Remove the gasket from the jig and deburr it.

The completed gasket is shown in fig. E.3. Check the knife edge for damage or burrs. If any damage to the knife edge is visible, the gasket will almost definately leak and should not be used.

The tool bit typically needs to be sharpened after making 2 gaskets.

Next, we seal the windows as follows:

1 Machine the window retaining ring shown in fig. E.4. This ring should be made from stainless steel. It is simplest to start from a Conflat blank or other used Conflat piece. The retaining ring dimensions shown in fig. E.4 are appropriate for a 2" window sealed onto a 2 3/4" Conflat port. In general, the window should fit into a hole with diameter 20 mils greater than that of the window.

2 Cut 30 circles of aluminum foil with the same diameter as the window to be sealed. Place them in the retaining ring.

3 Place the (cleaned) window on top of the aluminum foil so that it sits inside the retaining ring.

4 Place the knife-edge gasket on top of the window, with the knife edge pointing toward the window.

5 Attach (but do not tighten) the whole assemly onto the Conflat port using standard bolts and plate nuts. The bolts may need to be longer than usual due to the thickness of the window. The Conflat knife edge seals against the other side of the knife-edge gasket.

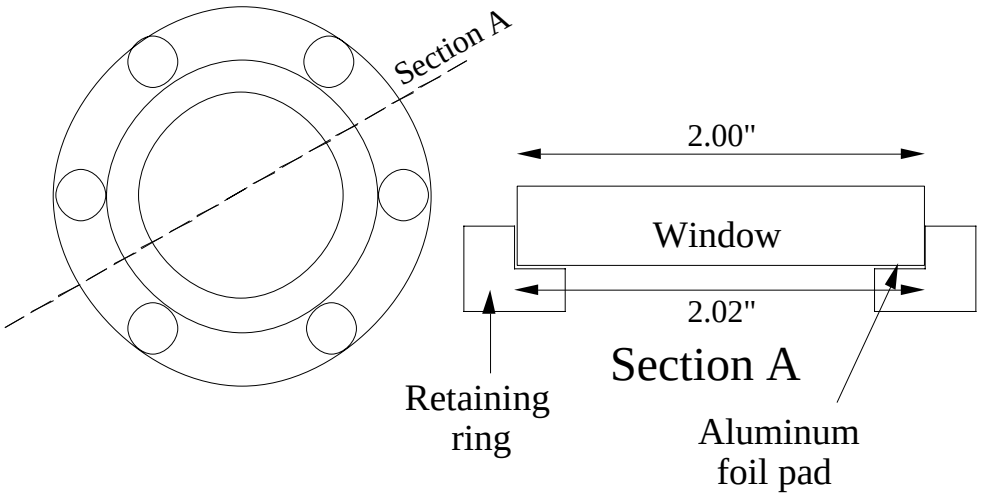

Figure E.4:

6 Tighten the bolts slowly and evenly to 20 in-lb. Above 20 in-lb, use a torque wrench and tighten the bolts in a star pattern, increasing the torque by no more than 1 in-lb each time. We find it best to tighten the bolts to 45 in-lb, let it sit for a few hours, and continue a final torque of 55-60 in-lb.

7 Carefully remove the aluminum foil from the outside of the window with an Exacto knife or sharp screwdriver.

The sealed window is shown in figs. 2.2a and 2.2d.

A window sealed in the above manner may be heated and cooled quite quickly, although the bolts tend to loosen over time and temperature cycling. Periodically retightening the bolts to the original torque helps prevent leaks.

Bibliography

[Abragam] A. Abragam. *Principles of Nuclear Magnetism.* Oxford University Press (1961).

[Allard82] Nicole Allard and John Keilkopf. The effect of neutral nonresonant collisions on atomic spectral lines. *Rev. Mod. Phys.* **54**, 4 1103–82 (1982).

[Amiot91] C. Amiot. The $X^1\Sigma_g^+$ Electronic State of K_2. *J. Mol. Spectr.* **147**(2), 370–82 (1991).

[Anderson60] L. W. Anderson, F. M. Pipkin and J. C. Baird. Hyperfine Structure of Hydrogen, Deuterium and Tritium. *Phys. Rev.* **120**, 1279 (1960).

[Anderson95] L. W. Anderson and T. Walker. Spin-Exchange Optical Pumping of Hydrogen and Deuterium Nuclei. *Nuc. Instr. and Meth. in Phys. Res. A.* **357**(2-3), 220-24 (1995).

[Appelt98] S. Appelt, A. Ben-Amar Baranga, C. J. Erickson, M. Romalis, A. R. Young, W. Happer. Theory of Spin-Exchange Optical Pumping of ^{3}He and 129Xe. *Phys. Rev. A* **82**(2) 1412–39 (1998).

[Arecchi] F. T. Arecchi and E. O. Sculz-Dubois. Laser Handbook vol. 1. Amsterdam, *North Holland Publishing Compnay* (1972).

[Anthony93] P. Anthony, *et al.* (E124 Collaboration). *Phys. Rev. Lett.* **71**, 959 (1993).

[Baranga98] A. Ben-Amar Baranga, S. Appelt, M. V. Romalis, C. J. Erickson, A. R. Young G. D. Cates and W. Happer. Polarization of ^{3}He by Spin Exchange With Optically Pumped Rb. *Phys. Rev. Lett.* **80**(13), 2801–4 (1998).

[Barrat54] J. P. Barrat, J. Brossel and A. Kastler. *Compt. Rend.* **239**, 1196 (1954).

[Bhaskar80] N. D. Bhaskar, J. Pietras, J. Camparo and W. Happer. Spin Destruction in Collisions between Cesium Atoms. *Phys. Rev. Lett.* **44**, 14, 930–33 (1980).

[Blatt] John M. Blatt and Victor F. Weisskopf. *Theoretical Nuclear Physics.* Dover Publications, Inc., New York (1952).

[Boesten96] H. M. J. M. Boesten, C. C. Tsai, B. J. Verhaar and D. J. Heinzen. Phys. Rev. Lett. **77**, 5194 (1996). Rev. A **59**, 1936 (1999).

[Bouchiat71] M. A. Bouciat, J. Brossel and L. C. Pottier. Evidence for Rb-Rare-Gas Molecules from the Relaxation of Polarized Rb Atoms in a Rare Gas. Experimental Results. *J. Chem. Phys* **56**, 3703–14 (1972).

[Brewer62] R. G. Brewer. Rubidium Spin Relaxation induced by Hydrogen. *J. Chem. Phys.* **37**, 2504 (1962).

[Chupp94] T. E. Chupp, R. J. Hoare, R L. Walsworth and Bo Wu. Spin-Exchange Pumped ^{3}He and ^{129}Xe Zeeman Masers. *Phys. Rev. Lett.* **72**, 2363 (1994).

[Clementi74] Enrico Clementi and Carla Roetti. Roothaan-Hartree-Fock Atomic Wavefunctions. *Atomic Data and Nuclear Data Tables* **14** 177-478 (1974).

[Eckel93] H.-A. Eckel, J.-M. Gress, J. Biele and W. Demtröder. Sub-Doppler Optical Double-Resonance Spectroscopy and Rotational Analysis of Na_3. *J. Chem. Phys.* **98**(1), 135–39 (1993).

[Elbs99] Michael Elbs, Hors Knockel, Tanja Laue, Christian Samuelis and Eberhard Tiemann. Observation of the last bound levels near the Na_2 ground-state asymptote. *Physical Review A* **59**, 5 3665-3673 (1999).

[Erickson99] Christopher Erickson, Private Communication.

[Fitzgerald98] R.J. Fitzgerald, K.L. Sauer and W. Happer. Cross-relaxation in laser-polarized liquid Xenon. *Chem. Phys. Lett.* **284**, 1–2, 87–92 (1998).

[Frederico99] T. Frederico, Lauro Tomio, A. Delfino and A. E. A. Amorim. Scaling Limit of Weakly Bound Triatomic States. *Phys. Rev. A* **60**, 1, R9–12 (1999).

[Gershenfeld98] N. Gershenfeld and I. L. Chuang. Quantum Computing with Molecules. *Scientific American* **278**, 6, 50–55 (1998).

[Glas78] H.-J. Glas and H. G. Weber. Collision Induced Dissociation of Cs_2 Studied by Atom-Molecule-Exchange Optical Pumping. *Z. Physik A* **284**, 253–60 (1978).

[Gupta74] R. Gupta, W. Happer, G. Moe and W. Park. Nuclear Magnetic Resonance of Diatomic Alkali Molecules in Optically Pumped Alkali Vapors. *Phys. Rev. Lett.* **32**(11), 574–77 (1974).

[Happer76] W. Happer. Laser Snow: Particle Formation by Resonant Light. *Optics Communications* **18**(1), 93 (1976).

[Happer87] W. Happer and W. A. Van Wijngaarden. An optical pumping primer. *Hyperfine Interactions* **38**, 435–470 (1987).

[Happer72] William Happer. Optical pumping. *Reviews of Modern Physics* **44**, 2 169–249 (1972).

[Huber80] R. Huber and H. G. Weber. The Collision Complex in the Exchange Reaction $Na+Na_2$. *Chem. Phys.* **37**, 173–80 (1979).

[Huber80] R. Huber, M. Knapp, F. König, H. Reinhard and H. G. Weber. Magnetic Shielding and Spin-Rotation Interaction in Ground State Alkali Molecules. *Z. Physik A*, **296**, 95–9 (1980).

[Jansch98] H.J. Jansch, T. Hof, U. Ruth, J. Schmidt, D. Stahl and D. Fick. NMR of surfaces: sub-monolayer sensitivity with hyperpolarized ^{129}Xe. *Chem. Phys. Lett.* **296**, 1–2, 146–150 (1998).

[Kadlecek98A] S. Kadlecek, L. W. Anderson and T. Walker. Measurement of Potassium-Potassium Spin Relaxation Cross Sections. *Nucl. Inst. Meth. Sci. Res. A* **402**, 208–11 (1998).

[Kadlecek98B] S. Kadlecek, L. W. Anderson and T. Walker. Field Dependence of Relaxation in a Dense Rb Vapor. *Phys. Rev. Lett.* **80**, 5512-16 (1998).

[Kadlecek98C] S. Kadlecek, T. Walker, D. Walter and W. Happer. Anisotropic Relaxation in Spin-Exchange Collisions of Alkali Atoms. Submitted for publication, July 1998.

[Kamke75] W. Kamke. Nuclear Magnetic Resonance of K_2 in Optically Pumped Potassium Vapor. *Phys. Lett.* **55A**(1), 15–16 (1975).

[Kantor85] P. Kantor, A. V. Mokhov, N. P. Penkin and L. N. Shabonova. Resonance Broadening of 794.7- and 780.0-nm Rb line. *Optics and Spectroscopy* **58**(6), 745–49 (1985).

[Kompitsas75] M. Kompitsas and H. G. Weber. A Study of the Nuclear Spin Polarization of Na_2 by Optical Pumping. *Chem. Phys. Lett.* **35**(2), 277–79 (1975).

[Knize89] R. J. Knize. Spin Destruction in Rubidium-Rubidium and Potassium-Potassium Collisions. *Phys. Rev. A* **40**, 11, 6219-22 (1989).

[Kornath98] Andreas Kornath, Ralf Ludwig and Anja Zoermer. Small Potassium Clusters. *Angew. Chem. Int. Ed.* **37**, 11, 1575–7 (1998).

[Krauss90] M. Krauss and W. J. Stevens. Effective Core Potentials and Accurate Energy Curves for Cs_2 and Other Alkali Diatomics. *J. Chem. Phys.* **93**, 4236–42 (1990).

[Linden98] N. Linden, H. Barjat and R. Freeman. An implementation of the Deutsch-Jozsa algorithm on a three-bit NMR quantum computer. *Chem. Phys. Lett.* **296**, 1–2, 61–67 (1998).

[Logan52] R. A. Logan, R. E. Coté and P. Kusch. The Sign of the Quadrupole Interaction Energy in Diatomic Molecules. *Phys. Rev.* **86**(3), 280–87 (1952).

[Marinescu94] M. Marinescu, H. R. Sadeghpour and A. Dalgarno. Dispersion Coefficients for Alkali-Metal Dimers. *Phys. Rev. A* **49**(2), 982–87 (1994).

[Mascord76] D. J. Mascord, H. W. Cruse and R. Grice. Reactive Scattering of Alkali Dimers : Velocity Analysis of Na + Rb_2 $\rightarrow$ NaRb + Rb. *Mol. Phys.* **32**(1), 131–44 (1976).

[Martins83] José Luís Martins, Roberto Car and Jean Buttet. Electronic Properties of Alkali Trimers. *J. Chem. Phys.* **78**(9), 5646-55 (1983).

[McNeal62] R. J. McNeal. Disorientation Cross-Sections in Optical Pumping. *J. Chem. Phys.* **37**, 2726 (1962).

[Mies96] F. Mies, C. Williams, P. Julienne, and M. Krauss. Estimating Bounds on Collisional Relaxation Rates of Spin-Polarized ^{85}Rb Atoms at Ultracold Temperatures. *J. Res. Natl. Inst. Stand. Technol.* **101**, 521–35 (1996).

[Migdalek98] Jacek Migdalek and Yong Ki Kim. Core Polarization and Oscillator Strength Anomaly in Potassium, Rubidium and Caesium. *J. Phys. B: At. Mol. Opt. Phys.* **31**, 1947 (1998).

[Nagengast98] W. Nagengast, A. Nass, C. Grosshauser, K. Rith and R. Schmidt. Relaxation of Electron Polarization for Optically Pumped Rubidium Atoms. *J. Appl. Phys.* **83**, 11, 5626–31 (1998).

[Nesmeianov63] An. N. Nesmeianov. *Vapour Pressure of the Elements.* New York, *Academic Press* (1963).

[Newbury91] N. R. Newbury, A. S. Barton, P. Bogorad, G. D. Cates, M. Gatzke, B. Saam, L. Han, R. Holmes, P. A. Souder, J. Xu and D. Benton. Laser Polarized Muonic Helium. *Phys. Rev. Lett.* **67**, 3219 (1991).

[Noble94] A. Noble and M. Kasevich. UHV Optical Window Seal to Conflat Knife Edge. *Rev. Sci. Inst.* **65**, 3042-5 (1994).

[Press] William H. Press, Saul H. Teukolsky, William T. Vetterling and Brian P. Flannery. *Numerical Recipies in C: The Art of Scientific Computing* Cambridge University Press (1993).

[Raferty91] D. Raferty, H. Long, T. Meersmann, P. J. Graninetti, L. Reven and A. Pines. High Field NMR of Adsorbed Xenon Polarized by Laser Pumping. *Phys. Rev. Lett.* **66**, 584 (1991).

[Reif] F. Reif. *Fundimentals of Statistical and Thermal Physics.* McGraw-Hill (1965).

[Schmidt97] D.M. Schmidt, J.S. George, S.I. Penttila, A. Capriham and E. Fukushima. Diffusion imaging with hyperpolarized ^{3}He gas. *Journal of Magnetic Resonance* **129**, 2, 184–187 (1997).

[Townes] C. H. Townes and A. L. Schawlow *Microwave Spectroscopy.* Dover Publications, Inc., New York (1975).

[Tsai97] C. C. Tsai, R. S. Freeland, J. M. Vogels, H. M. J. M. Boesten, B. J. Verhaar and D. J. Heinzen. Two-Color Photoassociation Spectroscopy of Ground State Rb_2. *Phys. Rev. Lett.* **79**, 1245–48 (1997).

[VanEsbroeck85] P. E. Van Esbroeck, R. A. McLean, T. D. Gaily, R. A. Holt and S. D. Rosner. Hyperfine Structure of Na_2. *Phys. Rev. A* **32**(5), 2595–601 (1985).

[Wagshul94] M. E. Wagshul and T. E. Chupp. Laser Optical Pumping of High-Density Rb in Polarized ^{3}He Targets. *Phys. Rev. A* **49**, 5, 3854–69 (1994).

[Walker93] T. Walker and L. W. Anderson. Consequences of Spin-Exchange Collisions for Polarized Hydrogen and Deuterium Targets. *Phys. Rev. Lett.* **71**(14), 2346 (1993).

[Walker97] Thad G. Walker and William Happer. Spin-Exchange Optical Pumping of Noble Gas Nuclei. *Reviews of Modern Physics* **69**, 2 629–642 (1997).

[Wieman91] C. E. Wieman and L. Hollberg. Using Diode Lasers for Atomic Physics. *Rev. Sci. Instrum.* **62**(1), 1–20 (1991).

[Whitehead75] J. C. Whitehead. Classical Trajectory Studies of Alkali Atom - Alkali Dimer Exchange Reactions, Li+Li_2. *Mol. Phys.* **29**(1), 177-89 (1975).

[Wolber98] J. Wolber, S. J. Doran, M. O. Leach and A. Bifone. Measuring Diffusion of Xenon in Solution with Hyperpolarized ^{129}Xe NMR. *Chem. Phys. Lett.* **296**(3-4), 391–96 (1998).

[Woodgate] G. K. Woodgate. *Elementary Atomic Structure.* Oxford University Press, New York (1980).

[Woste96] L. Woste. Laser Spectroscopy of Metal Clusters. *Zeitschrift für Physikalische Chemie* **196**, 11–41 (1996).

[Wu85] Z. Wu, T. G. Walker and W. Happer. Spin-Rotation Interaction of Noble-Gas Alkali-Metal Atom Pairs. *Phys. Rev. Lett.* **54**, 17, 1921–24 (1985).

[Wu86] Z. Wu, M. Kitano, W. Happer, M. Hou and J. Daniels. Optical Determination of Alkali Metal Vapor Number Density Using Faraday Rotation. *Appl. Opt.* **25**, 4483–91 (1986).

[Wu90] Z. Wu, W. Happer, M. Kitano and J. Daniels. Experimental Studies of Wall Interactions of Adsorbed Spin-Polarized ^{131}Xe Nuclei. *Physical Review A* **42**, 2774 (1990).